nature communications

Article

https://doi.org/10.1038/s41467-024-48871-4

Sub-100-fs energy transfer in coenzyme NADH is a coherent process assisted by a charge-transfer state

Received: 18 September 2023

Accepted: 15 May 2024

Published online: 08 June 2024

Check for updates

Vishal Kumar Jaiswal[1], Daniel Aranda Ruiz[2,6], Vasilis Petropoulos[3,6], Piotr Kabaciński[3,6], Francesco Montorsi[1], Lorenzo Uboldi[3], Simone Ugolini[1], Shaul Mukamel[4], Giulio Cerullo[3] ✉, Marco Garavelli[1] ✉, Fabrizio Santoro[5] & Artur Nenov[1] ✉

Excitation energy transfer (EET) is a key photoinduced process in biological chromophoric assemblies. Here we investigate the factors which can drive EET into efficient ultrafast sub-ps regimes. We demonstrate how a coherent transport of electronic population could facilitate this in water solvated NADH coenzyme and uncover the role of an intermediate dark charge-transfer state. High temporal resolution ultrafast optical spectroscopy gives a 54±11 fs time constant for the EET process. Nonadiabatic quantum dynamical simulations computed through the time-evolution of multidimensional wavepackets suggest that the population transfer is mediated by photoexcited molecular vibrations due to strong coupling between the electronic states. The polar aqueous solvent environment leads to the active participation of a dark charge transfer state, accelerating the vibronically coherent EET process in favorably stacked conformers and solvent cavities. Our work demonstrates how the interplay of structural and environmental factors leads to diverse pathways for the EET process in flexible heterodimers and provides general insights relevant for coherent EET processes in stacked multichromophoric aggregates like DNA strands.

Following the excitation energy transfer (EET) between chromophoric units in multimeric aggregates is of key importance for understanding biological processes like photosynthesis and DNA photodamage, as well as for the design of efficient light-harvesting molecular assemblies.[1–3] EET in these systems falls between the regimes of coherent and incoherent energy transport.[4] Where a process is placed in this sliding scale is dictated by: a) the energetic separation of relevant electronic states versus the coupling strength to each other and with the environment[5–9]; b) the spatial separation of the monomers in the macro-structure.

In homoaggregates, coherent population oscillations of quantum origin between the individual sites coupled to each other with a fixed phase relation in so-called excitonic excited states (ES) arise due to purely electronic coupling between the monomers. Coupling the electronic dynamics to a bath of nuclear degrees of freedom facilitates an efficient and ultrafast unidirectional population transfer to the

[1]Dipartimento di Chimica industriale "Toso Montanari", Università di Bologna, Viale del Risorgimento 4, 40136 Bologna, Italy. [2]ICMol, Universidad de Valencia, Catedrático José Beltrán Martínez, 2, 46980 Paterna, Spain. [3]Dipartimento di Fisica, Politecnico di Milano, Piazza Leonardo da Vinci 32, 20133 Milano, Italy. [4]Department of Chemistry and Department of Physics and Astronomy, University of California, Irvine, CA 92697, USA. [5]Istituto di Chimica dei Composti Organometallici (ICCOM-CNR), Area della Ricerca del CNR, Via Moruzzi 1, I-56124 Pisa, Italy. [6]These authors contributed equally: Daniel Aranda Ruiz, Vasilis Petropoulos, Piotr Kabaciński. ✉e-mail: giulio.cerullo@polimi.it; marco.garavelli@unibo.it; artur.nenov@unibo.it

lowest excitonic state. The role of such electronic coherences in disordered biological systems, such as the reaction centers of light-harvesting complexes, is being intensely debated[10–13].

In heterodimers with energetically well-separated electronic states, the motion of the nuclear wavepacket can strongly tune the energy gaps promoting crossings where electronic and vibronic couplings, i.e. wave function mixing along nuclear degrees of freedom, facilitate the population transfer[14–21]. In the limit of large donor-acceptor separation (i.e. >10 Å) inter-chromophore orbital overlaps are negligible, and couplings are dictated by the long-range electrostatic interactions. As the resulting electronic couplings are weaker than the coupling to the environment, the coherently prepared excited state first thermalizes through vibrational cooling on the picosecond time scale[22,23]. The EET then occurs incoherently on tens of ps-to-ns time scale, with rates that can be estimated by utilizing Förster resonance energy transfer theory. In the case of closely packed hetero-aggregates, on the other hand, variations of the inter-chromophore orbital overlaps and mixing with charge-transfer (CT) configurations[24,25] occurring during the photoinduced vibrational dynamics give rise to electronic and vibronic couplings which can be as pronounced as their intra-molecular counterparts, accelerating the EET down to the sub-ps regime. In this limit, the coherent motion of the nuclear wavepacket before thermalization (referred to as classical coherence) induces an inherently coherent EET competitive even with possible sub-ps decay channels such as intramolecular internal conversion (IC) to the ground state (GS) mediated by conical intersections (CIs).

NADH, the reduced form of nicotinamide adenine dinucleotide (NAD), is an important coenzyme found in the mitochondria that is part of the electron transport chain leading to the generation of adenosine triphosphate[26]. It is a dimer consisting of the two chromophores adenine (Ade) and nicotinamide (Nic), which absorb light in the ultraviolet (UV) region, connected through a phosphate bridge. This bichromophoric structure provides a playground rich with photoinduced processes, which are used as spectroscopic markers for cellular metabolism, for example, in label-free multimodal microscopy[27,28].

The high conformational flexibility afforded by the phosphate bridge linking the two monomers leads to DNA-like stacked (folded) or unstacked (unfolded) conformers whose ratio depends on solvent polarity, pH, and temperature[29–33]. While in alcoholic environments, like propylene glycol or methanol, there is a high propensity of unstacked conformations, a considerable percentage of stacked conformers is observed in water[34–37]. In its folded state, NADH is characterized by a photoinduced ultrafast EET process from Ade (donor) to Nic (acceptor). Since its first observation by Weber in 1957[34], the EET process, which involves the frontier π-orbitals of the locally excited (LE) states of the two monomers[38,39], has been extensively studied. Upon impulsive resonant excitation of the L_a-state of Ade, immediate (within the ≈100-fs temporal resolution of the ultrafast experiments) emission was observed from the lowest ππ* state of Nic (referred henceforth as Nic*). Previous time-resolved fluorescence and transient absorption (TA) experiments revealed the ultrafast nature of the process, placing the EET timescale in the sub-100-fs range[36,37], but with significant uncertainty due to their limited temporal resolution.

In this letter, using the example of NADH, we illuminate the structural, energetic and environmental conditions which favor a sub-100-fs coherent EET mechanism against IC in a closely stacked molecular heteroaggregate. Using UV TA spectroscopy with sub-30-fs temporal resolution, we resolve the EET from Ade to Nic* in water and find that, with a time constant $\tau_{EET} = 54 \pm 11$ fs, it is much faster than intra-Ade IC to the GS, which occurs with a time constant $\tau_{IC} \sim 160$ fs[40–46]. This observation places the mechanism through which the EET occurs completely outside the applicability of Förster theory still employed in the analysis of NADH photophysics[36,37]. Through multidimensional nonadiabatic quantum dynamics, we anticipate that this ultrafast EET in folded conformers is channeled through coherent vibrational motion along the same planar modes that facilitate intra-Ade IC. These coherent molecular vibrations contribute to the EET being faster than IC to the GS as, for the latter process, additional out-of-plane structural deformations are needed to bring the L_a and GS electronic potential energy surfaces to degeneracy. This is a general system-independent observation which implies that EET is a competitive deactivation process in closely stacked aggregates. Furthermore, our simulations reveal a dark Nic→Ade CT state, highly susceptible to structural and environmental disorder. In favorably stacked dimers and in cooperation with the fluctuations of the polar environment, the CT state is stabilized in the vicinity of the L_a state and acts as an intermediary that further boosts the EET yield.

Results

Transient absorption spectra of adenosine and NADH

Figure 1a, b depict the TA maps of Adenosine (a) and NADH (b) in water upon resonant excitation of the Ade moiety at 4.7 eV with sub-20-fs pulses and broadband (1.9-3.2 eV) probing. The excited state of the Ade monomer exhibits an intense photo-induced absorption (PA) band that spans our entire probe photon energy range, characterized by a sharp peak at >3 eV (Fig. 1a). This PA band decays on the <300-fs timescale as a result of Ade's L_a-state IC pathway back to the ground state. This is consistent with the vibronically driven 100–300 fs IC, reported for Ade and its derivatives[40–47].

The 4.7 eV UV pulse predominantly photoexcites the Ade moiety in NADH, resulting in an initial PA band similar to the one reported for the monomeric Ade (Fig. 2b). As mentioned earlier, the equilibrium between folded/unfolded conformers in NADH heavily depends on the solvent. In methanol, NADH exists almost entirely in its open form and thus the EET pathway is negligible, resulting in excited state dynamics similar to isolated Ade in water (see Suppl. Fig. 1 and Suppl. Fig. 2 in the Supplementary Information (SI)). However, in water, NADH has an approximate 30/70 population ratio between folded and unfolded configurations[37]. The significant population of folded structures activates the EET from Ade to Nic, resulting in an additional ultrafast deactivation channel of Ade's excited state (Fig. 1b). At 3.1 eV probe photon energy, the EET process results in a long-lived signal, due to a PA band from the Nic* state (Fig. 1c). In contrast, for a 2.5 eV probe, only Ade displays a significant PA. Comparison of the dynamics of Adenosine and NADH in water at this probe photon energy (Fig. 1d) reveals a faster decay for NADH, due to the additional deactivation channel for the $L_a$excited state of Ade through EET to Nic*.

Estimation of experimental EET timescale

Global fitting of the TA data, as shown in Table 1, gives time constants of $\boldsymbol{\tau}_{\mathbf{1Ade}} = 157 \pm 4$ fs and $\boldsymbol{\tau}_{\mathbf{1NADH,\ water}} = 122 \pm 4$ fs for Ade and NADH in water, respectively. While in isolated Ade and NADH solvated in methanol, the corresponding time constants of 157 fs and 167 fs correspond to the IC back to the GS, in NADH solvated in water the EET mechanism opens up an additional channel of excited state deactivation, increasing its rate. Taking into account the 30/70 equilibrium between folded and unfolded forms, the faster lifetime $\boldsymbol{\tau}_{\mathbf{1NADH,\ water}} = 122$ fs extracted by global analysis can be considered as a weighted average of the folded and unfolded ultrafast lifetime components:

$$\boldsymbol{\tau}_{\mathbf{1NADH,\ water}} = 0.7\,\boldsymbol{\tau}_{\mathbf{1NADH,\ unfolded}} + 0.3\,\boldsymbol{\tau}_{\mathbf{1NADH,\ folded}}$$

Assuming similar excited-state deactivations in unfolded water-solvated NADH and isolated Ade, one can take $\boldsymbol{\tau}_{\mathbf{NADH,\ unfolded}} = \boldsymbol{\tau}_{\mathbf{1Ade,\ water}} = 157$ fs, which results in a time constant $\boldsymbol{\tau}_{\mathbf{NADH,\ folded}} = 40 \pm 6$ fs for the folded NADH conformers. This total decay rate obtained for the folded NADH components ($\mathbf{k}_{\mathbf{total}} = (40\ \mathrm{fs})^{-1}$) reflects

https://doi.org/10.1038/s41467-024-48871-4

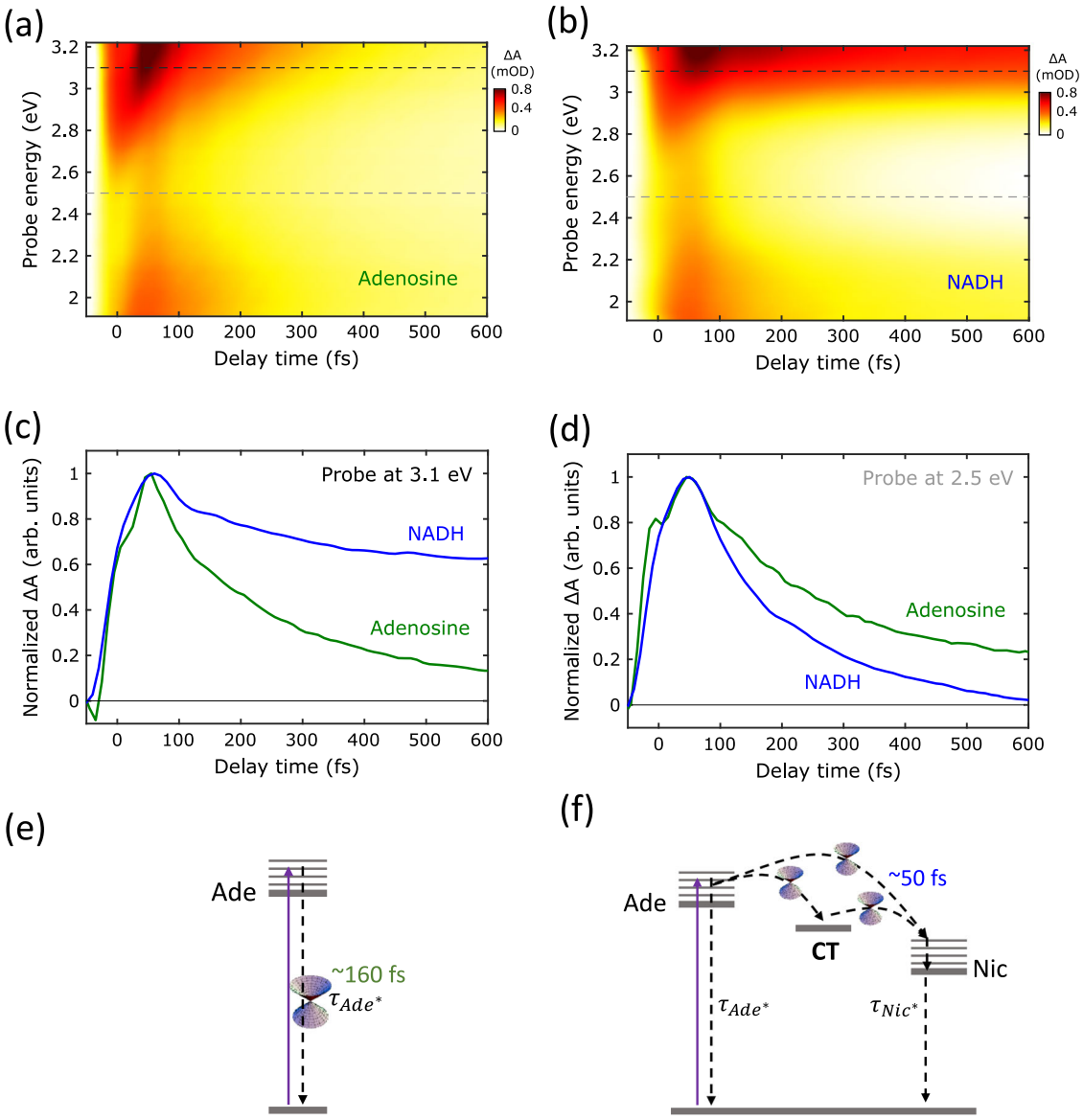

Fig. 1 | Ultrafast energy transfer in NADH. Transient absorption (TA) maps of **a** Adenosine (Ade) and **b** NADH in piperazine-N,N′-bis(2-ethanesulfonic acid) (PIPES) aqueous buffer upon photoexcitation with sub-20-fs pulses at 4.7 eV. The dashed lines indicate the selected time-traces shown in Fig. 1c, d for detection at 3.1 eV (black dashed line) and 2.5 eV (gray dashed line). **c**, **d** Time-traces of Ade (green) and NADH (blue) for probing at **c** 3.1 eV and **d** 2.5 eV respectively. The faint gray line in Fig. 1c, d defines the zero line (ΔA = 0). Schematics depicting the ultrafast vibronic processes after Ade resonant excitation which lead to **e** internal conversion (IC) in Ade and **f** direct/through-CT coherent EET in NADH. Source data are provided as a Source Data file.

the sum of the rates for Ade IC ($\mathbf{k}_{IC} = (157\ \mathrm{fs})^{-1}$) and ultrafast EET from the Ade L_a-state to Nic* ($\mathbf{k}_{ET}$), resulting in $\mathbf{k}_{total} = \mathbf{k}_{IC} + \mathbf{k}_{ET}$, thus giving a time constant of $\boldsymbol{\tau}_{ET,\ folded} = 54 \pm 11$ fs for the EET process (see a detailed discussion in Suppl. Note 1.2 and 1.3).

Quantum dynamics simulations of the EET in NADH

To gain insight into the ~50-fs Ade →Nic EET mechanism in the folded NADH forms, we have modeled the photoinduced time-evolution of the system by nonadiabatic quantum dynamics of multidimensional wavepackets using the MCTDH method[48–52]. Due to the large number of normal modes in the bichromophoric molecule, the multilayer formulation of the MCTDH method (ML-MCTDH) was employed[53–56]. The coupled dynamics of the electronic states of the system through the vibrational degrees of freedom are described by a Linear Vibronic Coupling (LVC) Hamiltonian[57,58], parametrized with the energies and gradients computed at the multiconfigurational wavefunction-based XMS-CASPT2 level of theory[59]. Calculations were performed on different water solvated stacked NADH aggregates, obtained from a 20 ns of Replica Exchange Molecular Dynamics (REMD)[60], in a quantum mechanics/molecular mechanics (QM/MM)[61] setup allowing to account for the conformational diversity and solvent effects with quantitative accuracy. Details are provided in the Suppl. Note 2 to 7.

The structural flexibility of NADH leads to diverse relative orientations of the two bases in the stacked conformers, whose relative populations in REMD dynamics are detailed in Suppl. Table 2. Figure 2d–f shows the time-evolution of electronic states population in representative structures of the three most populated stacked conformers, capturing 65% of stacked population. The dynamics reveal that EET is an ultrafast process mediated by coherent vibrational motions. The coupling between the electronic states induced by nuclear motions along these vibrations facilitates a near complete Ade →Nic population transfer on a sub-100-fs time scale. As shown in Fig. 2 and additional dynamics reported in Suppl. Note. 8 of the SI, the EET mechanism can be either direct (Fig. 2f) or proceed involving a

https://doi.org/10.1038/s41467-024-48871-4

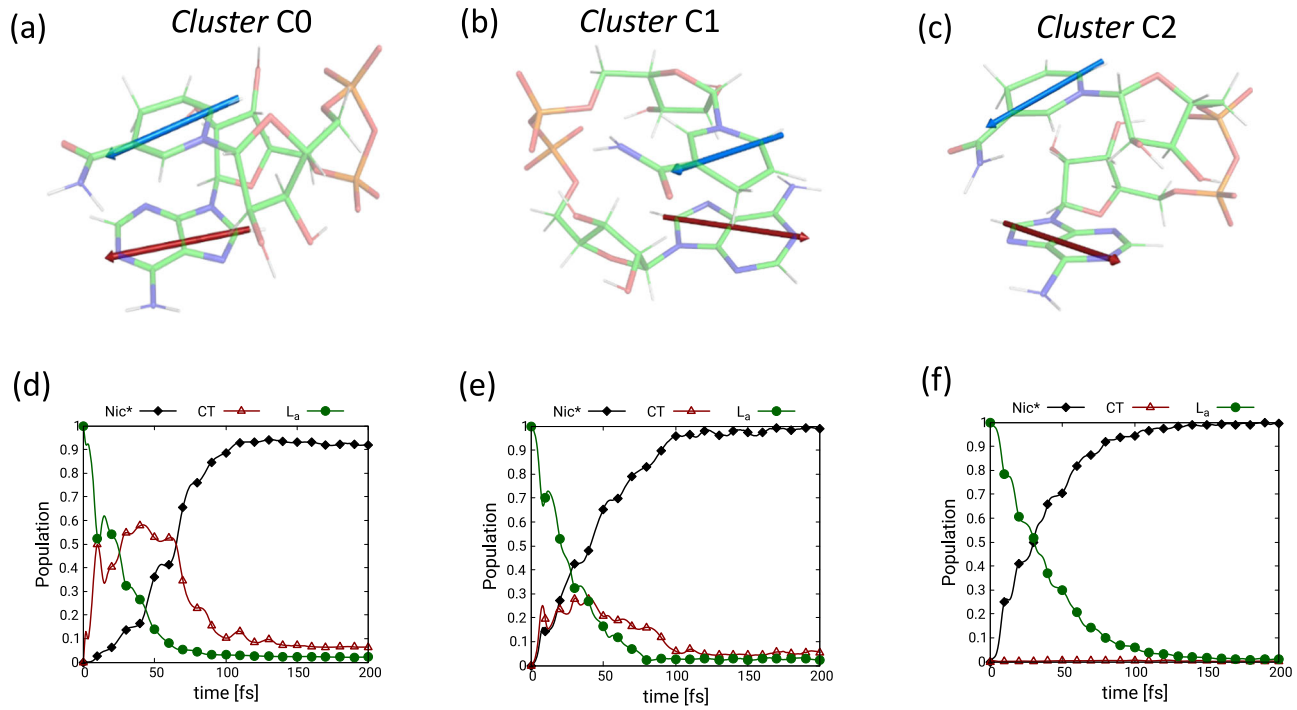

Fig. 2 | Ultrafast energy transfer dynamics in highest populated clusters. **a**–**c** Conformational representatives of the three largest clusters of Replica-Exchange Molecular Dynamics. The relative orientation of two chromophores in different clusters is shown through arrows colored blue (on Nic) and red (on Ade). Carbon atoms are colored in green, nitrogens in blue, hydrogens in white, oxygen in red and phosphorus in yellow. Details about clustering and the population of clusters are given in Suppl. Note. 2. **d**–**f** Quantum Dynamics (using ML-MCTDH) on a representative structure of the three largest clusters. Additional dynamics on other representative structures are shown in Suppl. Fig. 10. Source data are provided as a Source Data file.

Table 1 | Time constants, accompanied by their experimental uncertainty, as obtained from the global fitting of the TA data in the case of Adenosine in water and NADH in water

	τ_1 (fs)	τ_2 (fs)	τ_3 (fs)
Adenosine in water	157 ± 4	894 ± 50	-
NADH in water	122 ± 4	878 ± 40	long

Nic→Ade CT state as an intermediary (Fig. 2d,e). The propensity for a direct or CT-mediated EET mechanism is dictated by the energetic position of the CT state versus the La. We shall show later how this is affected by the structural and solvent heterogeneity present in the system.

Vibronically coherent mechanisms are ubiquitous in ultrafast photophysical processes involving population transfer between electronic states[62,63]. Impulsively excited molecular vibrations, called tuning modes, modulate the energy gaps between electronic states, whereas vibrations known as coupling modes, together with purely electronic coupling, induce wave function mixing which dictates the rate of the non-adiabatic population transfer between electronic states. The direct transfer in NADH is mediated by high-frequency stretching modes of the initially excited Ade moiety. In particular, the C-C and C-N stretchings, with frequencies of ~1400 cm^{-1} and ~1600 cm^{-1}, respectively, show the highest tuning and, simultaneously, significant coupling between L_a and Nic*, irrespective of stacking conformation (Suppl. Fig. 15 in the SI). The oscillatory pattern in the first 100 fs of the population dynamics (Fig. 2f) with a period of ≈10 fs is the result of the tuning modes leading to energy degeneracy (real La/Nic* CI) between L_a and Nic* every half a period (Suppl. Fig. 12 and Suppl. Fig. 16 in SI).

To gain further insight, we computed the quantum electronic coherences between L_a and Nic* along the dynamics (Suppl. Note. 15) and observed that they last for at least 70 fs while exhibiting recurrences with a period comparable to the frequencies of the stretching modes (Suppl. Fig. 18). Their eventual decay is caused by the concurrent effects of: a) progessive population depletion in the $L_a$state accompanied by the accumulation in the Nic* state; b) progessive decrease of the overlap of the wavepackets evolving in the L_a and Nic* states. The direct EET is facilitated to equal amounts by electronic (E_{ij}^0) and vibronic (λ_{ij}) couplings, which can be verified by switching off their respective contribution (Suppl. Fig. 18). The population transfer becomes slower in both cases, yet, notably, population inversion still occurs within 100 fs. Interestingly, the observation of ultrafast EET in the absence of electronic couplings makes apparent that in closely stacked aggregates even small localized deformations such as stretchings induce vibronic couplings large enough to facilitate a sub-100-fs EET.

We note that intra-monomer IC in Ade is initially driven by the same impusively excited high-frequency modes. However, as the energy gap (with the GS) to overcome is significantly bigger (ca. 5 eV with respect to ca. 1.5 eV), additional deformations, such as ring puckering, are necessary to facilitate IC to the GS[42,46,64,65]. Since these deformations need activation and are associated with more pronounced displacements, IC is naturally slower, taking a few hundreds of fs. Source data are provided as a Source Data file.

Factors affecting the participation of CT state in EET process

The extent of participation of the dark CT state in the EET process is determined by its energetic position and coupling to the two monomer LE states L_a and Nic*. The structural and solvent dynamics impart a large amount of heterogeneity to the system, leading to various types of stacked conformers with different relative orientations of the two bases (Fig. 2a–c). While the energetic positions of the L_a and Nic* are relatively unaffected by the different arrangements of the two chromophores, the CT state is markedly more sensitive. Figure 3 shows how

https://doi.org/10.1038/s41467-024-48871-4

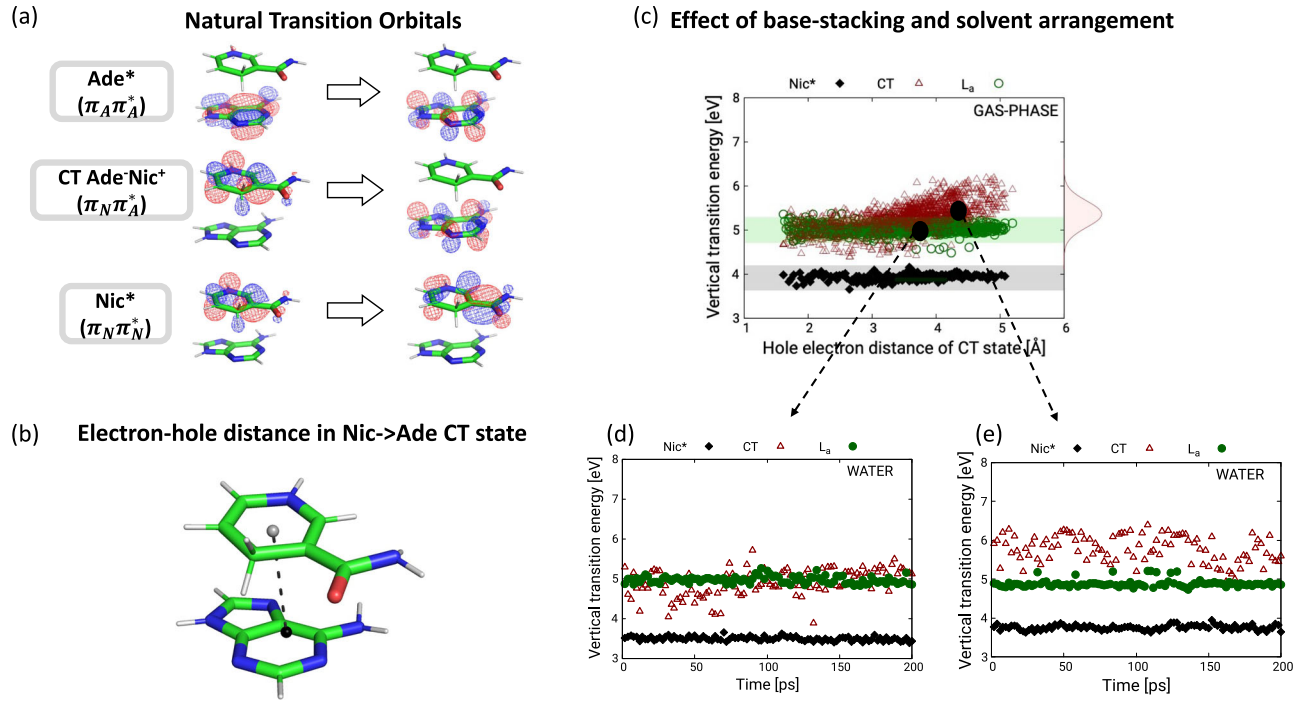

Fig. 3 | Stacking and solvent effects on energies of charge-transfer (CT) and locally excited (LE) states. a The natural transition orbitals of the two LE and lowest CT state involved in the EET process. **b** The electron-hole distance[77,78] in the Nic→Ade CT state in a representative stacked conformer depicted with a dashed line. The two dots specify the position of the center of charges of hole and electron created in the CT state. **c** Stacking Effect: Vertical transition energies of the CT state vs the electron-hole distance of the CT state in gas-phase. The black and green bands indicate the energies of Nic* and L_a state which show minimal fluctuation compared to CT state. The Gaussian profile shows the spread of the values of the CT state with FWHM of ca. 1 eV. Two structures with markedly different CT energies are highlighted with black dots for studying solvent effects. **d**, **e** Solvent Effect: The effect of the solvent fluctuations on the energies of the diabatic states for the two structures highlighted in (**c**), which represent respectively a case in which the CT is near degenerate with the L_a-state of Ade (**d**) and a case in which the CT state is significantly higher in energy (**e**). The two profiles were obtained by running an equilibrated solvent MD around the two frozen NADH solute geometry and computing vertical transition energies at XMS-CASPT2 level. Details in Suppl. Note. 14.

both the stacking and solvent configuration individually affect the energetic position of the CT state. The transfer of an electron from Nic to Ade in the CT state creates an electron-hole dipole in the system (Fig. 3b). The relative orientation of the two bases modulates the distance between the centers of (positive and negative) charge of this electron-hole pair in stacked conformations from 3 to 5 Å. In return, this causes a variation of the CT state energy by ~1 eV in vacuo (Fig. 3c) at the time of photoexcitation. Introducing the solvent, the interaction of the CT dipole with the electric field of water additionally modulates the fluctuation of CT state energy by ~1 eV, as seen from computations in solvent ensemble around two geometries selected from the manifold of stacked conformations (Fig. 3d, e).

The combined effects of stacking and solvent orientation dictate whether the CT state can actively participate in ultrafast EET process. If a certain stacking places the CT state more than 0.5 eV above the L_a state in gas-phase, its energy fluctuations due to the interaction with the solvent cannot render the CT accessible from the L_a state after photoexcitation (Fig. 3e). In such conformations, populating predominantly cluster C2 – with a median interbase distance of ~4.6 Å – the EET occurs via a direct transfer. Instead, for stacking where the CT state is energetically closer to the L_a (i.e. within less than 0.5 eV) in gas-phase, the solvent fluctuations can induce stabilization of the CT band around and even below the L_a state (Fig. 3d), eventually enabling its active participation in the EET dynamics. Such is the case for the most populated stacked cluster C0 – with a median interbase distance of ~4.12 Å. The average ratio between La/CT electronic coupling and energy gap $|V/\Delta|$ = 0.268 calculated for the conformations in this cluster indicates a strong wave function mixing and, consequently, admixing of CT character in the bright adiabatic state in the Franck-Condon (FC) region.

Figure 2d shows a representative dynamics for a snapshot of cluster C0 in which the CT state is 0.5 eV below the L_a in the FC region. A virtually immediate increase of the population of the CT state to 50% on a 10 fs timescale is observed, which is accompanied by the instantaneous formation of a quantum coherence which lasts for about 70 fs (column LVC in Suppl. Fig. 19). Tuning along the high-frequency C-C and C-N stretching modes quickly overcomes the La/CT energy gap, so that electronic and vibronic couplings – exhibiting larger magnitudes compared to their counterparts in the direct EET due to the one-electron nature of the process – efficiently promote La→CT population transfer. Notably, if tuning modes are switched off, thus forcing purely electronic dynamics between stationary wavepackets, no population transfer takes place despite the formation of coherences of sizeable magnitude (column "no λ_{ii} All" in Suppl. Fig. 19). This makes evident that tuning modes are essential to circumvent the La/CT energy gap for the electronic and vibronic couplings to have effect. Furthermore, we selectively switched off either coupling to investigate its impact on the Nic→Ade electron transfer event (columns "no E_{ij}^0 All" and "no λ_{ij} All" in Suppl. Fig. 19). Purely electronic couplings are found to promote La/CT population inversion on a 10-fs timescale. Electronic coherence formation is vibrationally assisted as can be noted by the coherence recurrences with times compatible with the periods of the high-frequency tuning modes, and by the fact that the coherence magnitude moderately increases when switching off electronic couplings.

The population of the CT state is only transient and is transferred to Nic* creating, at the same time, an electronic coherence between CT and Nic* that lasts till 150 fs. Contrary to the high frequency modes driving the direct EET, we find that multiple conformation-dependent low frequency modes delocalized over both moieties facilitate this second step of the CT-mediated EET. These low-frequency modes

https://doi.org/10.1038/s41467-024-48871-4

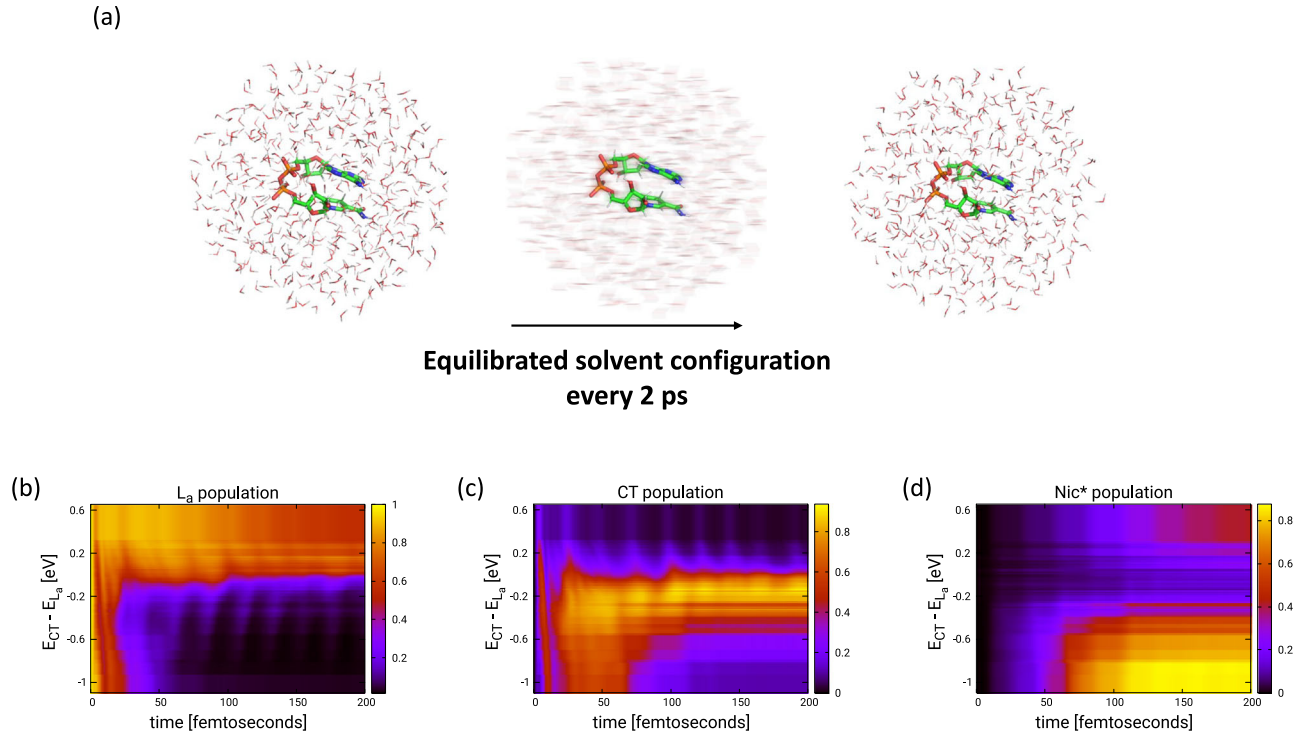

Fig. 4 | Wavepacket dynamics on most populated conformer in 100 equilibrated solvent ensembles. a An ensemble of equilibrated solvent configurations is created around a representative structure of most populated cluster of the REMD. The solute NADH is kept frozen during the solvent equilibrium dynamics. **b**–**d** Populations dynamics in the three diabatic electronic states - L_a (left), CT (middle), Nic* (right) – during the first 200 fs after photoexcitation of the L_a state as a function of the relative energy difference between the CT and $L_a$states (i.e. E_{CT}-E_{La}). The plots are generated from individual ML-MCTDH dynamics performed on 100 snapshots from the solvent equilibrium dynamics as indicated in (**a**), each one with characteristic solvent-modulated electronic energies, electronic and vibronic couplings. Details on the simulation can be found in Suppl. Note. 14. Source data are provided as a Source Data file.

show the largest vibronic coupling between the CT and Nic* state amongst the normal modes of the system. When the vibronic couplings along these modes are switched off (see Suppl. Fig. 14 in SI for a representative case), the transfer to Nic* from the CT state is significantly slowed down and the population remains trapped in the CT state.

To explore the role of solvent heterogeneity in the ultrafast EET process, we carried out independent wavepacket dynamics on a representative structure from the most populated conformer embedded in 100 different solvent configurations obtained through equilibrated molecular dynamics at room temperature (Fig. 4a). Thereby, for each solvent arrangement the LVC Hamiltonian was reparametrized to take into account the solvent effect on the energetics and electronic coupling (details in Suppl. Note. 14.1). Figure 4b shows a false color plot of the state-specific population evolution upon instantaneous L_a photoexcitation along the 100 wavepacket dynamics ordered according to the energy gap between CT and L_a in the FC point. An ultrafast population transfer to Nic* is observed when the CT state is energetically below the L_a state at the FC geometry. The CT state acts as a doorway populated within 10-20 fs after excitation of the L_a state and depopulated within 60 fs by transferring the population to the Nic* state. The acceleration provided by the CT state becomes apparent when comparing against dynamics performed in the same solvent ensemble after switching off LE-CT couplings (Suppl. Fig. 17 in SI, also see Suppl. Figs. 10/S11) where the EET process gets substantially slowed down. A similar retardation is observed for those solvent/stacking configurations where the CT state is substantially above the L_a (Fig. 4b) and, therefore, cannot act as a doorway in the EET mechanism. Thus, the acceleration provided by the CT state can play a paramount role in making the EET mechanism the dominant relaxation path immediately following photoexcitation.

Besides the ultrafast population transfer to Nic*, we observe population trapping in the CT state in our dynamics reported in Fig. 4 when L_a and CT are energetically close in the FC region. In this case, after an ultrafast population of the CT state, a subsequent transfer to Nic* state is substantially slowed down as the CT and Nic* surfaces do not cross in the course of the vibrational dynamics in the CT state. However, it should be noted that our model lacks the dynamic relaxation of the electronic states induced by the temporal response of the polar solvent. Indeed, a charge-separated state can access lower energies upon relaxation of the molecules of the surrounding polar solvent which can occur on a timescale as fast as sub-50-fs in water[66–68]. Thus, we expect that the CT state stabilization induced by modeling the response of the polar solvent will further put these dynamics into the realm of ultrafast population transfer to Nic* state.

Discussion

In this work, we unambiguously demonstrate, by means of TA spectroscopy with sub-30-fs temporal resolution, that the ultrafast Ade to Nic EET in water-solvated NADH occurs on a 50-fs timescale. By means of multimode wavepacket quantum dynamics, we reveal that this is an electronically and vibrationally coherent process. Coherent molecular vibrations – high-frequency stretchings – activated upon optical excitation of Ade (the donor) tune the energy gap where electronic and vibronic couplings directly channel the electronic population to Nic (the acceptor). Depending on the spatial separation and relative orientation of the two monomers (which affects the magnitude of the couplings) the direct pathway exhibits timescales ranging from few tens of fs to several ps. Sub-100 fs direct EET pathways are only possible for very close (< 5 Å) stacking, since this activates inter-chromophore vibronic couplings of the same order of magnitude as intra-chromophore ones.

The EET process can be further accelerated via the mediation of a low-lying CT state coupled to the locally excited states of the two monomers. The relative orientation of the two monomers in closely stacked conformations, along with the solvent thermal fluctuations, affect the energetics of CT state and determine the propensity of the CT-mediated EET pathway. When the CT state is near-degenerate or below the $L_a$state of Ade, the first step of the CT-mediated EET, i.e. the Ade →Nic hole transfer, occurs quasi instantaneously. Completion of the EET process is observed within 100 fs, through the subsequent Ade→Nic electron transfer, which is dependent on the relaxation timescale of the solvent.

Our findings are of general validity for describing the dependence of energy transfer and charge separation processes on the coupling between electronic and nuclear degrees of freedom, conformational heterogeneity and solvent fluctuations in closely packed hetero-aggregates. The EET depends on the interplay of many factors: nature of the tuning and coupling modes and respectively the amplitude of their motion or the strength of coupling they carry; conformational freedom and spatial distance between chromophores in the aggregate; solvent polarity and thermalizaiton timescale. We identify the parameter window which facilitates ultrafast EET. At an inter-chromophore distance of <5 Å: a) electronic and vibronic couplings are equally relevant and cooperate in promoting efficient EET; b) even localized vibrational modes are capable of generating sufficiently strong orbital mixing and, thus, strong vibronic couplings; c) the short distance between the centers of negative and positive charge of the two chromophores stabilizes the CT state opening an additional EET pathway, favored in polar solvents. Most importantly, despite the conformational heterogeneity of such macro-structures, the EET is an intrinsically coherent process, i.e. governed by coherently oscillating wavepackets on the potential energy surfaces of the involved electronic states which tune the energy gaps and drive the EET unidirectionally from the donor to the acceptor. Such coherent EET cannot be described by Förster theory, which is suited to describe incoherent EET mechanisms.

Classical coherences manifest themselves through quantum beating in the TA spectra[69–71], yet, the high frequencies of the dominant modes in NADH prevent them from being registered with current state-of-the-art experimental setups. This makes the theoretical analysis much more relevant. We hope that our findings will be a stimulus to increase the temporal resolution of UV TA spectroscopy and to apply transient spectroscopies which interrogate other spectral ranges in which the CT state may show unambiguous fingerprints. In particular, we propose photoelectron spectroscopy as a more sensitive way to single out CT states, as ionization from the intermediately created negatively charged Ade would give rise to characteristic signatures at lower ionization energies compared to the neutral form. Eventually, this study discloses a learning path on how to underdstand, and thereafter tune, the control knobs that are crucial for the design of systems with tailored EET efficiency.

Methods

Experimental setup

Ultrafast TA experiments[72] were performed using a Ti:sapphire laser generating 100 fs pulses at 800 nm wavelength and 1 kHz repetition rate. Deep UV pump pulses tunable in the 4.2-4.8 eV range were generated as the second harmonic of a visible non-collinear optical parametric amplifier and compressed to sub-20-fs duration with a prism pair. Probe pulses covering 1.9-3.2 eV were obtained through white-light continuum generation by focusing a fraction of the fundamental beam in a calcium fluoride plate. Pump and probe polarizations were set at the magic angle (54.7°).

Sample preparation

β-NADH, in the form of reduced disodium salt hydrate, and adenosine were purchased from Sigma-Aldrich and used as received, dissolved in either methanol or 0.1 M piperazine-N,N′-bis(2-ethanesulfonic acid) (PIPES) aqueous buffer at pH 7.0. The samples were flown in a 150-µm-thick laminar liquid jet configuration, resulting in the absorbance of 2 OD at 4.7 eV pump photon energy. The used pump fluence was below 300 µJ/cm^2 to minimize the coherent artifact and solvated electron signals.

Estimation of experimental EET timescale

The timescale of the EET process was estimated by employing a sequential kinetic model, taking into account the diverse relaxation pathways undertaken in stacked and unstacked conformers. The timescale of the EET pathway was estimated from the obtained lifetimes of the various evolution-associated spectra (EAS) obtained through global analysis of the TA map. The full details are reported in Suppl. Note. 1.3.

Computational methods

The conformational heterogeneity of solvated NADH was sampled through replica-exchange molecular dynamics performed through AMBER molecular dynamics package as detailed in Suppl. Note. 2. The major conformers were identified through a cluster analysis using of internal distance matrix of the solute atoms. The population fraction and inter-base distances of major clusters are reported in Suppl Table 2. Hybrid QM/MM calculations were carried out with the COBRAMM[73,74] program, interfacing Gaussian16[75] and openMOLCAS[76] QM codes with the AMBER molecular dynamics package. The QM and MM partitioning involves three layers: High, Medium, and Low. The two chromophore bases in NADH solute are treated at QM level (High level), while the rest of the backbone along with the solvent is treated at MM level (details in Suppl. Note. 4). All geometry optimizations were done while allowing the backbone and the hydrogen-bonded solvent molecules to relax to the QM solute (Medium level), while the rest of the MM water molecules are frozen (Low Layer). The ground state geometry minimum was obtained at the Møller−Plesset second order perturbation theory (MP2) level. All computations utilized the Pople 6-31 G* basis set employing the Cholesky decomposition method to speed up the computation of atomic integrals. The vertical energies and gradients for the LVC model were obtained at XMS-CASPT2 level utilizing an active space of 4 electrons in 4 orbitals, comprising the frontier HOMO and LUMO of the two bases. The validity of the minimal active space was established by benchmarking against larger active space computations discussed in Suppl. Note. 5. Structure analysis (NTOs, attachment and detachment densities, electron-hole distance) was performed with the WFA module of Molcas[77,78]. All CASPT2 computations were done with zero IPEA shift, and an imaginary shift of 0.2.

Transformation of the adiabatic XMS-CASPT2 states to locally-excited and pure-CT states was done by the Fragment Excitation Difference procedure outlined by Hsu et al.[79]. In this method an excitation matrix Δx_{mn} is built which characterizes the excitation difference between the donor and acceptor. In our case, the diagonalization of this matrix separates out the locally excited states with eigenvalues +/−1 and the CT-state with an eigenvalue of 0. The transformation matrix thus obtained can be used to transform the Hamiltonian to the diabatic basis, to compute the static electronic coupling and the vibronically induced coupling between the diabatic states. Further details outlining the procedure are reported in Suppl. Note. 7.

ML-MCTDH dynamics were performed using a variant of the multilayer algorithm of Heidelberg MCTDH package[80] as implemented in Quantics[81] program. The system was parametrized with a Linear Vibronic Coupling model using energies, gradients and couplings computed at XMS-CASPT2 level. The wavepacket propagations were done with ML-MCTDH adopting a variable mean field scheme with a Runge-Kutta integrator up to a final time of 200 fs. The dynamics on different cluster representatives were performed with 62 photoactive vibrational modes selected from the total 84 normal modes of the

bichromophoric system included in the QM part of QM/MM setup. To select the photoactive modes, the maximum from the absolute value of either the gradients of the electronic states or interstate couplings of every pair of electronic states at Franck-Condon for each mode was chosen. All the 84 modes were sorted in decreasing order based on this value and the first 62 modes were selected. In this way, the discarded modes are the least active upon excitation as they have smallest gradients/interstate couplings at Franck-Condon (less than ~ 0.02 eV) and don't promote population transfer. The selected 62 modes were partitioned into system (16) and bath modes (46). For the primitive basis-set we adopted Hermite DVR functions. The 16 coordinates containing the largest coupling/gradients were grouped together by pairs of coordinates with similar frequency in the ML tree and described by a larger number of primitive (30) and single-particle functions, while the remainder 46 (the "bath") were grouped in pairs and described with less primitives (15) and single-particle functions. The 100 dynamics in different solvent ensembles were performed with 62 normal modes partitioned into a main system (8 modes) and bath (54 modes). The system modes were described 30 primitive bases and bath modes 15 primitive basis functions.

Data availability

The QM/MM optimized structures for the clusters representatives employed in this work, the solvent configurations for the dynamics displayed in Fig. 2 and the parameters used for the Hamiltonian employed in the MLMCTDH wavepacket dynamics have been deposited in the Zenodo database under the accession code 10987710. Source data for Figs. 1–4 are provided in the Source Data file[82] (https://doi.org/10.6084/m9.figshare.25640532). Source data are provided with this paper.

References

1. Ashkenazi, G., Kosloff, R. & Ratner, M. A. Photoexcited electron transfer: short-time dynamics and turnover control by dephasing, relaxation, and mixing. *J. Am. Chem. Soc.* **121**, 3386–3395 (1999).
2. Xu, D. & Schulten, K. Coupling of protein motion to electron transfer in a photosynthetic reaction center: investigating the low temperature behavior in the framework of the spin—boson model. *Chem. Phys.* **182**, 91–117 (1994).
3. Ando, K. & Sumi, H. Nonequilibrium oscillatory electron transfer in bacterial photosynthesis. *J. Phys. Chem. B* **102**, 10991–11000 (1998).
4. Olaya-Castro, A. & Scholes, G. D. Energy transfer from Förster–Dexter theory to quantum coherent light-harvesting. *Int. Rev. Phys. Chem.* **30**, 49–77 (2011).
5. Simpson, W. T. & Peterson, D. L. Coupling strength for resonance force transfer of electronic energy in van der waals solids. *J. Chem. Phys.* **26**, 588–593 (1957).
6. Robinson, G. W. & Frosch, R. P. Electronic excitation transfer and relaxation. *J. Chem. Phys.* **38**, 1187–1203 (1963).
7. Scholes, G. D. & Ghiggino, K. P. Rate expressions for excitation transfer I. Radiationless transition theory perspective. *J. Chem. Phys.* **101**, 1251–1261 (1994).
8. Clegg, R. M., Sener, M. & Govindjee. From Förster resonance energy transfer to coherent resonance energy transfer and back. *Proc. SPIE 7561, Optical Biopsy VII*, 75610C (2010).
9. Mendive-Tapia, D. et al. Multidimensional quantum mechanical modeling of electron transfer and electronic coherence in plant cryptochromes: the role of initial bath conditions. *J. Phys. Chem. B* **122**, 126–136 (2018).
10. Engel, G. S. et al. Evidence for wavelike energy transfer through quantum coherence in photosynthetic systems. *Nature* **446**, 782–786 (2007).
11. Collini, E. et al. Coherently wired light-harvesting in photosynthetic marine algae at ambient temperature. *Nature* **463**, 644–647 (2010).
12. Panitchayangkoon, G. et al. Long-lived quantum coherence in photosynthetic complexes at physiological temperature. *Proc. Natl Acad. Sci. USA* **107**, 12766–12770 (2010).
13. Duan, H.-G. et al. Nature does not rely on long-lived electronic quantum coherence for photosynthetic energy transfer. *Proc. Natl Acad. Sci.* **114**, 8493–8498 (2017).
14. Arsenault, E. A., Yoneda, Y., Iwai, M., Niyogi, K. K. & Fleming, G. R. The role of mixed vibronic Qy-Qx states in green light absorption of light-harvesting complex II. *Nat. Commun.* **11**, 6011 (2020).
15. Halpin, A. et al. Two-dimensional spectroscopy of a molecular dimer unveils the effects of vibronic coupling on exciton coherences. *Nat. Chem.* **6**, 196–201 (2014).
16. Sil, S. et al. Excitation energy transfer and vibronic coherence in intact phycobilisomes. *Nat. Chem.* **14**, 1286–1294 (2022).
17. Fuller, F. D. et al. Vibronic coherence in oxygenic photosynthesis. *Nat. Chem.* **6**, 706–711 (2014).
18. Lin, C., Kim, T., Schultz, J. D., Young, R. M. & Wasielewski, M. R. Accelerating symmetry-breaking charge separation in a perylenediimide trimer through a vibronically coherent dimer intermediate. *Nat. Chem.* **14**, 786–793 (2022).
19. Romero, E. et al. Quantum coherence in photosynthesis for efficient solar-energy conversion. *Nat. Phys.* **10**, 676–682 (2014).
20. Perlík, V. et al. Vibronic coupling explains the ultrafast carotenoid-to-bacteriochlorophyll energy transfer in natural and artificial light harvesters. *J. Chem. Phys.* **142**, 212434 (2015).
21. Jumper, C. C., van Stokkum, I. H. M., Mirkovic, T. & Scholes, G. D. Vibronic wavepackets and energy transfer in cryptophyte light-harvesting complexes. *J. Phys. Chem. B* **122**, 6328–6340 (2018).
22. Forster Th. energiewanderung und fluoreszenz. *Naturwissenschaften* **33**, 166–175 (1946).
23. Theodor Förster. Energy migration and fluorescence. *J. Biomed. Opt.* **17**, 011002 (2012).
24. Harcourt, R. D., Scholes, G. D. & Ghiggino, K. P. Rate expressions for excitation transfer. II. Electronic considerations of direct and through–configuration exciton resonance interactions. *J. Chem. Phys.* **101**, 10521–10525 (1994).
25. Feng, X., Luzanov, A. V. & Krylov, A. I. Fission of entangled spins: an electronic structure perspective. *J. Phys. Chem. Lett.* **4**, 3845–3852 (2013).
26. Ghukasyan, V. V. & Heikal, A. A. (Eds.) *Natural Biomarkers for Cellular Metabolism: Biology, Techniques, and Applications*. (1st ed.). (CRC Press, London, 2014).
27. Ranjit, S., Lanzanò, L., Libby, A. E., Gratton, E. & Levi, M. Advances in fluorescence microscopy techniques to study kidney function. *Nat. Rev. Nephrol.* **17**, 128–144 (2021).
28. Lakowicz, J. R., Szmacinski, H., Nowaczyk, K. & Johnson, M. L. Fluorescence lifetime imaging of free and protein-bound NADH. *Proc. Natl Acad. Sci.* **89**, 1271–1275 (1992).
29. Tropp, J. & Redfield, A. G. Proton magnetic resonance of NADH in water-methanol mixtures. Conformational change and behavior of exchangeable proton resonances as a function of temperature. *J. Am. Chem. Soc.* **102**, 534–538 (1980).
30. Hull, R. V., Conger, P. S. & Hoobler, R. J. Conformation of NADH studied by fluorescence excitation transfer spectroscopy. *Biophys. Chem.* **90**, 9–16 (2001).
31. Li, H. et al. Ultrafast fluorescence dynamics of NADH in aprotic solvents: Quasi-static self-quenching unmasked. *J. Photochem. Photobiol. Chem.* **436**, 114384 (2023).
32. Cao, S. et al. Femtosecond fluorescence spectra of NADH in solution: ultrafast solvation dynamics. *J. Phys. Chem. B* **124**, 771–776 (2020).
33. Reza, M. M. et al. Primary photophysics of nicotinamide chromophores in their oxidized and reduced forms. *J. Phys. Chem. B* **127**, 8432–8445 (2023).

34. Weber, G. Intramolecular transfer of electronic energy in dihydro diphosphopyridine nucleotide. *Nature* **180**, 1409–1409 (1957).
35. Freed, S., Neyfakh, E. A. & Tumerman, L. A. Influence of solvents on the intramolecular energy transfer in NADH and NADPH. *Biochim. Biophys. Acta BBA - Bioenerg.* **143**, 432–434 (1967).
36. Heiner, Z., Roland, T., Leonard, J., Haacke, S. & Groma, G. I. Kinetics of light-induced intramolecular energy transfer in different conformational states of NADH. *J. Phys. Chem. B* **121**, 8037–8045 (2017).
37. Cadena-Caicedo, A., Gonzalez-Cano, B., López-Arteaga, R., Esturau-Escofet, N. & Peon, J. Ultrafast fluorescence signals from β-dihydronicotinamide adenine dinucleotide: resonant energy transfer in the folded and unfolded forms. *J. Phys. Chem. B* **124**, 519–530 (2020).
38. Kulkarni, G. V., Ray, A. & Patel, C. C. Molecular orbital studies on nicotinic acid, nicotinamide and related compounds. *J. Mol. Struct.* **49**, 373–382 (1978).
39. Fülscher, M. P., Serrano-Andrés, L. & Roos, B. O. A theoretical study of the electronic spectra of adenine and guanine. *J. Am. Chem. Soc.* **119**, 6168–6176 (1997).
40. Cohen, B., Hare, P. M. & Kohler, B. Ultrafast excited-state dynamics of adenine and monomethylated adenines in solution: implications for the nonradiative decay mechanism. *J. Am. Chem. Soc.* **125**, 13594–13601 (2003).
41. Conti, I., Garavelli, M. & Orlandi, G. Deciphering low energy deactivation channels in adenine. *J. Am. Chem. Soc.* **131**, 16108–16118 (2009).
42. Brøndsted Nielsen, S. & Sølling, T. I. Are conical intersections responsible for the ultrafast processes of adenine, protonated adenine, and the corresponding nucleosides? *ChemPhysChem* **6**, 1276–1281 (2005).
43. Evans, N. L. & Ullrich, S. Wavelength dependence of electronic relaxation in isolated adenine using uv femtosecond time-resolved photoelectron spectroscopy. *J. Phys. Chem. A* **114**, 11225–11230 (2010).
44. Kang, H., Jung, B. & Kim, S. K. Mechanism for ultrafast internal conversion of adenine. *J. Chem. Phys.* **118**, 6717–6719 (2003).
45. Gustavsson, T., Sharonov, A., Onidas, D. & Markovitsi, D. Adenine, deoxyadenosine and deoxyadenosine 5′-monophosphate studied by femtosecond fluorescence upconversion spectroscopy. *Chem. Phys. Lett.* **356**, 49–54 (2002).
46. Improta, R., Santoro, F. & Blancafort, L. Quantum Mechanical Studies on the Photophysics and the Photochemistry of Nucleic Acids and Nucleobases. *Chem. Rev.* **116**, 3540–3593 (2016).
47. Stange, U. C. & Temps, F. Ultrafast electronic deactivation of UV-excited adenine and its ribo- and deoxyribonucleosides and -nucleotides: A comparative study. *Ultrafast Photoinduced Process. Polyat. Mol. Struct. Dyn. Spectrosc. Dedic. Wolfgang Domcke Occas. His 70th Birthd.* **515**, 441–451 (2018).
48. Meyer, H.-D., Manthe, U. & Cederbaum, L. S. The multi-configurational time-dependent Hartree approach. *Chem. Phys. Lett.* **165**, 73–78 (1990).
49. Beck, M. H., Jäckle, A., Worth, G. A. & Meyer, H.-D. The multi-configuration time-dependent Hartree (MCTDH) method: a highly efficient algorithm for propagating wavepackets. *Phys. Rep.* **324**, 1–105 (2000).
50. Meyer, H.-D., Gatti, F. & Worth, G. A. *Multidimensional Quantum Dynamics: MCTDH Theory and Applications*. (Wiley-VCH, Weinheim, 2009).
51. Meyer, H.-D. & Worth, G. A. Quantum molecular dynamics: propagating wavepackets and density operators using the multi-configuration time-dependent Hartree method. *Theor. Chem. Acc.* **109**, 251–267 (2003).
52. Worth, G. A., Meyer, H.-D., Köppel, H., Cederbaum, L. S. & Burghardt, I. Using the MCTDH wavepacket propagation method to describe multimode non-adiabatic dynamics. *Int. Rev. Phys. Chem.* **27**, 569–606 (2008).
53. Wang, H. & Thoss, M. Multilayer formulation of the multi-configuration time-dependent Hartree theory. *J. Chem. Phys.* **119**, 1289–1299 (2003).
54. Manthe, U. A multilayer multiconfigurational time-dependent Hartree approach for quantum dynamics on general potential energy surfaces. *J. Chem. Phys.* **128**, 164116 (2008).
55. Manthe, U. Layered discrete variable representations and their application within the multiconfigurational time-dependent Hartree approach. *J. Chem. Phys.* **130**, 054109 (2009).
56. Vendrell, O. & Meyer, H.-D. Multilayer multiconfiguration time-dependent Hartree method: Implementation and applications to a Henon–Heiles Hamiltonian and to pyrazine. *J. Chem. Phys.* **134**, 044135 (2011).
57. Köppel, H., Domcke, W. & Cederbaum, L. S. Multimode molecular dynamics beyond the born-oppenheimer approximation. in *Adv. Chem. Phys.* **57**, 59–246 (1984).
58. Köppel, H. Diabatic Representation: Methods For The Construction Of Diabatic Electronic States. in *Conical Intersections* 15 175–204 (World Scientific, 2004).
59. Shiozaki, T., Győrffy, W., Celani, P. & Werner, H.-J. Communication: extended multi-state complete active space second-order perturbation theory: Energy and nuclear gradients. *J. Chem. Phys.* **135**, 81106 (2011).
60. Sugita, Y. & Okamoto, Y. Replica-exchange molecular dynamics method for protein folding. *Chem. Phys. Lett.* **314**, 141–151 (1999).
61. Warshel, A. & Levitt, M. Theoretical studies of enzymic reactions: Dielectric, electrostatic and steric stabilization of the carbonium ion in the reaction of lysozyme. *J. Mol. Biol.* **103**, 227–249 (1976).
62. Crespo-Hernández, C. E., Cohen, B., Hare, P. M. & Kohler, B. Ultrafast excited-state dynamics in nucleic acids. *Chem. Rev.* **104**, 1977–2020 (2004).
63. Penfold, T. J., Gindensperger, E., Daniel, C. & Marian, C. M. Spin-vibronic mechanism for intersystem crossing. *Chem. Rev.* **118**, 6975–7025 (2018).
64. Yamazaki, S. & Kato, S. Solvent effect on conical intersections in excited-state 9h-adenine: radiationless decay mechanism in polar solvent. *J. Am. Chem. Soc.* **129**, 2901–2909 (2007).
65. Tuna, D., Sobolewski, A. L. & Domcke, W. Mechanisms of ultrafast excited-state deactivation in adenosine. *J. Phys. Chem. A* **118**, 122–127 (2014).
66. Jaiswal, V. K. et al. Environment-driven coherent population transfer governs the ultrafast photophysics of tryptophan. *J. Am. Chem. Soc.* **144**, 12884–12892 (2022).
67. Jimenez, R., Fleming, G. R., Kumar, P. V. & Maroncelli, M. Femtosecond solvation dynamics of water. *Nature* **369**, 471–473 (1994).
68. Cerezo, J. et al. Mixed quantum/classical method for nonadiabatic quantum dynamics in explicit solvent models: the ππ*/nπ* decay of thymine in water as a test case. *J. Chem. Theory Comput.* **14**, 820–832 (2018).
69. Borrego-Varillas, R. et al. Tracking excited state decay mechanisms of pyrimidine nucleosides in real time. *Nat. Commun.* **12**, 7285 (2021).
70. Rouxel, J. R. et al. Coupled electronic and nuclear motions during azobenzene photoisomerization monitored by ultrafast electron diffraction. *J. Chem. Theory Comput.* **18**, 605–613 (2022).
71. Borrego-Varillas, R. et al. Observation of the sub-100 femtosecond population of a dark state in a thiobase mediating intersystem crossing. *J. Am. Chem. Soc.* **140**, 16087–16093 (2018).
72. Borrego-Varillas, R., Ganzer, L., Cerullo, G. & Manzoni, C. Ultraviolet transient absorption spectrometer with sub-20-fs time resolution. *Appl. Sci.* **8**, 989 (2018).

73. Weingart, O. et al. COBRAMM 2.0 — A software interface for tailoring molecular electronic structure calculations and running nanoscale (QM/MM) simulations. *J. Mol. Model.* **24**, 271 (2018).
74. Avagliano, D., Bonfanti, M., Nenov, A. & Garavelli, M. Automatized protocol and interface to simulate QM/MM time-resolved transient absorption at TD-DFT level with COBRAMM. *J. Comput. Chem.* **43**, 1641–1655 (2022).
75. Frisch, M. J. et al. Gaussian 16. Gaussian, Inc. (2016).
76. Li Manni, G. et al. The OpenMolcas Web: A Community-Driven Approach to Advancing Computational Chemistry. *J. Chem. Theory Comput.* **19**, 6933–6991 (2023).
77. Plasser, F., Krylov, A. I. & Dreuw, A. libwfa: Wavefunction analysis tools for excited and open-shell electronic states. *WIREs Comput. Mol. Sci.* **12**, e1595 (2022).
78. Plasser, F., Mewes, S. A., Dreuw, A. & González, L. Detailed wave function analysis for multireference methods: implementation in the molcas program package and applications to tetracene. *J. Chem. Theory Comput.* **13**, 5343–5353 (2017).
79. Hsu, C.-P., You, Z.-Q. & Chen, H.-C. Characterization of the short-range couplings in excitation energy transfer. *J. Phys. Chem. C.* **112**, 1204–1212 (2008).
80. Worth, G. A., Beck, M. H., Jäckle, A. & Meyer, H.-D. The MCTDH Package, Version 8.2, (2000). H.-D. Meyer, Version 8.3 (2002), Version 8.4 (2007). O. Vendrell and H.-D. Meyer Version 8.5 (2013).
81. Worth, G. A. et al. The QUANTICS Package, Version 1.1, (University of Birmingham, Birmingham, U.K, 2015).
82. Jaiswal, V. K., et al. Sub-100-fs energy transfer in coenzyme NADH is a coherent process assisted by a charge-transfer state. *Nat. Commun.*, https://doi.org/10.6084/m9.figshare.25640532. (2024).

Acknowledgements

D.A. acknowledges Fundación Ramón Areces and Generalitat Valenciana/European Social Fund (APOSTD/2021/025) for fundings and ICCOM-CNR (Pisa)/ICMol-MolMatTC (Valencia) for hospitality. Support from the U.S. Department of Energy, Office of Science, Office of Basic Energy Sciences, Chemical Sciences, Geosciences and Biosciences Division under award no. DE-SC0022225 (A.N., F.M., S.M., V.K.J., and M.G.) is gratefully acknowledged. AN acknowledge financial support from PNRR MUR project ECS_00000033_ECOSISTER and from the Si-Fi-MYSTERY project, PRIN: PROGETTI DI RICERCA DI RILEVANTE INTERESSE NAZIONALE-Bando 2022, Prot. P2022WSJKS. G.C., F.S. and M.G. acknowledge financial support from the CRESCENDO project, PRIN: PROGETTI DI RICERCA DI RILEVANTE INTERESSE NAZIONALE-Bando 2022, Prot. 2022HL9PRP. G.C. and M.G. acknowledge financial support from the European Union – Next Generation EU – PNRR – M4C2, investimento 1.1 – "Fondo PRIN 2022" – "Understanding the pHotochemistry of sulfur substituted dnA bases by advanced ultrafast spectroscopy for phototherapeutic applications (HAPPY) ID P20224AWLB – CUP D53D23016720001".

Author contributions

P.K. build the experimental setup, V.P., P.K., L.U. performed the measurements, V.P., P.K. analyzed and interpreted the experimental data. V.K.J, D.A., F.M., and S.U. performed the computational simulations. V.K.J., D.A., F.S., M.G., S.M., and A.N. analyzed and discussed the computational simulations. D.A., S.M., A.N., M.G., and G.C. procured funding for the work. F.S., A.N., M.G., and G.C. supervised the project. V.K.J. and A.N. wrote the manuscript with inputs from all authors.

Competing interests

The authors declare no competing interests.

Additional information

Supplementary information The online version contains supplementary material available at https://doi.org/10.1038/s41467-024-48871-4.

Correspondence and requests for materials should be addressed to Giulio Cerullo, Marco Garavelli or Artur Nenov.

Peer review information *Nature Communications* thanks Dongho Kim and the other, anonymous, reviewer(s) for their contribution to the peer review of this work. A peer review file is available.

Supporting Information

Sub-100-fs energy transfer in coenzyme NADH is a coherent process assisted by a charge-transfer state.

Vishal Kumar Jaiswal[1], Daniel Aranda Ruiz[2‡], Vasilis Petropoulos[3‡], Piotr Kabaciński[3‡], Francesco Montorsi[1], Lorenzo Uboldi[3], Simone Ugolini[1], Shaul Mukamel[4], Giulio Cerullo[3,*], Marco Garavelli[1,*], Fabrizio Santoro[5], Artur Nenov[1,*]

[1]Dipartimento di Chimica industriale "Toso Montanari", Università di Bologna, Viale del Risorgimento 4, 40136 Bologna, Italy;

[2]ICMol, Universidad de Valencia, Catedrático José Beltrán Martínez, 2, 46980 Paterna, Spain;

[3]Dipartimento di Fisica, Politecnico di Milano, Piazza Leonardo da Vinci 32, 20133 Milano, Italy;

[4]Department of Chemistry and Department of Physics and Astronomy, University of California, Irvine, California 92697, United States;

[5]Istituto di Chimica dei Composti Organometallici (ICCOM-CNR), Area della Ricerca del CNR, Via Moruzzi 1, I-56124 Pisa, Italy;

‡ *These authors have equally contributed to this work*

** Corresponding authors: artur.nenov@unibo.it, marco.garavelli@unibo.it, giulio.cerullo@polimi.it*

Table of Contents

Suppl. Note. 1 Transient Absorption Experiment

1.1 TA map of UV-excited NADH in methanol

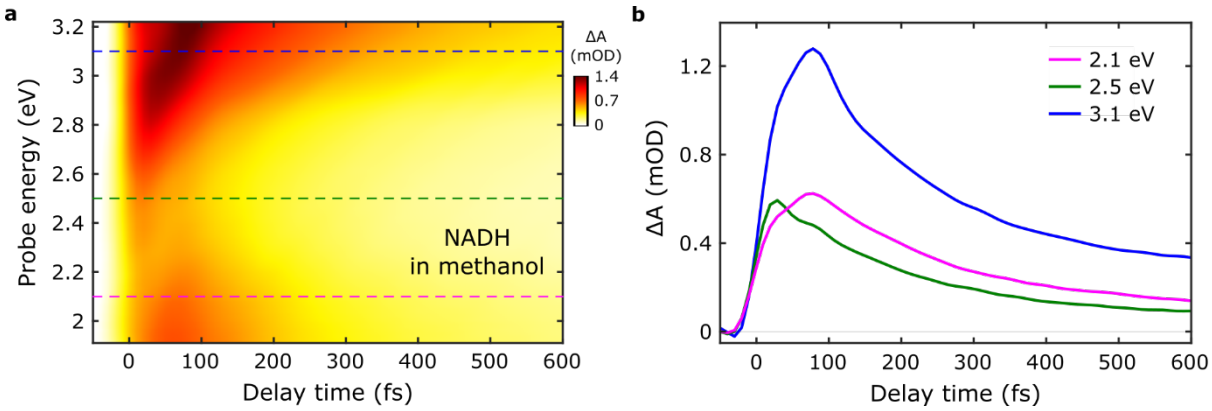

Suppl. Fig. 1: NADH in methanol upon 4.7 eV excitation, focusing the early time evolution. (a) TA map as a function of delay time and probe photon energy; (b) TA dynamics at selected probe photon energies, as highlighted in (a).

1.2 Global Fitting of UV-excited Adenosine and NADH dynamics

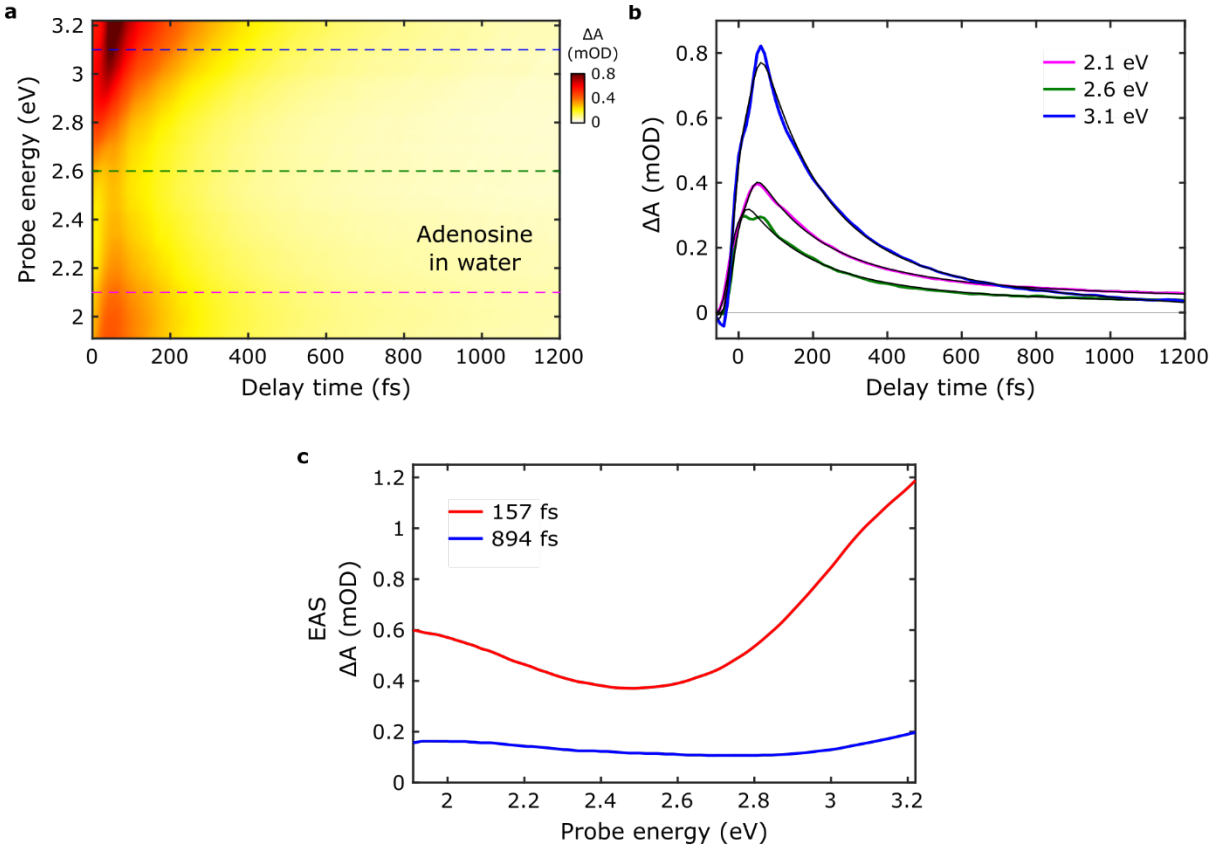

Suppl. Fig. 2: Global fitting results of adenosine in water upon 4.7 eV excitation. (a) TA map as a function of delay time and probe photon energy; (b) TA dynamics at specific probe photon energies, as highlighted in (a), overlapped with their fit (black line) extracted by global analysis. (c) Evolution

associated spectra (EAS) obtained from the global analysis of the TA data, with the corresponding time constants.

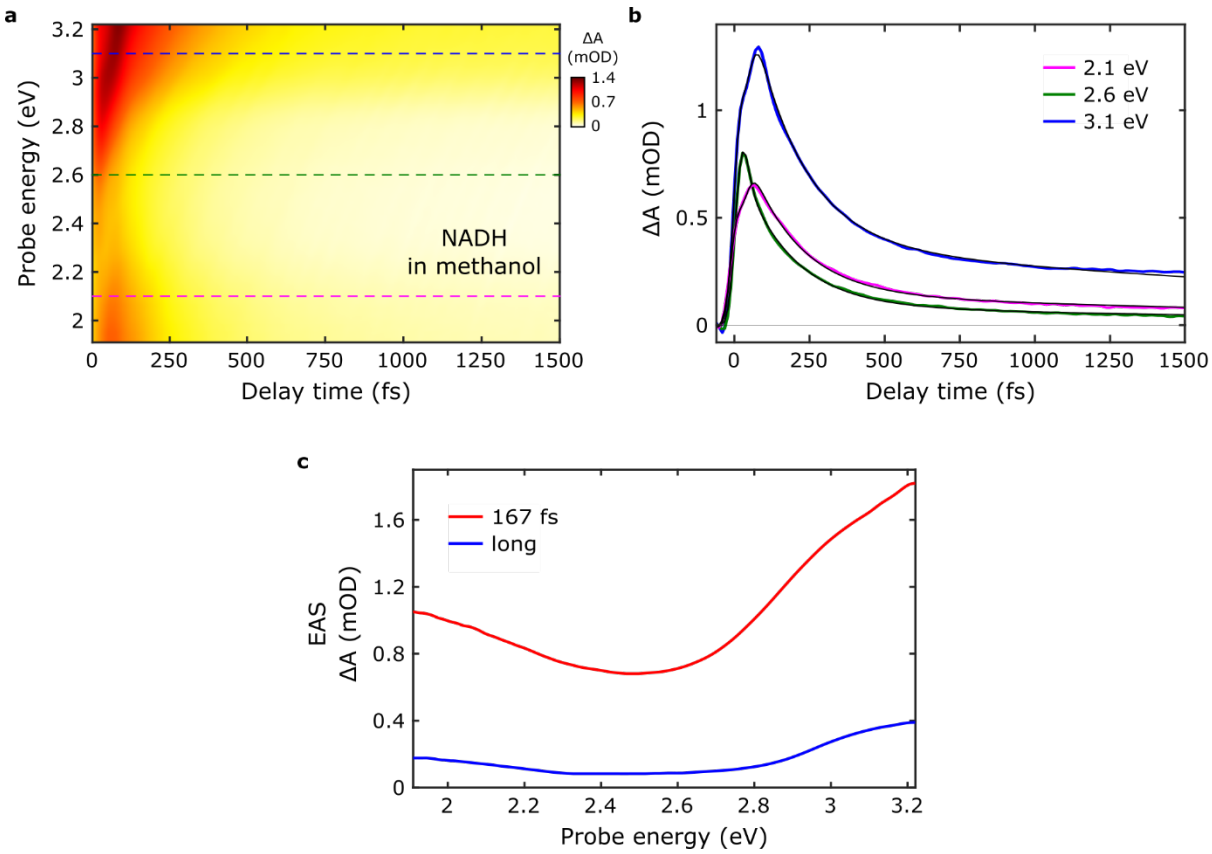

Suppl. Fig. 3: Global fitting results of NADH in methanol upon 4.7 eV excitation. (a) TA map as a function of delay time and probe photon energy; (b) Selected dynamics at specific probe photon energies, as highlighted in (a), overlapped with their fit (black line) extracted by global analysis. (c) EAS spectra obtained from the global analysis of the TA data, with the corresponding time constants.

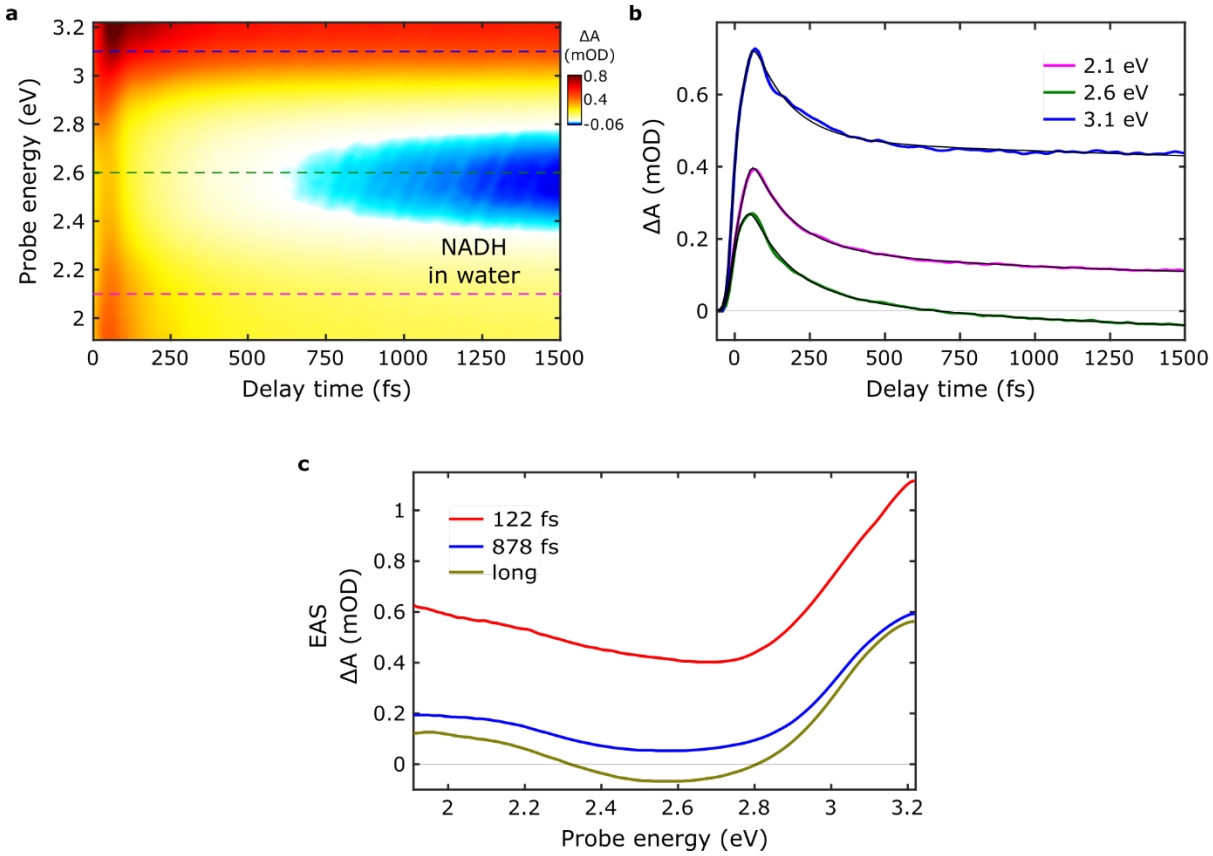

Suppl. Fig. 4: Global fitting results of NADH in water upon 4.7 eV excitation. (a) TA map as a function of delay time and probe photon energy; (b) TA dynamics at selected probe photon energies, as highlighted in (a), overlapped with their fit (black line) extracted by global analysis. (c) EAS spectral evolution obtained from the global analysis of the TA data, with the corresponding time constants.

	τ_1 (fs)	τ_2 (fs)	τ_3 (fs)
Adenosine in water	157 ± 4	894 ± 50	-
NADH in methanol	167 ± 4	-	long
NADH in water	122 ± 4	878 ± 40	long

Suppl. Table 1: Time constants, accompanied by their experimental uncertainty, as obtained from the global fitting of the TA data in case of Adenosine in water, NADH in methanol and NADH in water.

1.3 Estimation of the energy transfer timescale within the NADH dimer in water solvent (Adenine to Nicotinamide energy transfer)

NADH dissolved in water exists in an equilibrium between the folded and unfolded conformers. In such conditions, the folded conformers constitute approximately the 30% population and play a vital role in bridging the Adenine (Ade) and Nicotinamide (Nic) moieties, thereby enabling the energy transfer from Ade La-state to Nicotinamide excited state (Nic*). As mentioned in the main text, upon photoexcitation of NADH in water at 4.7 eV, two possible excited state pathways emerge (Scheme 1):

(i) Photoexcitation of the unfolded NADH conformers (70%). Taking into account the established negligible energy transfer in the open configuration[1]the ultrafast kinetics of the NADH unfolded conformers should retain a similar depopulation rate as Ade in water ($\boldsymbol{\tau}_{\text{NADH, unfolded}} \approx \boldsymbol{\tau}_{1\text{Ade, water}}$). The experimentally resolved ultrafast component of Adenosine's excited state in water (Suppl. Table 1), $\boldsymbol{\tau}_{1\text{Ade, water}}$ = 157 fs, corresponds to the main depopulation channel via internal conversion (IC) back to the ground state. Indeed, in our experiment for NADH dissolved in methanol, where NADH exists in open configuration, the Ade La-state possess a similar ultrafast component $\boldsymbol{\tau}_{1\text{NADH, methanol}}$ = 167 fs. The slight deviation in the latter lifetime with respect to the monomeric Ade in water can be attributed to the different solvent environment.

(ii) Photoexcitation of the folded NADH conformers (30%). In folded conformers, the excited state energy faces two concurrent dissipation channels: (a) Ade* IC back to the ground state and (b) ultrafast energy transfer from Ade* to Nic*. The competition between these two ultrafast processes is manifested in the TA measurements as an increase in the overall depopulation rate of the Ade La-state. We note that our pump pulse resonantly excites the Ade component in NADH dimer. Since the Ade depopulation is way faster than any other excited state relaxation events (e.g., vibrational cooling of Nic* takes place in picosecond timescales[1,2], we can safely assign the differences found between the $\boldsymbol{\tau}_1$ components of Adenosine and NADH in water solvent (Suppl. Table 1) to the presence of additional deactivation channels in Ade*. Indeed, for NADH in water we obtain $\boldsymbol{\tau}_{1\text{NADH, water}}$ = 122 fs from global analysis (Suppl. Table 1), a component faster than the net depopulation lifetime of the monomeric Ade* $\boldsymbol{\tau}_{1\text{Ade, water}}$ = 157 fs.

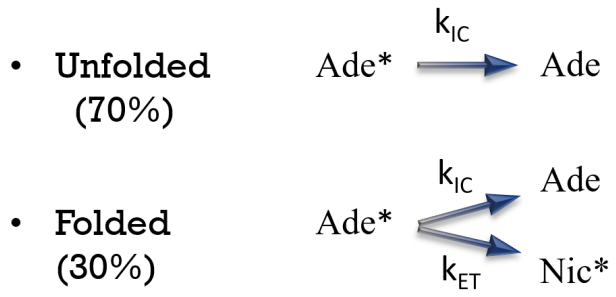

Scheme 1: Possible kinetic pathways of NADH in water following resonant Ade photoexcitation.

Thus, taking into account the 30/70 population ratio between folded/unfolded conformers of NADH in water, the $\boldsymbol{\tau}_{1\text{NADH, water}}$ = 122 fs lifetime extracted by global analysis can be considered as a weighted average of the folded and unfolded ultrafast lifetime components, simply given by:[3]

$$\boldsymbol{\tau_1}_{\text{NADH, water}} = 0.7\ \boldsymbol{\tau}_{\text{NADH, unfolded}} + 0.3\ \boldsymbol{\tau}_{\text{NADH, folded}} \quad \text{(Eq. 1)}$$

As we mentioned earlier, we can safely assign $\boldsymbol{\tau}_{\text{NADH, unfolded}} = \boldsymbol{\tau_1}_{\text{Ade, water}} = 157$ fs in Eq. 1, resulting in:

$$\boldsymbol{\tau}_{\text{NADH, folded}} = 40 \pm 6 \text{ fs} \quad \text{(Eq. 2)}$$

Accompanied by a value uncertainty retrieved through simple error propagation from the values of Suppl. Table 1.

The total decay rate of the folded NADH components ($\mathbf{k}_{\text{total}} = (40 \text{ fs})^{-1}$) reflects the sum of the Ade internal conversion ($\mathbf{k}_{\text{IC}} = (157 \text{ fs})^{-1}$) and the ultrafast energy transfer from Ade La-state to Nic* ($\mathbf{k}_{\text{ET}}$), given simply as:[1,3]

$$\mathbf{k}_{\text{total}} = \mathbf{k}_{\text{IC}} + \mathbf{k}_{\text{ET}} \quad \text{(Eq. 3)}$$

Resulting in an energy transfer from Ade La-state to Nic*:

$$\boldsymbol{\tau}_{\text{ET, folded}} = 54 \pm 11 \text{ fs} \quad \text{(Eq. 4)}$$

However, we should stress the 4.7 eV resonant excitation of the Ade moiety, might result in concurrent direct population of a small percentage of the Nic moiety. Taking into account that: (i) the absorption of Nic at 4.7 eV is ≈12 times lower in amplitude than its absorption peak around 3.6 eV [3,4](ii) the extinction coefficient of Ade in water at 4.7 eV (≈13000 $cm^{-1}\ M^{-1}$)[5] (iii) the extinction coefficient of NADH in water at 3.6 eV (≈6300 $cm^{-1}\ M^{-1}$)[6,7] ; the anticipated direct excitation of the Nic moiety is expected to be around 1/24 of the contribution of the Ade absorption at 4.7 eV. As a result, the 2 OD absorption at 4.7 eV in our experiment corresponds to 1.92 OD of Ade and 0.08 OD of Nic absorptions, respectively.

Despite the 4% of direct Nic population upon 4.7 eV excitation, the vibrational relaxation to the Nic minimum occurs in mere picoseconds[1,2] , at least one order of magnitude slower than the EET itself. This process may only influence the longer time constants of our global analysis, namely, the τ_2 and τ_3 components of Suppl. Table 1. Thus, the τ_1 time constant of NADH in water exclusively illustrates the additional deactivation channel found in Ade due to the presence of the EET, being unaffected by the small percentage (4%) of Nic direct excitation and without influencing the result of our master equation Eq.1.

Suppl. Note. 2 Replica Exchange Molecular Dynamics

The replica exchange dynamics were run using the protocol described for the simulation of dinucleosides.[8] The REMD simulations were done with integration time-steps of 4fs using hydrogen mass repartitioning (HMR) as outlined in the reference dynamical study. In total 20 ns of REMD were performed covering a temperature of 280 to 396 K over 18 replicas. The dynamics were post processed by extracting trajectories at 298 K.

2.1 Model Setup

The setup for MD consisted of NADH solvated in a truncated octahedral box of TIP3P water with an 8 Angstrom buffer space and then charge neutralized with 2 sodium ions. The parametrized forcefield parameters for NADH were taken from previously published works.[9,10] 18 replicas were setup with temperatures set at 280.00, 286.04, 292.18, 298.41, 304.74, 311.17, 317.69, 324.31, 331.03, 337.85, 344.79, 351.82, 358.97, 366.22, 373.59, 381.07, 388.67, and 396.40.

2.2 Pre-Equilibration at 298.15 K

All replicas were optimized with 1000 steps of steepest descent with 5 kcal/(mol·Å^2) positional restraints on NADH heavy atoms, followed by 15 ps of MD with same positional restraints at NVT ensemble. This was followed 3 optimizations of 1000 steps each with steepest descent with relaxing positional restraints of 2,0.1 and 0 kcal/(mol·Å^2) on NADH heavy atoms. Then a series of MD with relaxing positional restraints on heavy atoms were performed. 5ps of MD was done with 1 kcal/(mol·Å^2) positional restraints on NADH heavy atoms. This was followed by 1ns MD with 0.5 kcal restraints on NADH heavy atoms, then 1ns of MD with 0.5 kcal restraints on NADH backbone heavy atoms and then 1ns MD with no positional restraints. These series of dynamics were all done with integration timestep of 1fs except the last unconstrained MD where a timestep of 2fs was used. All MD steps were done by keeping the temperature at 298.15 K using the weak-coupling algorithm with 1ps time constant and using SHAKE to constrain the bonds involving hydrogen atoms. All MD simulations were done at NVT ensemble with periodic boundary conditions and PME with 8 Angstrom cutoff.

2.3 Equilibration at Replica temperature

The previous step results in 18 replicas at 298.15 K. For final equilibration step before running REMD, each replica was equilibrated from 298.15 K to the respective replica temperature (from 280 to 396 K) over 1ns. A Langevin thermostat with 2ps^{-1} collision frequency was employed. HMR was used to enable timestep of 4fs. The last structure from these dynamics were used to initiate REMD simulations.

2.4 Production (REMD)

REMD simulations were done for 18 replicas at temperatures mentioned above with 1ps exchange attempt interval. Dynamics were run with integration step of 4fs and HMR. The temperature was maintained by a Langevin thermostat with 2ps^{-1} collision frequency. All simulations were done at NVT ensemble with periodic boundary conditions and PME with 8 Angstrom cutoff. Simulations were performed for 20ns.

Suppl. Note. 3 Cluster Analysis

The dynamics were post processed by extracting trajectories at 298 K. which resulted in 2000 MD frames on which subsequent clustering was done using cpptraj program from AmberTools. Clustering was performed using DBSCAN[11] algorithm with an epsilon of 0.6, using the distance matrix of the solute atoms as a metric.

CLUSTERS from distance-matrix (DME) clustering // threshold = 0.6	**Percentage population in total REMD dynamics.**	**Median Interbase distance (ANGSTROM)**
Cluster C0	21.8	4.12
Cluster C1	13.1	4.73
Cluster C2	10.2	4.60
Cluster C3	6.1	4.18
Cluster C4	3.4	5.86
Cluster C5	2.3	4.48
Cluster C6	2.3	3.85
Cluster C7	0.9	8.45

Suppl. Table 2: Cluster population and mean interbase distance in Angstroms of various clusters from REMD dynamics

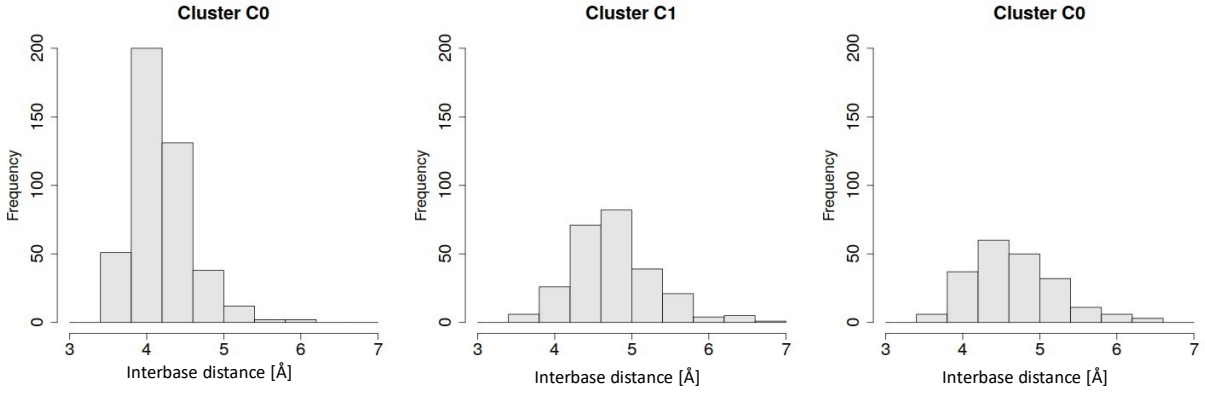

Suppl. Fig. 5 Distribution of inter-base distance in Angstroms for three largest clusters

Suppl. Note. 4 QM/MM Setup and Protocol for obtaining LVC parameters.

A QM/MM setup of a spherical droplet was made from the snapshots selected to enable ab-initio computations with electrostatic embedding. The spherical droplet consisted of 500 closest solvent molecules from the center of geometry of the solute. A High/Medium/Low layer partitioning was used where the high layer is described quantum mechanically and the medium and low layers through molecular mechanics force-fields. The medium layer is mobile during computations, while the low-layer is kept frozen. The high layer consisted of the two bases. The rest of the solute consisting of the backbone and nearest hydrogen-bonded waters were kept in the mobile medium layer, and the rest of the surrounding solvents were kept frozen in low-layer.

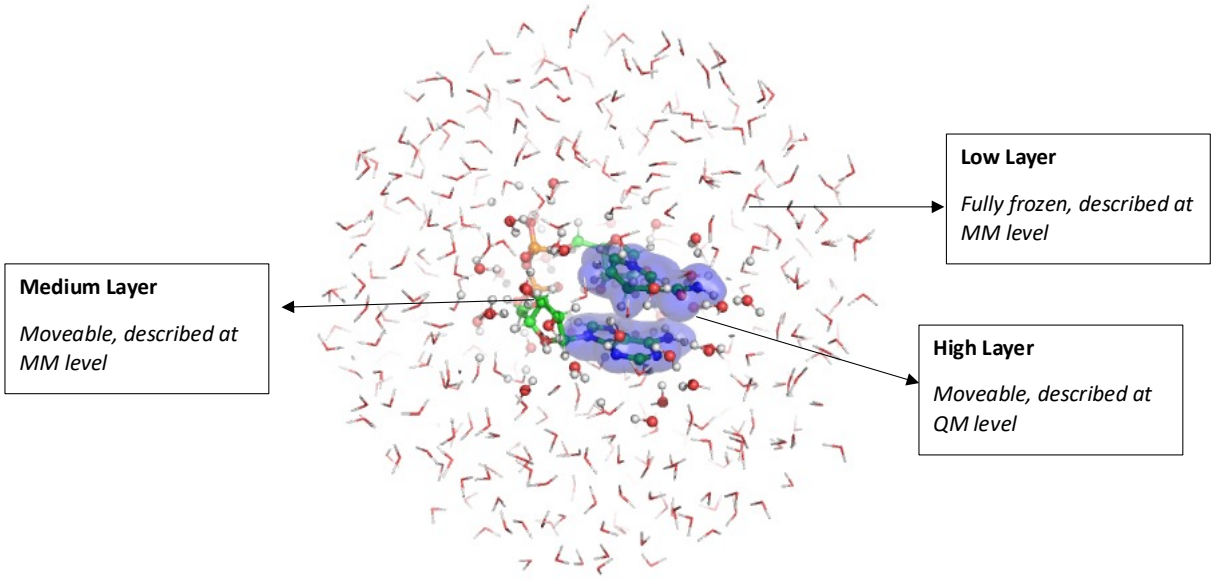

Suppl. Fig. 6 QM/MM setup used for optimizations where both High and Medium layer are moveable while Low layer is kept frozen. For energy and gradient computations to build the LVC model, only the high layer described at QM-level was movable, rest comprising backbone and solvent were kept frozen. The two chromophores are in High layer. The backbone of the nucleotide along with nearest water molecules shown with balls and sticks are in Medium layer. Rest of the water molecules shown with lines are in Low layer.

Using this QM/MM setup the ground-state was optimized at MP2 level of theory using 6-31G* basis-set. Post-optimization a frequency computation was done to obtain the normal-modes of the system. Only the frequency of the High-layer was computed owing to the ultrafast nature of the EET process. The frequency computations were done on every snapshot for which ML-MCTDH dynamics were performed to obtain system-specific normal modes accounting the effect of solute structure and environment. These system-specific normal modes were used to generate displaced structures on which electronic structure computations were done to obtain parameters for LVC Hamiltonian.

Suppl. Note. 5 Benchmarking of CASSCF active-space

To enable multiconfigurational excited-state computations, a selection of active-space orbitals is needed. The valence π-system of NADH consists of a large number of orbitals which have to be truncated to enable computations in reasonable time. To enable this, benchmark computations were done with full active-space using the RASPT2 methodology by putting all 15 occupied orbitals in RAS1 and 7 virtual orbitals in RAS3 and allowing 4 excitations. These benchmark computation on the stacked structure reveal a dark Nic->Ade charge transfer state between the bright La and Nic* state.

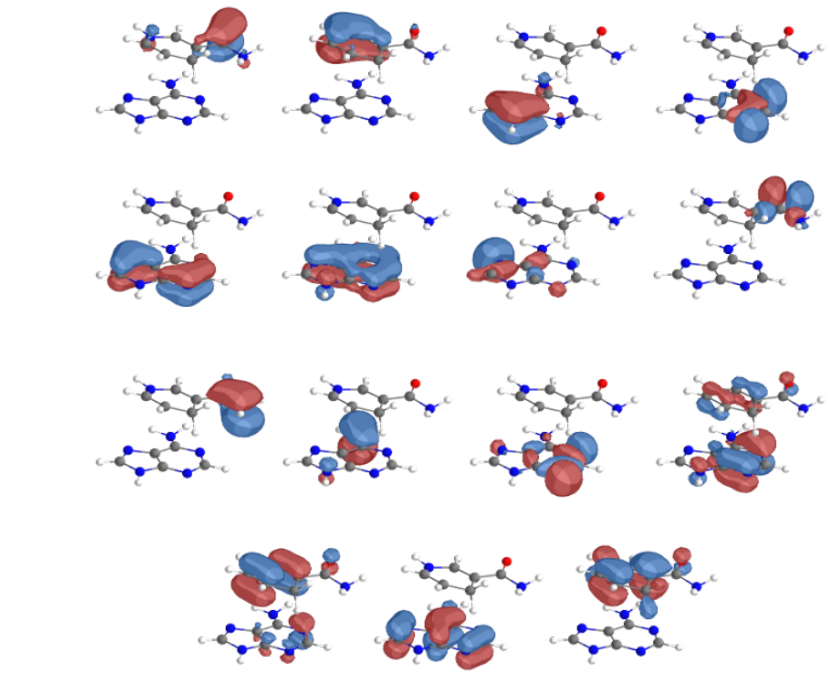

RAS1 ORBITALS

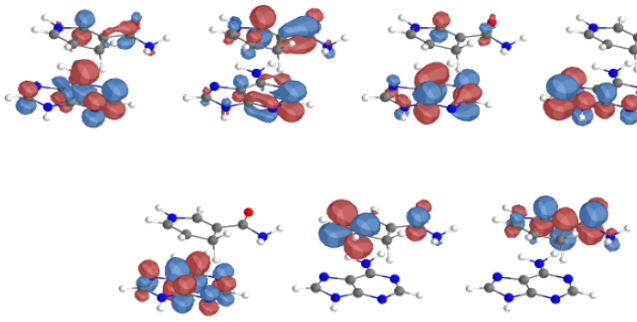

RAS3 ORBITALS

Suppl. Fig. 7 Active-Space orbitals of 4,15||4,7 RASPT2 computation

Natural Transition Orbital analysis reveal all the low-lying excitations relevant for ultrafast EET process to be described mainly by single transitions. Therefore, a reduced active space of |4,4| (4 electrons in 4 orbitals) was chosen to be a reasonable approximation. To enable smooth potentials at CASPT2 level, the XMS-CASPT2 level of theory was employed. A comparison of the vertical transitions for the chosen stacked snapshot with different active spaces are shown in Table 2. The level of underlying RAS/CAS theory is specified in the tables in the standard way as described below:

The various RAS subspaces are denoted as **RAS 1 | RAS2 | RAS3 ,**

a,b | c,d | e,f is a RASSCF computations with **b** orbitals in RAS1 space, **d** orbitals in RAS2 space and **f** orbital sin RAS3 space. There are **c** electrons in RAS2 space. A maximum of **a** excitations from RAS1 space and **e** excitations into RAS3 space is allowed.

	4,15||4,7	**|14,14|**	**|12,12|**	**|10,10|**	**|8,8|**	**|6,6|**	**|4,4|**
SSPT2	eV	eV	eV	eV	eV	eV	eV
Nic*	3.48	3.32	3.33	3.33	3.45	3.23	3.26
CT	4.76	5.37	5.45	5.54	4.87	4.76	4.77
La	5.05	5.15	5.27	5.25	5.04	5.05	4.93

Suppl. Table 3: Vertical Excitation energies at SS-CASPT2 level for various active spaces.

	SSPT2				**XMSPT2**		
	4,15||4,7	**|8,8|**	**|6,6|**	**|4,4|**	**|8,8|**	**|6,6|**	**|4,4|**
SSPT2	**eV**	eV	eV	eV	eV	eV	**eV**
Nic*	**3.48**	3.45	3.23	3.26	3.44	3.36	**3.40**
CT	**4.76**	4.87	4.76	4.77	4.92	4.86	**4.83**
La	**5.05**	5.04	5.05	4.93	5.14	5.00	**4.99**

Suppl. Table 4: Comparison between Vertical Excitation energies at SS-CASPT2 vs XMS-CASPT2 level for various active spaces. Note that XMS-CASPT2 with **|4,4|** active-space gives values comparable to the **reference 4,15||4,7** computation. Therefore, XMS-CASPT2 with a minimal |4,4| active-space was utilized in computations for gathering parameters for LVC Hamiltonian.

Suppl. Note. 6 Vertical Transition energies on cluster representatives

REP C0	eV *(f)*										AVG (eV)	σ (eV)
Nic*	3,61 *(0.13)*	3,48 *(0.13)*	3,82 *(0.11)*	3,59 *(0.12)*	3,57 *(0.13)*	3,74 *(0.13)*	3,60 *(0.14)*	3,74 *(0.11)*	3,43 *(0.14)*	3,63 *(0.13)*	3.62	0.12
CT	5,30 *(0.03)*	4,95 *(0.18)*	4,64 *(0.00)*	4,76 *(0.00)*	*5,15 (0.09)*	4,96 *(0.00)*	4,74 *(0.00)*	4,77 *(0.02)*	3,79 *(0.00)*	*5,16 (0.02)*	4.82	0.42
LA	5,07 *(0.56)*	5,04 *(0.42)*	5,00 *(0.60)*	5,10 *(0.59)*	*4,99 (0.52)*	5,44 *(0.60)*	4,98 *(0.60)*	5,02 *(0.57)*	4,89 *(0.59)*	*5,04 (0.58)*	5.06	0.15
LA-CT gap	-0,23	0,09	0,36	0,34	-0,16	0,48	0,24	0,25	1,10	-0,12		
REP C1												
Nic*	*3,83 (0.12)*	3,98 *(0.10)*	3,71 *(0.16)*	3,93 *(0.09)*	3,67 *(0.13)*	3,73 *(0.12)*	4,02 *(0.10)*	3,88 *(0.12)*	3,91 *(0.12)*	4,11 *(0.09)*	3.88	0.14
CT	*5,20 (0.18)*	4,52 *(0.02)*	5,98 *(0.00)*	4,72 *(0.08)*	*5,45 (0.10)*	5,38 *(0.03)*	4,46 *(0.00)*	4,89 *(0.14)*	5,17 *(0.04)*	*4,89 (0.00)*	5.06	0.48
LA	*5,03 (0.43)*	5,05 *(0.58)*	5,17 *(0.53)*	5,00 *(0.54)*	*5,20 (0.47)*	5,05 *(0.57)*	5,11 *(0.61)*	5,11 *(0.45)*	4,94 *(0.58)*	*4,99 (0.)*	5.06	0.08
LA-CT gap	0,10	0,53	-0,81	0,28	-0,25	-0,33	0,65	0,22	-0,23	0,10		
REP C2												
Nic*	3,83 *(0.13)*	3,75 *(0.14)*	3,60 *(0.14)*	3,46 *(0.17)*	3,61 *(0.17)*	3,69 *(0.16)*	3,77 *(0.16)*	3,78 *(0.17)*	3,83 *(0.13)*	3,55 *(0.15)*	3.69	0.13
CT	6,27 *(0.00)*	6,06 *(0.00)*	5,83 *(0.00)*	5,60 *(0.00)*	5,60 *(0.00)*	5,06 *(0.11)*	5,85 *(0.00)*	5,74 *(0.00)*	5,67 *(0.00)*	5,69 *(0.00)*	5.74	0.32
LA	5,05 *(0.59)*	5,02 *(0.60)*	5,28 *(0.58)*	4,89 *(0.60)*	4,76 *(0.58)*	4,99 *(0.49)*	4,93 *(0.59)*	4,90 *(0.59)*	5,03 *(0.60)*	4,94 *(0.60)*	4.98	0.14
LA-CT gap	-1,22	-1,04	-0,55	-0,71	-0,84	-0,07	-0,92	-0,84	-0,64	-0,75		

Suppl. Table 5 Vertical Transition Energies and Oscillator Strengths in brackets at XMS-CASPT2, with active-space of |4,4| for 10 solvated representatives of three most populated conformations denoted as REP C0-,C1 and C2 from REMD, along with the average (AVG) and standard deviation (σ) over the 10 representatives.

Suppl. Note. 7 Diabatization of LE and CT states

The LVC Hamiltonian for coupled for a coupled set of diabatic electronic states $|d\rangle=(|d_1\rangle, |d_2\rangle, \ldots, |d_N\rangle)$ may be written as

$$H = \sum_i (K + V_{ii}^{\mathrm{d}}(\boldsymbol{q}) \, |d_i\rangle\langle d_i|) + \sum_{i,j>i} V_{ij}^{\mathrm{d}}(\boldsymbol{q})(|d_i\rangle\langle d_j| + |d_j\rangle\langle d_i|) \qquad (1)$$

where **q** are the dimensionless normal mode coordinates, defined on the ground electronic state S0, with conjugate momenta **p**. The kinetic *K* and potential *V* terms of the Hamiltonian are defined as

$$K = \frac{1}{2} \boldsymbol{p}^{\mathrm{T}} \boldsymbol{\Omega} \boldsymbol{p} \quad (2)$$

$$V_{ii}^{\mathrm{d}}(\boldsymbol{q}) = E_{ii}^{\mathrm{d}}(0) + \lambda_{ii}^{\mathrm{T}}(\boldsymbol{q}) + \frac{1}{2} \boldsymbol{q}^{\mathrm{T}} \boldsymbol{\Omega} \boldsymbol{q} \quad (3)$$

$$V_{ij}^{\mathrm{d}}(\boldsymbol{q}) = E_{ij}^{\mathrm{d}}(0) + \lambda_{ij}^{\mathrm{T}}(\boldsymbol{q}) \qquad (4)$$

with $\boldsymbol{\Omega}$ being the diagonal matrix of normal mode frequencies ω_α , λ_{ij} being the vector of linear coupling constants, $E_{ii}^{\mathrm{d}}(0)$ being the diabatic energy of state *i* at the reference geometry (0 = Franck-Condon), and $E_{ii}^{\mathrm{d}}(0)$ being an electronic coupling constant between diabatic states *i* and *j* at the reference geometry (Franck-Condon). The coupling of electronic states at the reference geometry is the excitonic like term and referred to as **Electronic Coupling** in this work. The λ_{ij} term induces additional coupling between the electronic states due to normal modes **q** and is referred in this work as **Vibronic Coupling**.

The adiabatic states at XMS-CASPT2|4,4| level were diabatized to obtain pure LE (Nic*, La) and CT states. The diabatization was done by diagonalizing the matrix of Fragment Excitation Difference as outlined by Hsu et al.[12] In this method an excitation matrix Δx_{mn} is built, where the matrix elements are difference of excitation density ($\rho^{(mn)}$) between donor and acceptor.

$$\Delta \mathrm{x}_{\mathrm{mn}} = \int_{\mathrm{r}\epsilon \mathrm{D}} \rho_{\mathrm{ex}}^{(\mathrm{mn})}(\mathrm{r})\mathrm{dx} - \int_{\mathrm{r}\epsilon \mathrm{A}} \rho_{\mathrm{ex}}^{(\mathrm{mn})}(\mathrm{r})\mathrm{dx} \qquad (5)$$

For the diagonal elements the excitation density $\rho^{(mm)}$ is defined as sum of attachment and detachment densities, while for off-diagonal elements $\rho^{(mn)}$ is defined as the transition density between the states.

To conduct this protocol, the 1-electron transition density matrix (TDM) in molecular-orbital (MO) basis was obtained using the RASSI module of Openmolcas. To obtain attachment/detachment/transition densities localized on the fragment monomers, the TDM was converted from MO to atomic-orbital (AO) basis and the coefficients in this AO basis were summed to obtain the fraction of densities on two monomers.

The non-diagonal symmetric Δx_{mn} matrix obtained was diagonalized to give the rotation matrix **D** needed to transform the adiabatic states at Franck-Condon geometry [$\boldsymbol{q}$ = 0] to diabatic states.

$$\Delta \mathrm{x}_{\mathrm{mn}}^{diag} = \mathrm{D}^{-1} \Delta \mathrm{x}_{\mathrm{mn}} \mathrm{D} \quad (6)$$

This matrix **D** can be applied to transform the diagonal Hamiltonian in the adiabatic basis ψ at [$\boldsymbol{q}$ = 0] to a non-diagonal symmetric Hamiltonian matrix in diabatic basis ϕ at [$\boldsymbol{q}$ = 0] with energies and

interstate electronic couplings of diabatic LE and CT states. We utilized a *crude-diabatic* (in reference to crude-adiabatic approximation[13]) approximation for our quantum dynamics where these frozen diabatic states at Franck-Condon geometry $\phi[\mathbf{q} = 0]$ are the reference states amongst which the population transfer is monitored.

$$\mathrm{H}_{\phi[\boldsymbol{q}=0]} = \mathrm{D}^{-1}\mathrm{H}_{\psi[\boldsymbol{q}=0]}\mathrm{D} \qquad (7)$$

The above procedure gives us the energies of diabatic states and 0^{th}-order coupling of the LVC Hamiltonian, the coupling between diabatic states induced due to relative orientation the bases at FC geometry. This coupling is also referred as **Electronic Coupling** in this work.

To obtain the linear coupling constants λ_{ij}, we displace each normal coordinate α by some small value $\pm\Delta_\alpha$ and compute the energies of the adiabatic states giving us a diagonal Hamiltonian at $\mathbf{q} = \Delta_\alpha$. Then using two transformations as described below, this diagonal Hamiltonian is transformed to non-diagonal symmetric Hamiltonian in the previously described diabatic basis $\phi[\mathbf{q} = 0]$.

The overlap matrix **S** between the adiabatic states at displaced geometry along a normal mode [$\boldsymbol{q} = \Delta_\alpha$] and adiabatic states at Franck-Condon [$\boldsymbol{q} = 0$] was computed. This overlap matrix **S** was used to transform the diagonal Hamiltonian at displaced geometry to non-diagonal symmetric Hamiltonian in the basis of adiabatic states at [$\boldsymbol{q} = 0$]. Following this, this non-diagonal symmetric Hamiltonian in adiabatic basis of [$\boldsymbol{q} = 0$] was then further transformed to Hamiltonian in the basis of diabatic states at [$\boldsymbol{q} = 0$] through the previously computed rotation matrix **D.**

$$\mathrm{H}_{\phi[\mathrm{Q}_0]} = \langle\phi[Q_0]|\psi[Q_0]\rangle\,\langle\boldsymbol{\psi}[\boldsymbol{Q_0}]|\boldsymbol{\psi}[\boldsymbol{Q}]\rangle\,\mathrm{H}_{\psi[\mathrm{Q}=\Delta_\alpha]}\,\langle\boldsymbol{\psi}[\boldsymbol{Q_0}]|\boldsymbol{\psi}[\boldsymbol{Q}]\rangle^{-\mathbf{1}}\,\langle\phi[Q_0]|\psi[Q_0]\rangle^{-1}$$

$$= \mathrm{D}\,\mathbf{S}\,\mathrm{H}_{\psi[\mathrm{Q}]}\,\mathbf{S^{-1}}\,\mathrm{D}^{-1} \qquad (8)$$

The above procedure gives the gradients and additional couplings of the diabatic states induced by motion along the normal mode [Q_j] , also known as **Vibronic coupling.**

7.1 Electronic Coupling (V), Energy-gap (ΔE) and Mixing (V / ΔE) values for 100 different solute conformations of most populated cluster C0.

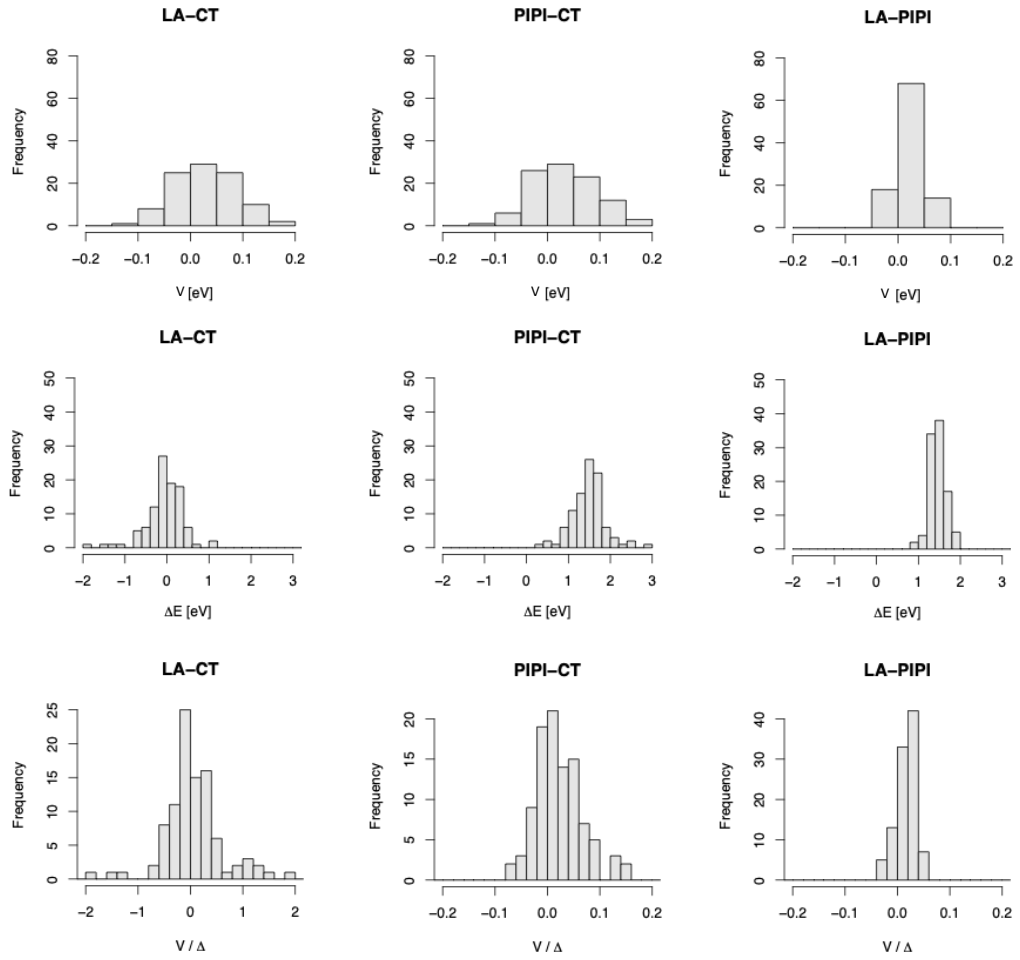

Suppl. Fig. 8 Electronic coupling, Energy gap , and mixing (V/delta) for 100 different solute conformations of most representative cluster in solvent. These are obtained by diabatizing the adiabatic states computed at |4,4|/XMS-CASPT2 level.

7.2 Adiabatic and diabatic states of frozen solute in 100 solvent ensemble.

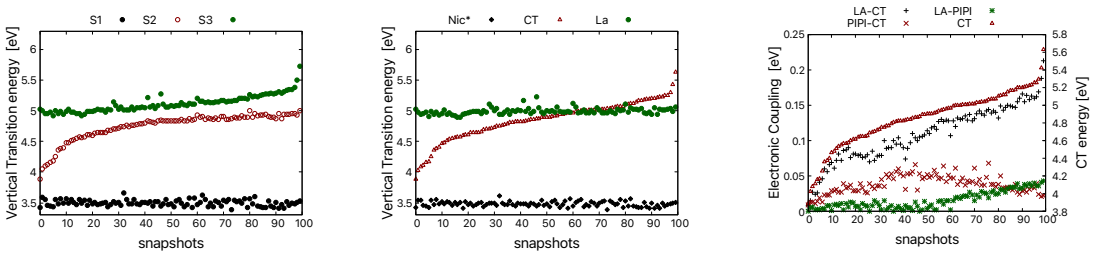

ADIABATIC DIABATIC COUPLING

Suppl. Fig. 9 Adiabatic, Diabatic states and Electronic coupling of a fixed solute geometry from most populated cluster in 100 different equilibrated solvent ensembles

Suppl. Note. 8 Wavepacket dynamics on Cluster representatives

ù

8.1 LVC parameters for dynamics on Cluster representatives in diabatic basis

	Nic* **(eV)**	**CT** **(eV)**	**La** **(eV)**	**La-CT** **(eV)**	**CT-Nic*** **(eV)**	**La-Nic*** **(eV)**
Cluster C0						
1	3.82	4.63	5.00	-0.06	0.01	0.01
2	3.57	5.12	5.01	0.01	0.06	-0.04
3	3.74	5.43	4.95	0.00	0.00	0.00
4	3.60	4.74	4.97	0.00	0.00	-0.01
5	3.74	4.77	5.01	0.06	0.02	-0.04
6	3.43	3.81	4.87	0.01	-0.02	-0.14
Cluster C1						
1	3.71	5.97	5.17	0.00	0.06	0.03
2	3.92	4.75	4.96	-0.02	-0.09	-0.03
3	3.67	5.39	5.25	0.02	0.03	0.10
4	3.98	4.39	5.01	0.00	0.00	0.00
5	3.90	5.14	4.95	-0.05	0.06	0.03
6	4.10	4.88	4.98	-0.02	0.00	0.03
Cluster C2						
1	3.75	6.05	5.01	0.00	0-.01	0.00
2	3.45	5.59	4.88	0.00	0.00	0.00
3	3.61	5.59	4.75	-0.01	0.00	0.00
4	3.69	5.06	4.99	0.00	0.00	0.00
5	3.77	5.73	4.89	0.01	-0.02	0.03
6	3.54	5.68	4.94	0.00	0.00	0.00

Suppl. Table 6: LVC parameters (vertical excitation energy in columns 2-4 and interstate electronic coupling matrix elements in columns 5-7) for ML-MCTDH dynamics on cluster representatives shown in next section.

8.2 Wavepacket dynamics for CT-mediated EET including all coupling terms in vibronic Hamiltonian in diabatic-basis.

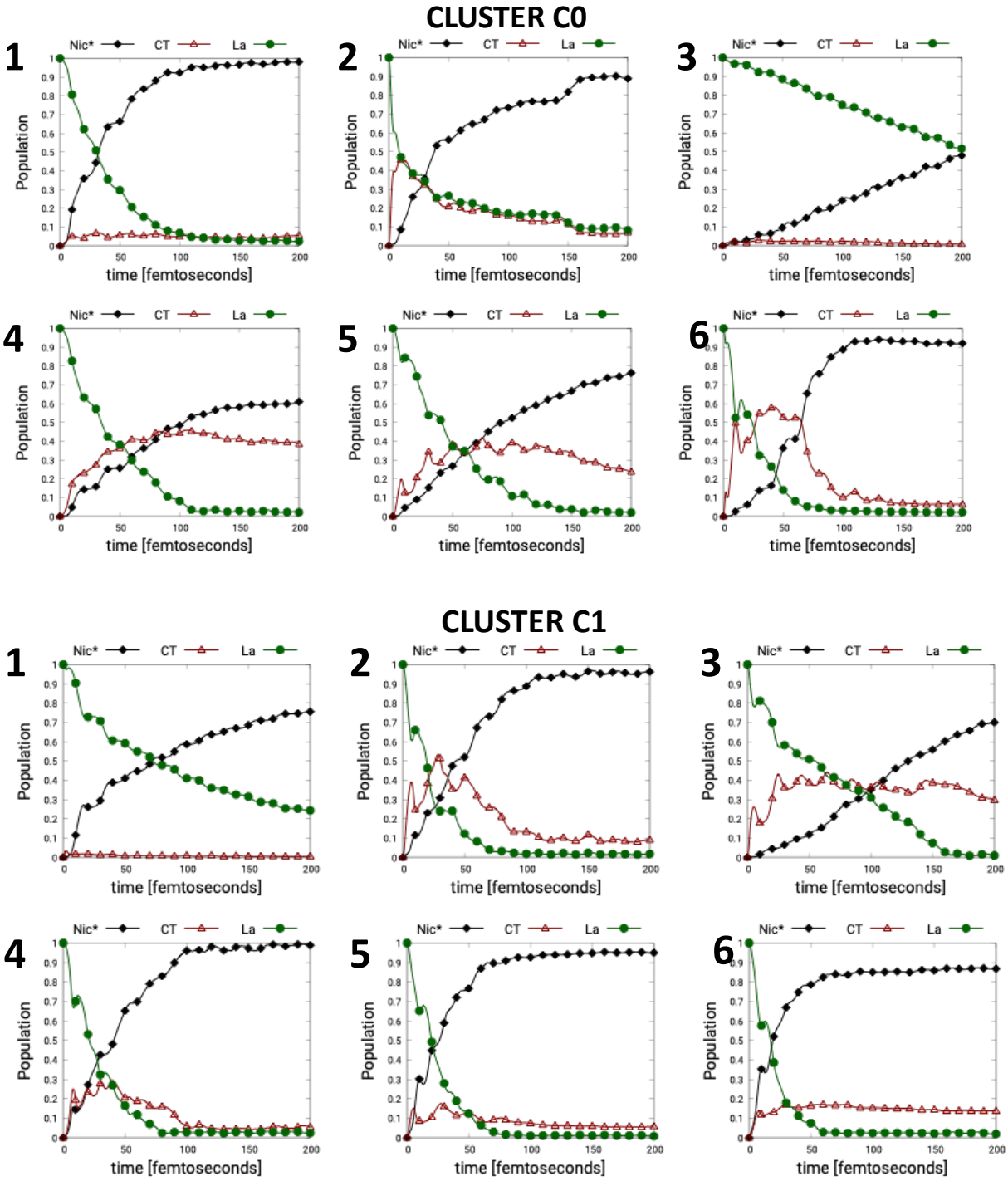

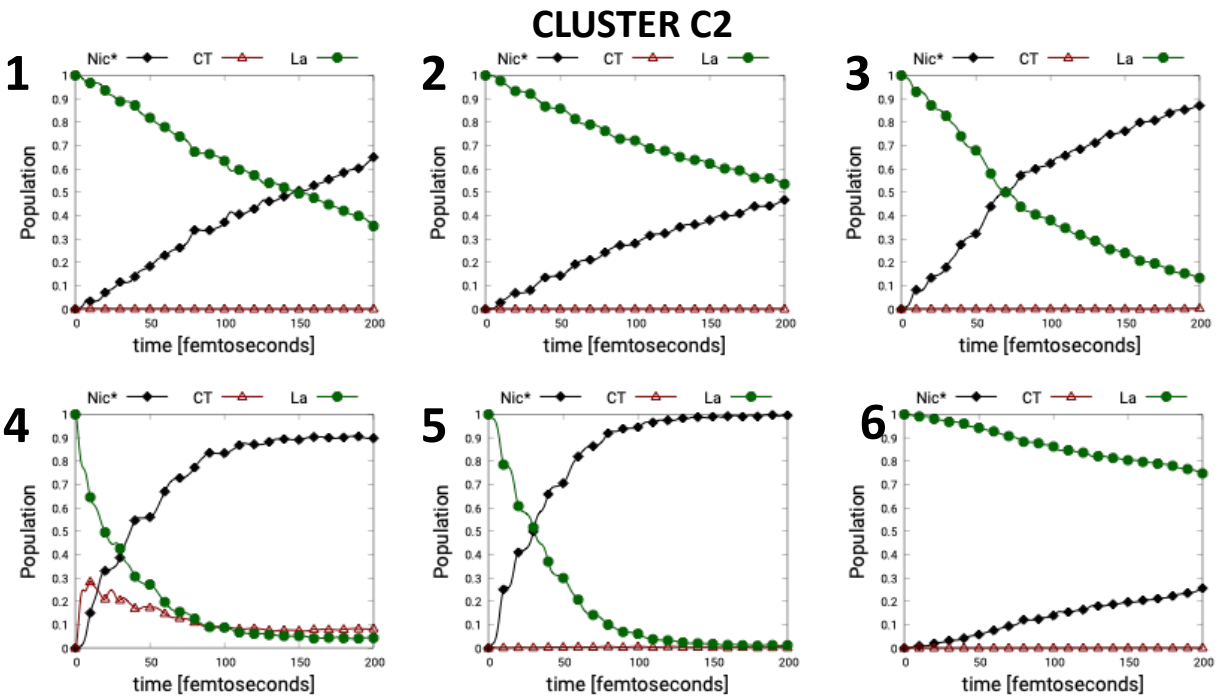

Suppl. Fig. 10: ML-MCTDH dynamics including all 3 electronic states and all coupling and gradient terms. The dynamics are labeled (**1,2** etc) according to Suppl. Table 6

8.3 Wavepacket dynamics for Direct EET including all coupling terms in vibronic Hamiltonian in diabatic-basis.

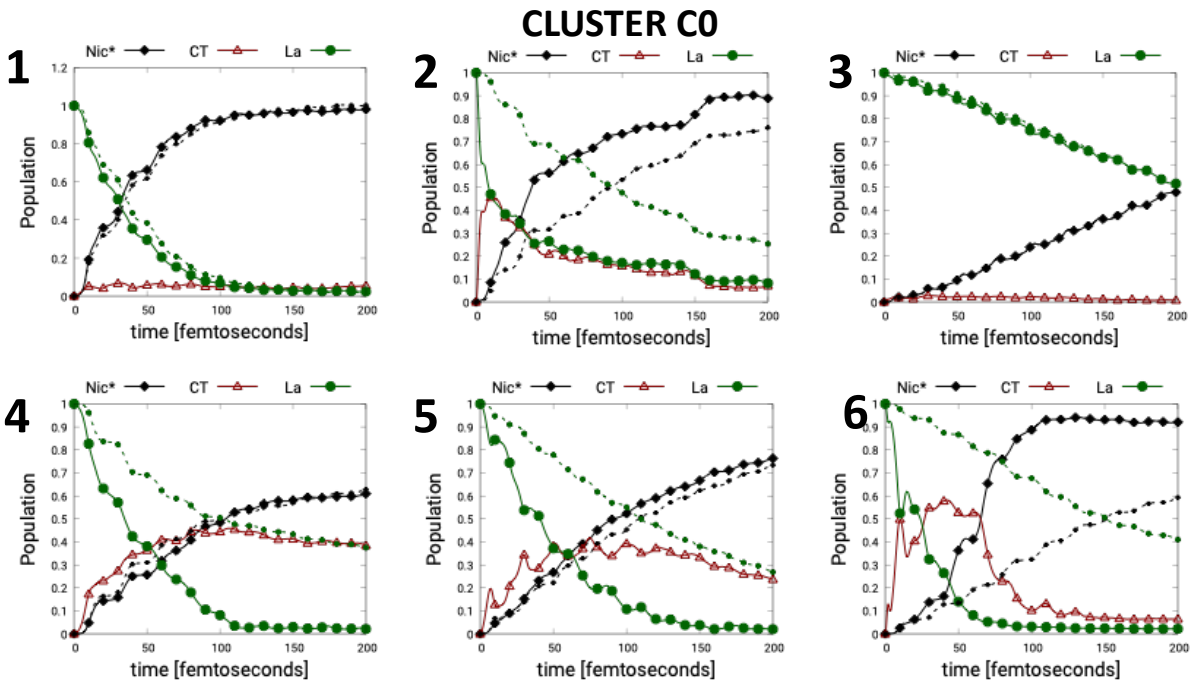

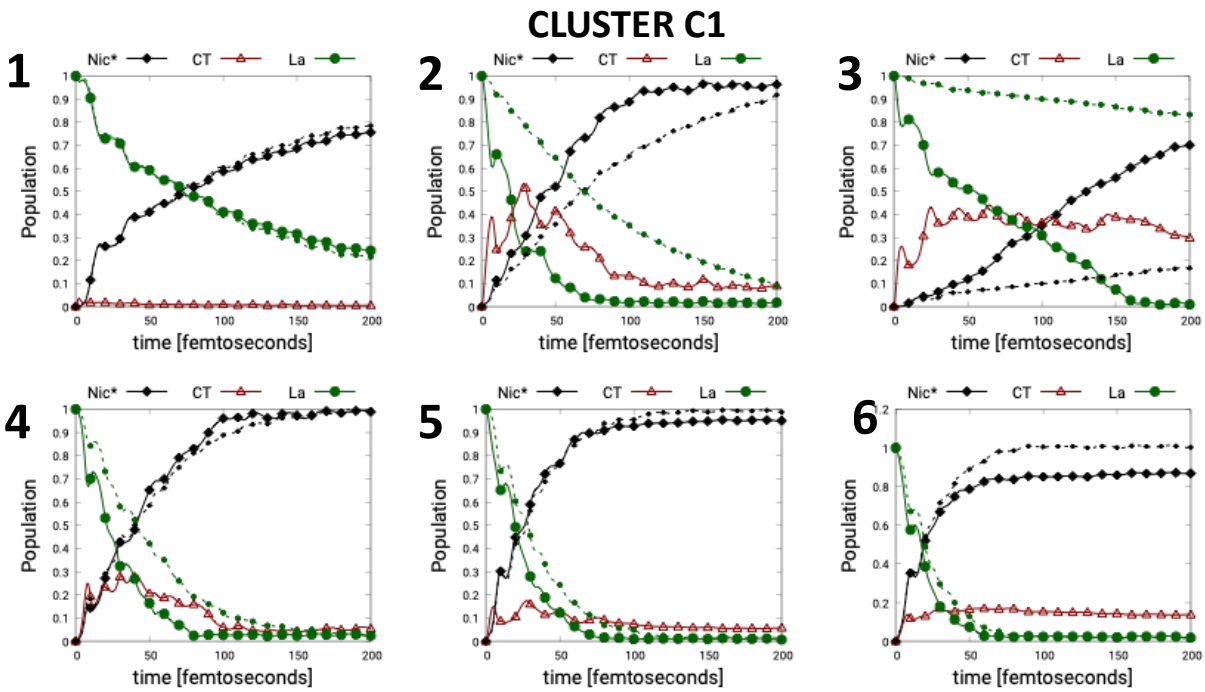

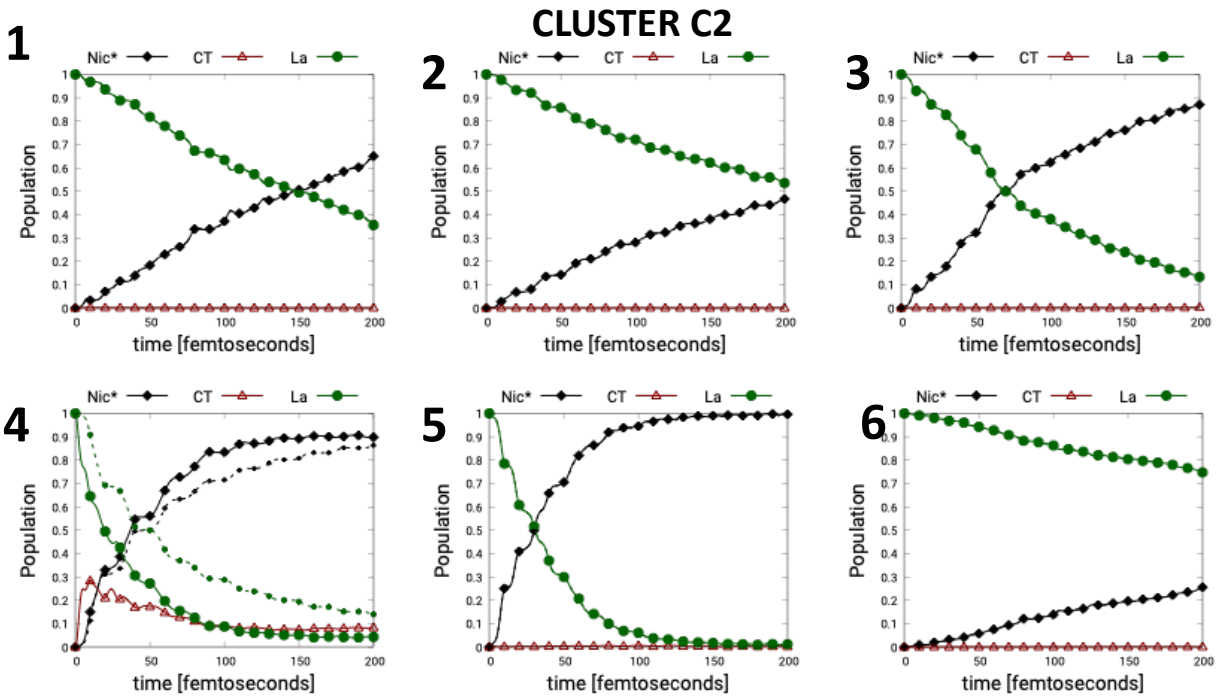

Suppl. Fig. 11: Solid line: ML-MCTDH dynamics with three electronic states and all coupling/gradient terms. Dashed line: ML-MCTDH dynamics with two electronic states (NO CT) simulating Direct Transfer and respective gradient and all interstate coupling terms.

Suppl. Note. 9 Energies of diabatic states along example ML-MCTDH dynamics.1.

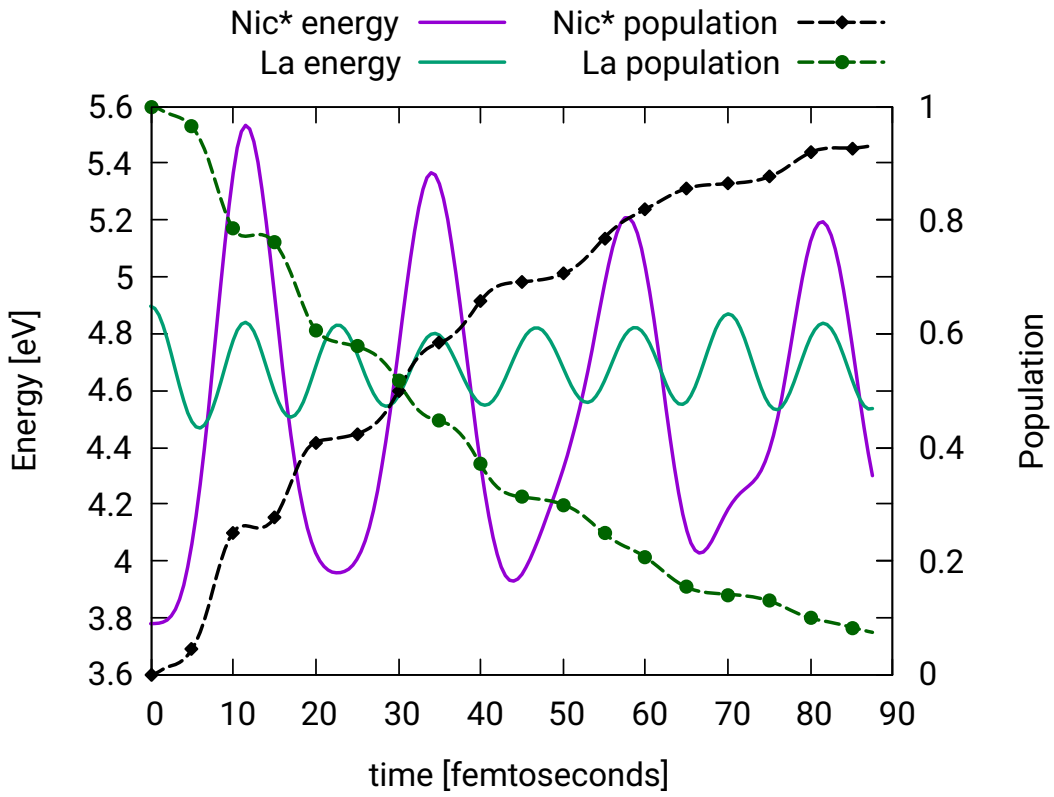

Suppl. Fig. 12: Energies of Nic* and La state along ML-MCTDH dynamics for a representative structure (Cluster C2 / Struct5). The population transfer mainly happens around the times when La and Nic* energies become degenerate.

Suppl. Note. 10 Selective effects of Interstate Electronic/Vibronic Coupling on wavepacket dynamics.

To explore the selective effects of Electronic Coupling (*coupling between diabatic LE/CT states due to inter-base orientation at Franck-Condon geometry*) or Vibronic Coupling (*additional coupling induced due to photo-excited normal modes of the system*), these terms were switched ON or OFF in the Hamiltonian. This is accomplished by removing the respective terms from the operator file in ML-MCTDH dynamics.

Cluster C0
Structure 01

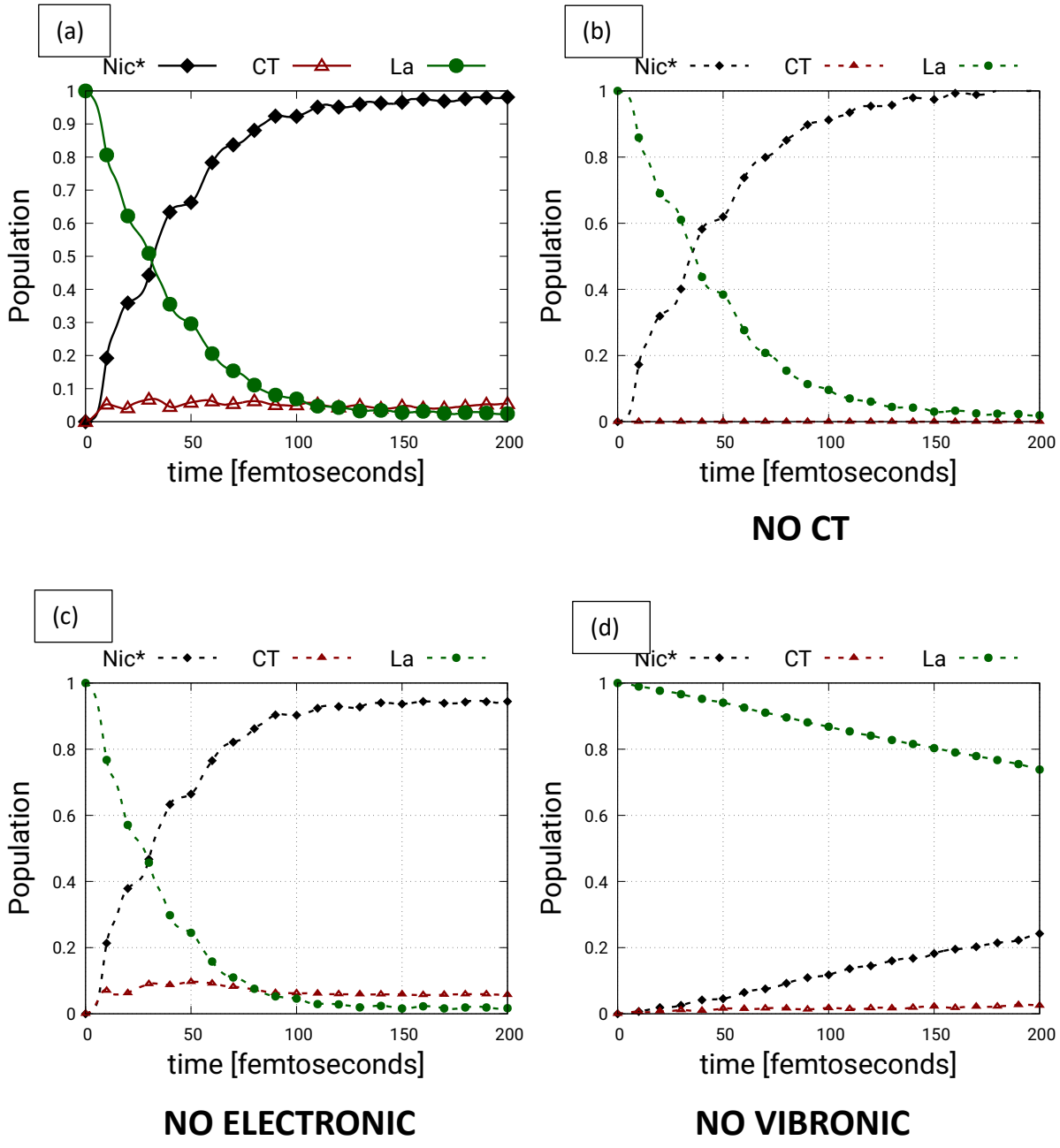

Suppl. Fig. 13.1: (a) ML-MCTDH dynamics will coupling terms and the three electronic states. (b) ML-MCTDH dynamics with all coupling (between L_a and Nic*) terms but NO CT state (c) ML-MCTDH dynamics after removing all electronic coupling terms (off-diagonal terms of electronic hamiltonian) (d) ML-MCTDH dynamics after removing all vibronic terms (gradients and coupling terms of vibronic hamiltonian)

Cluster C0
Structure 02

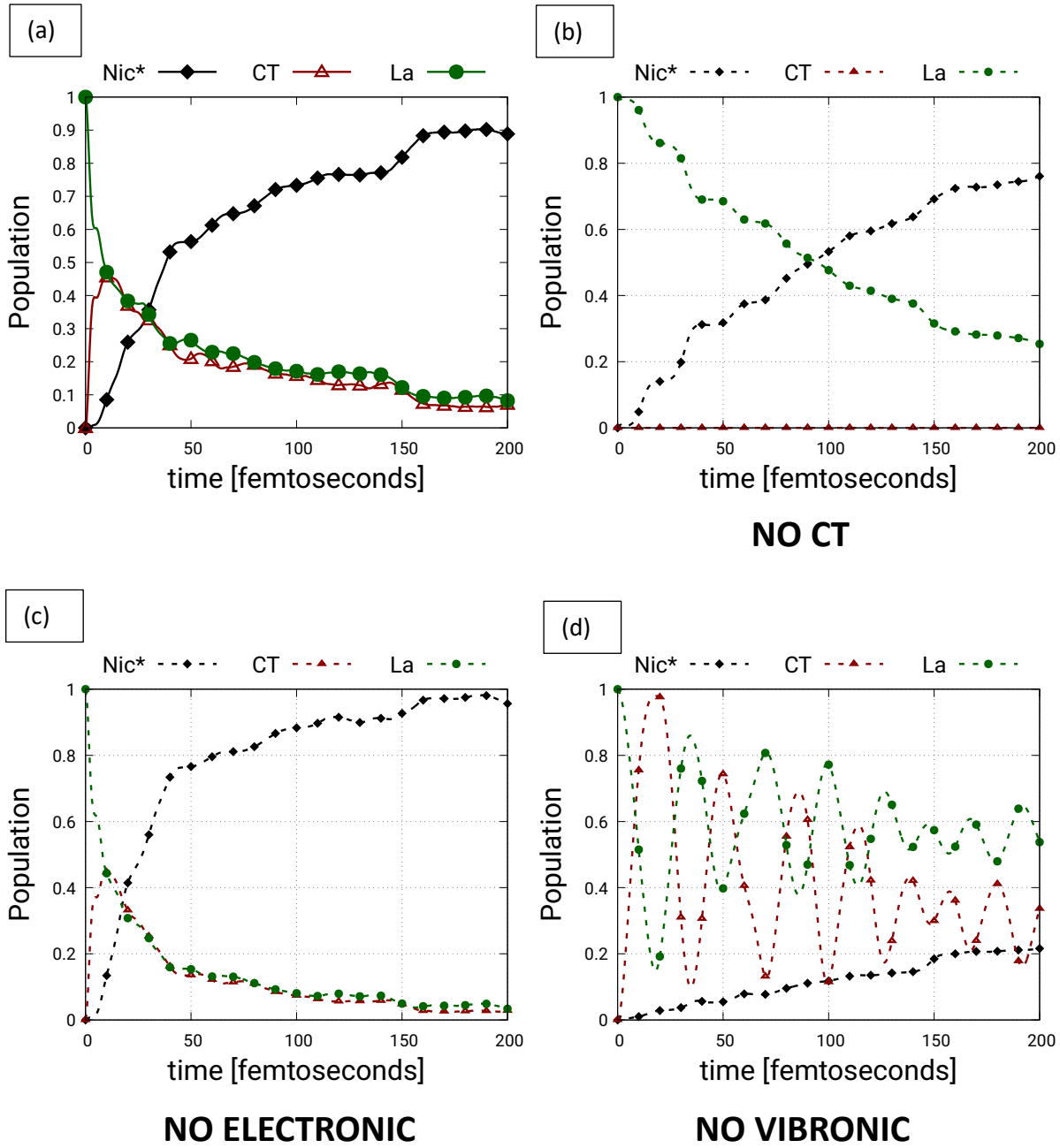

Suppl. Fig. 13.2: Caption same as Suppl. Fig. 13.1

Cluster C0
Structure 03

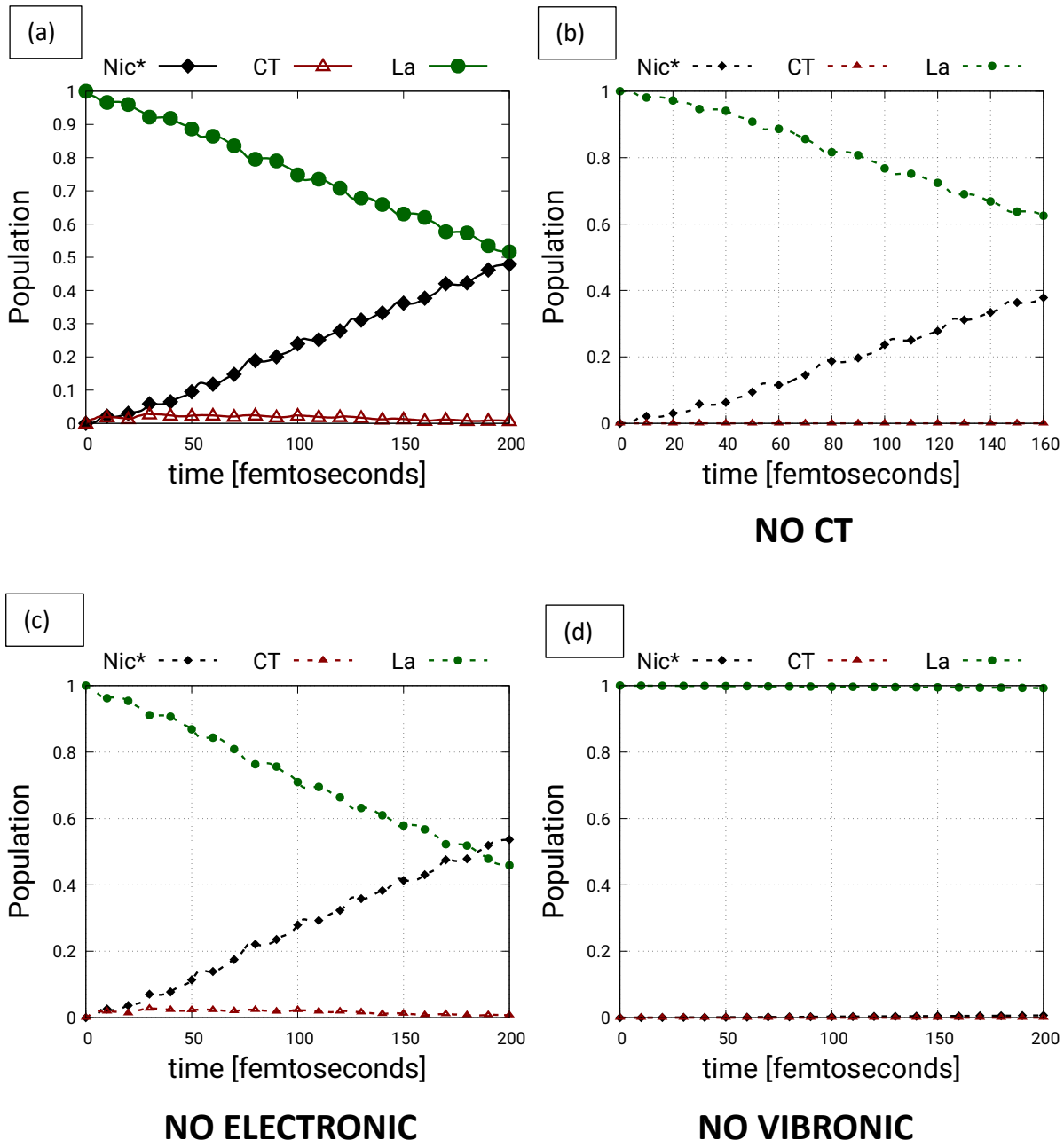

Suppl. Fig. 13.3 : Caption same as Suppl. Fig. 13.1

Cluster C0
Structure 04

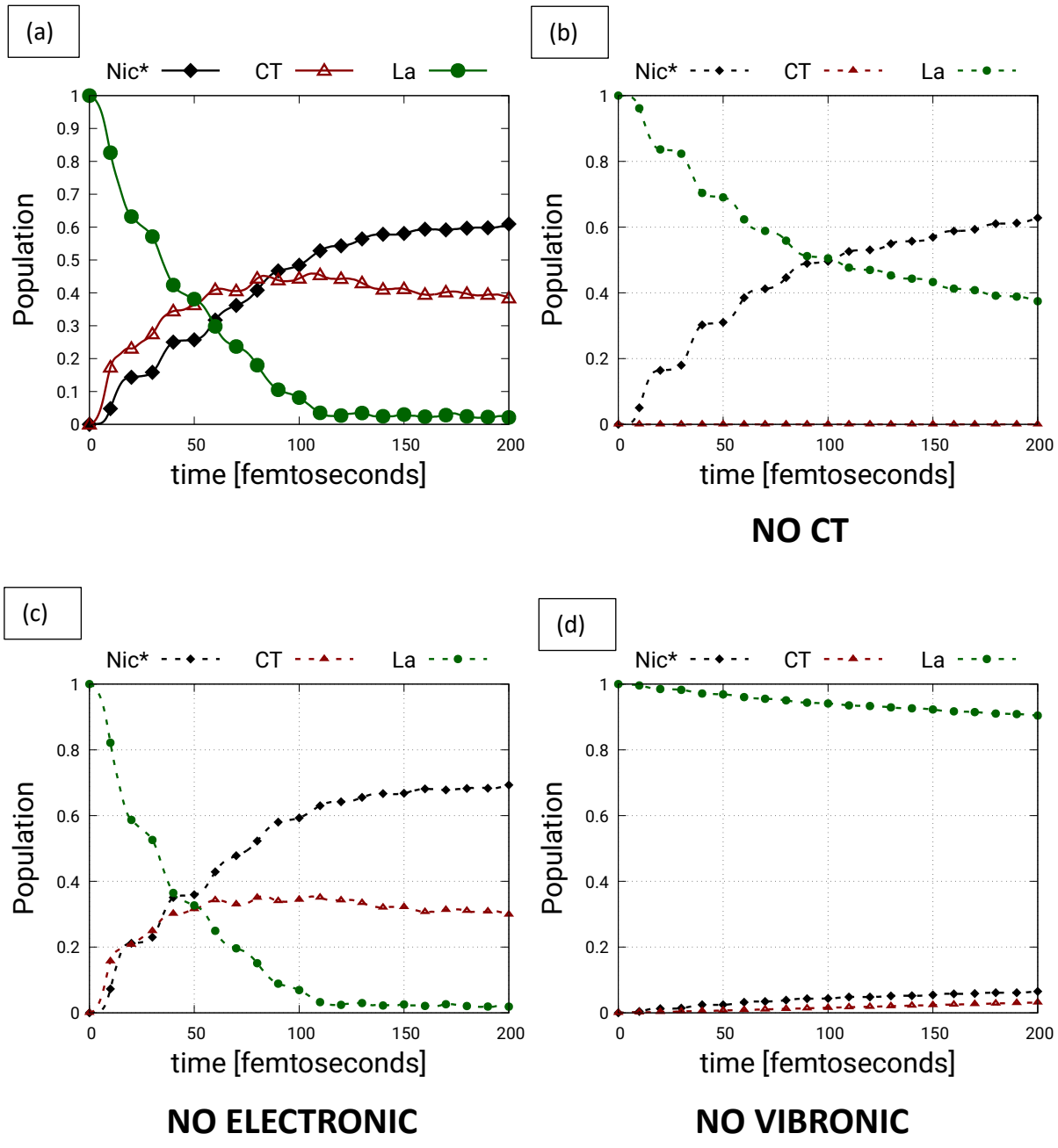

Suppl. Fig. 13.4: Caption same as Suppl. Fig. 13.1

Cluster C0
Structure 05

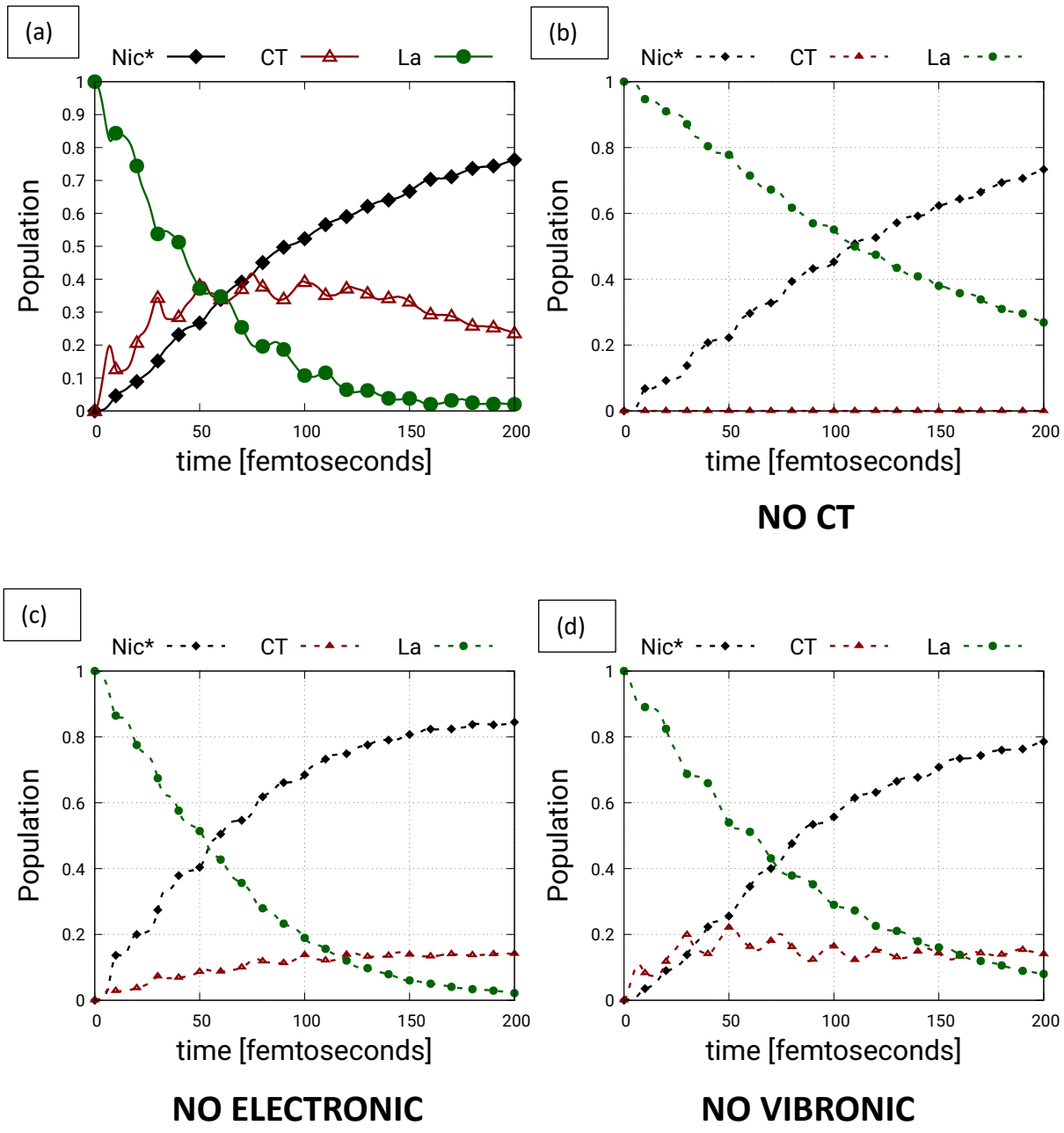

Suppl. Fig. 13.5: Caption same as Suppl. Fig. 13.1

Cluster C0
Structure 06

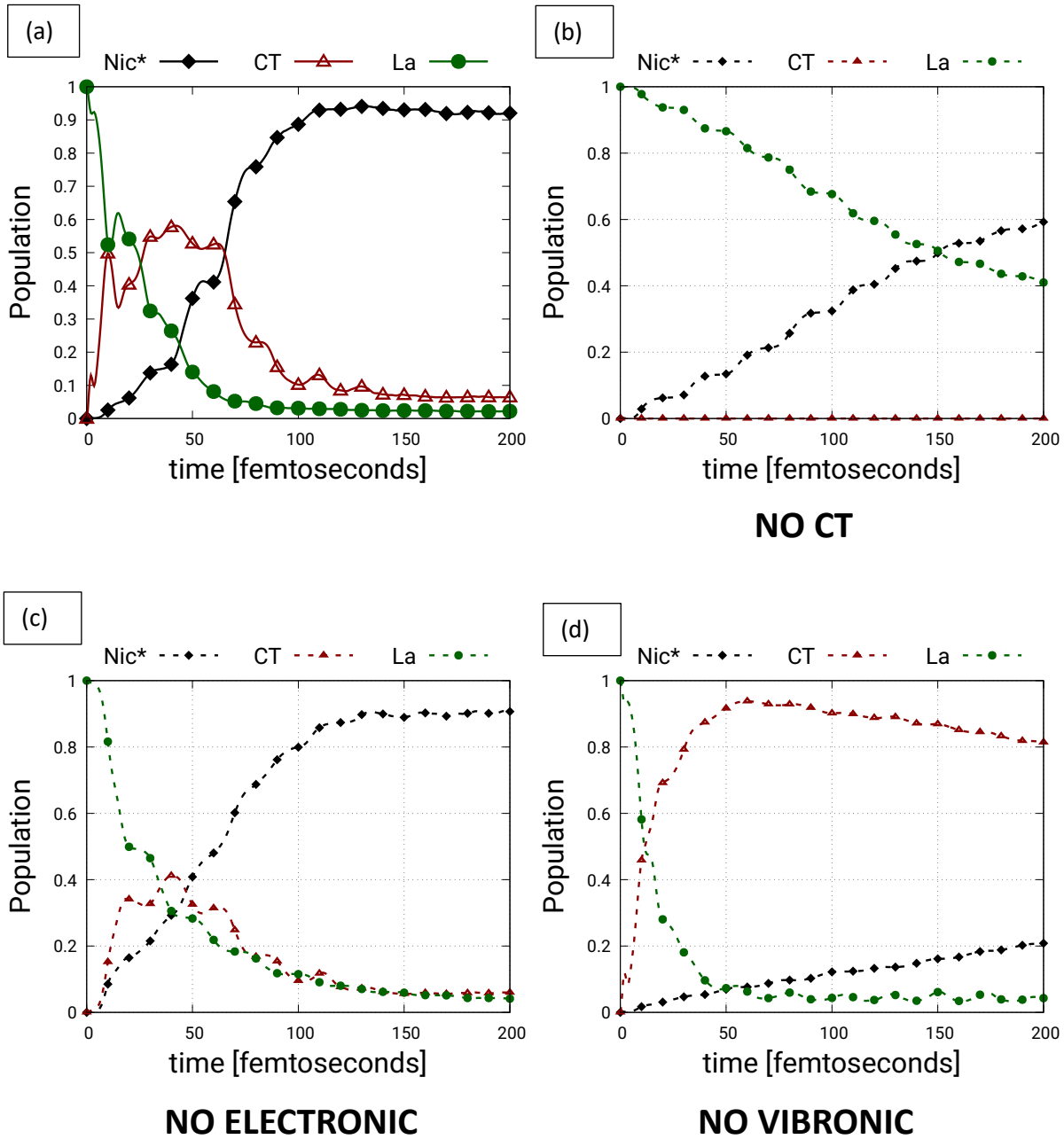

Suppl. Fig. 13.6: Caption same as Suppl. Fig. 13.1

Cluster C1
Structure 01

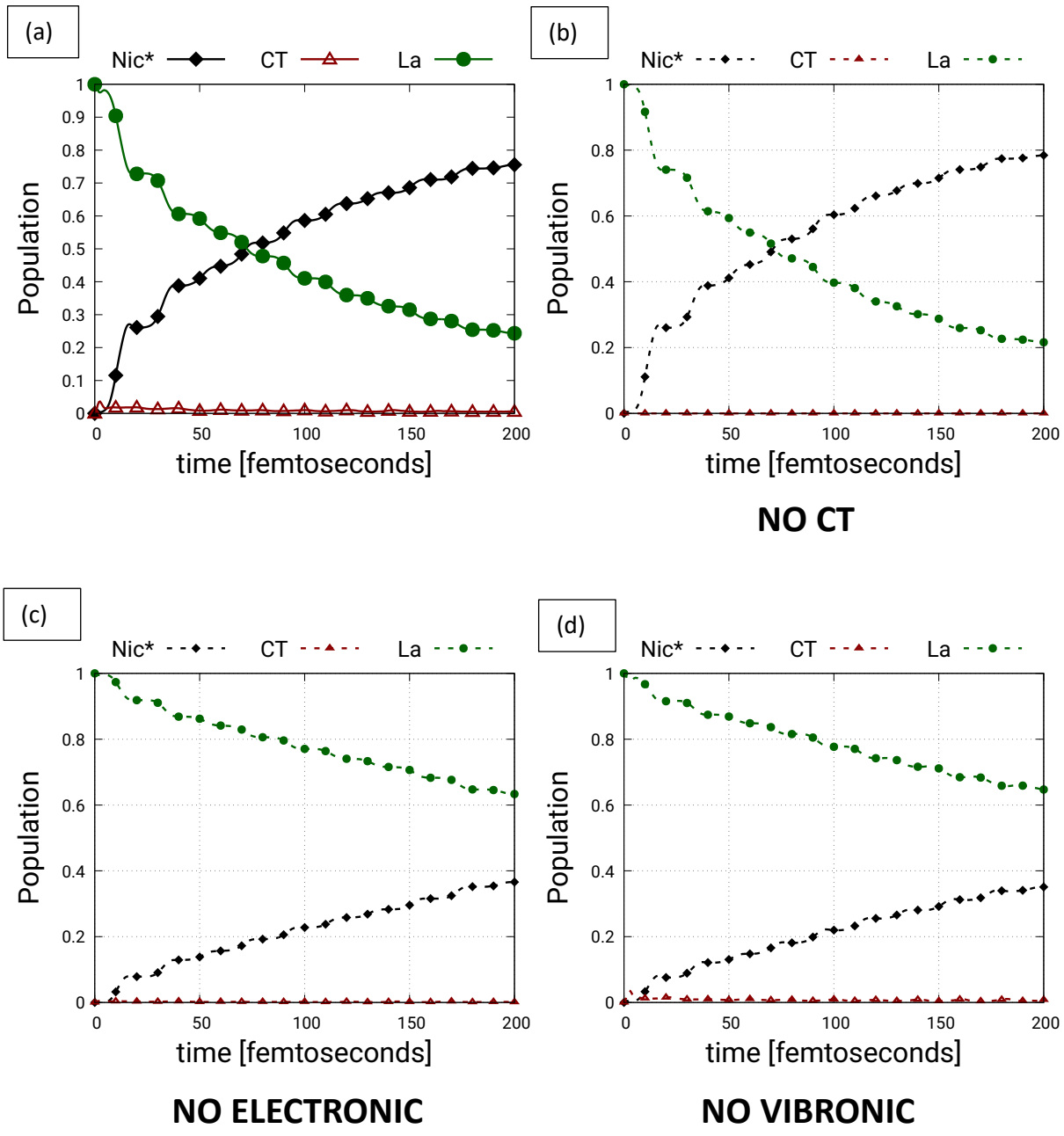

Suppl. Fig. 13.7: Caption same as Suppl. Fig. 13.1

Cluster C1
Structure 02

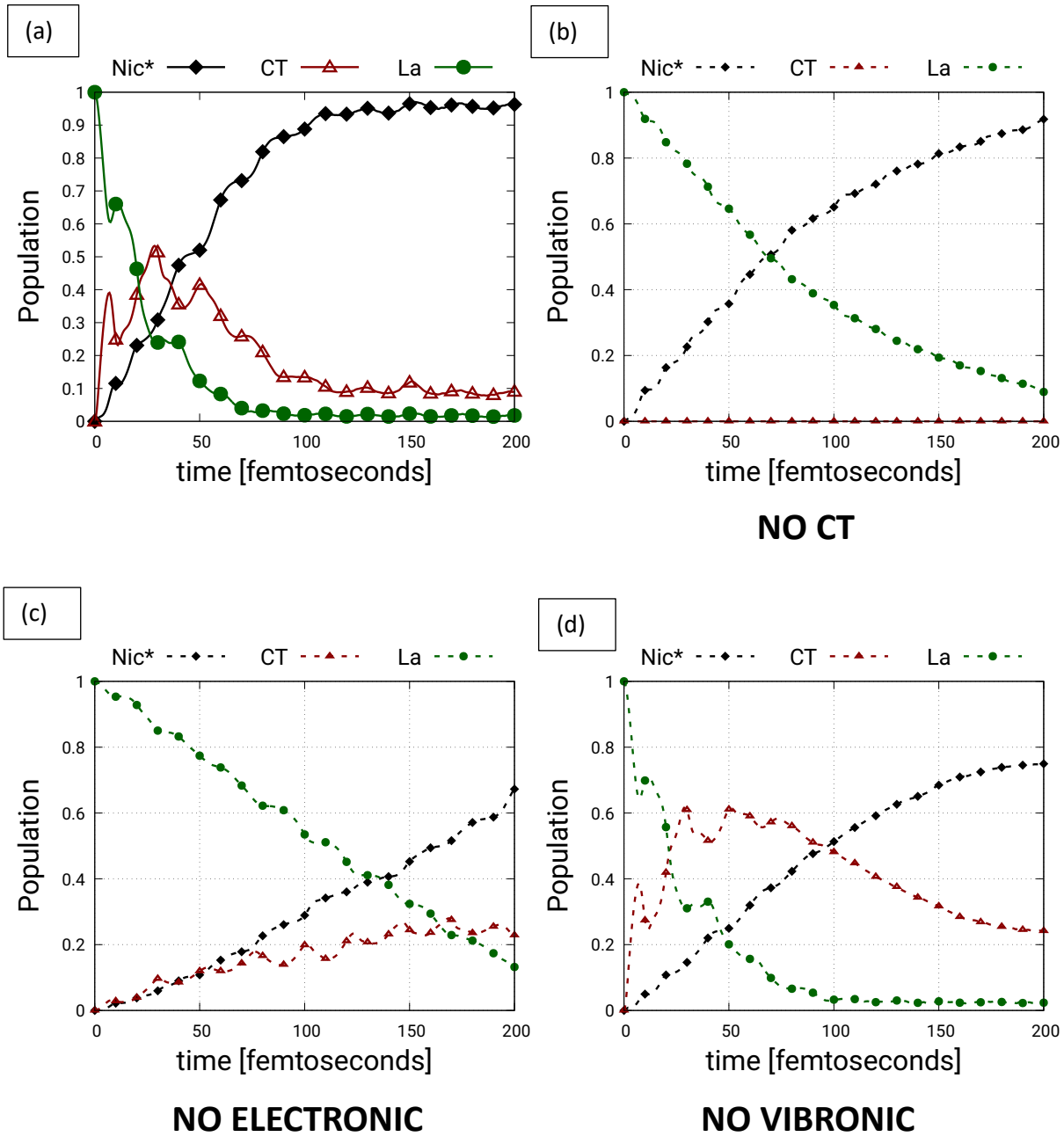

Suppl. Fig. 13.8: Caption same as Suppl. Fig. 13.1

Cluster C1
Structure 03

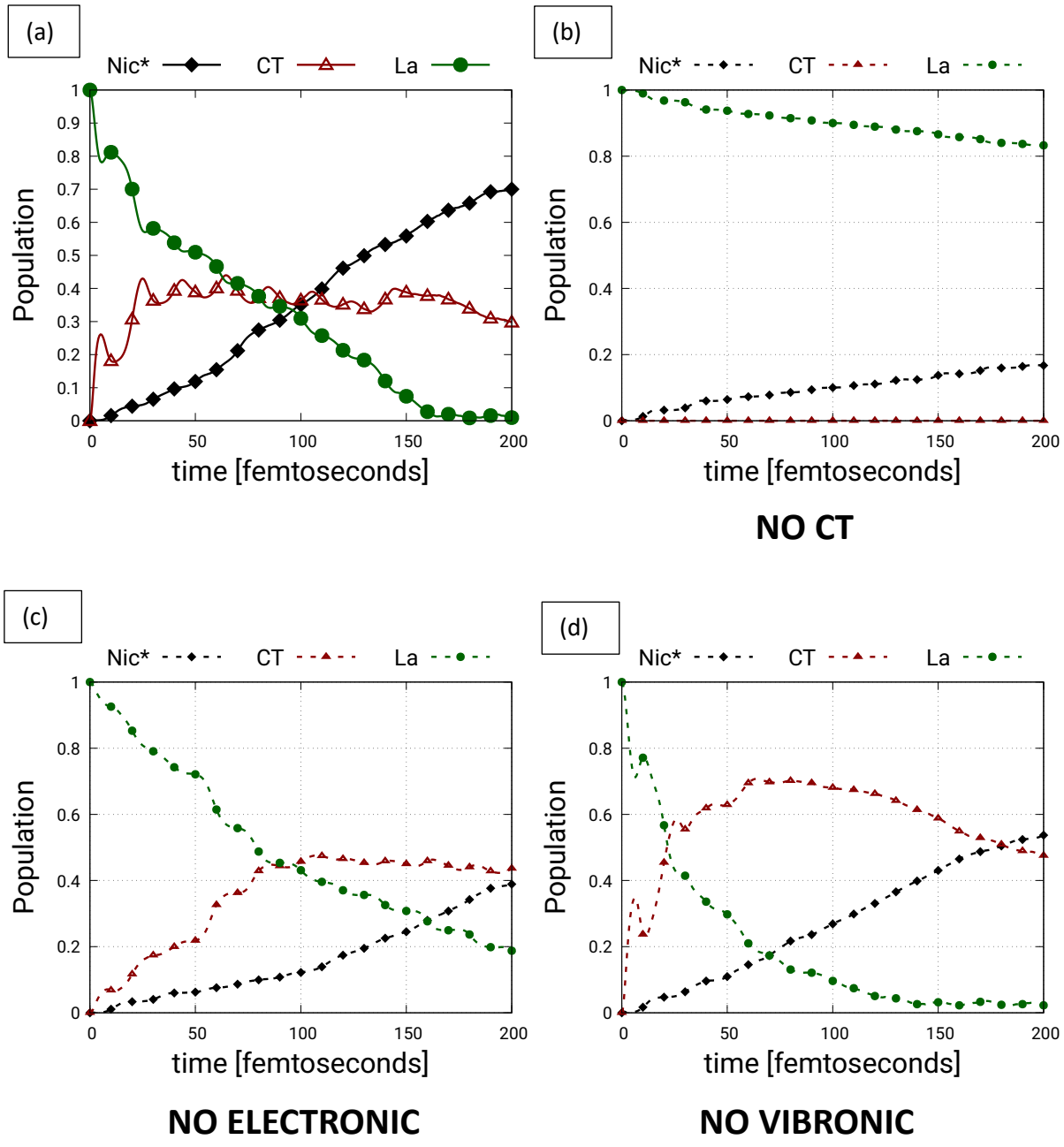

Suppl. Fig. 13.9: Caption same as Suppl. Fig. 13.1

Cluster C1
Structure 04

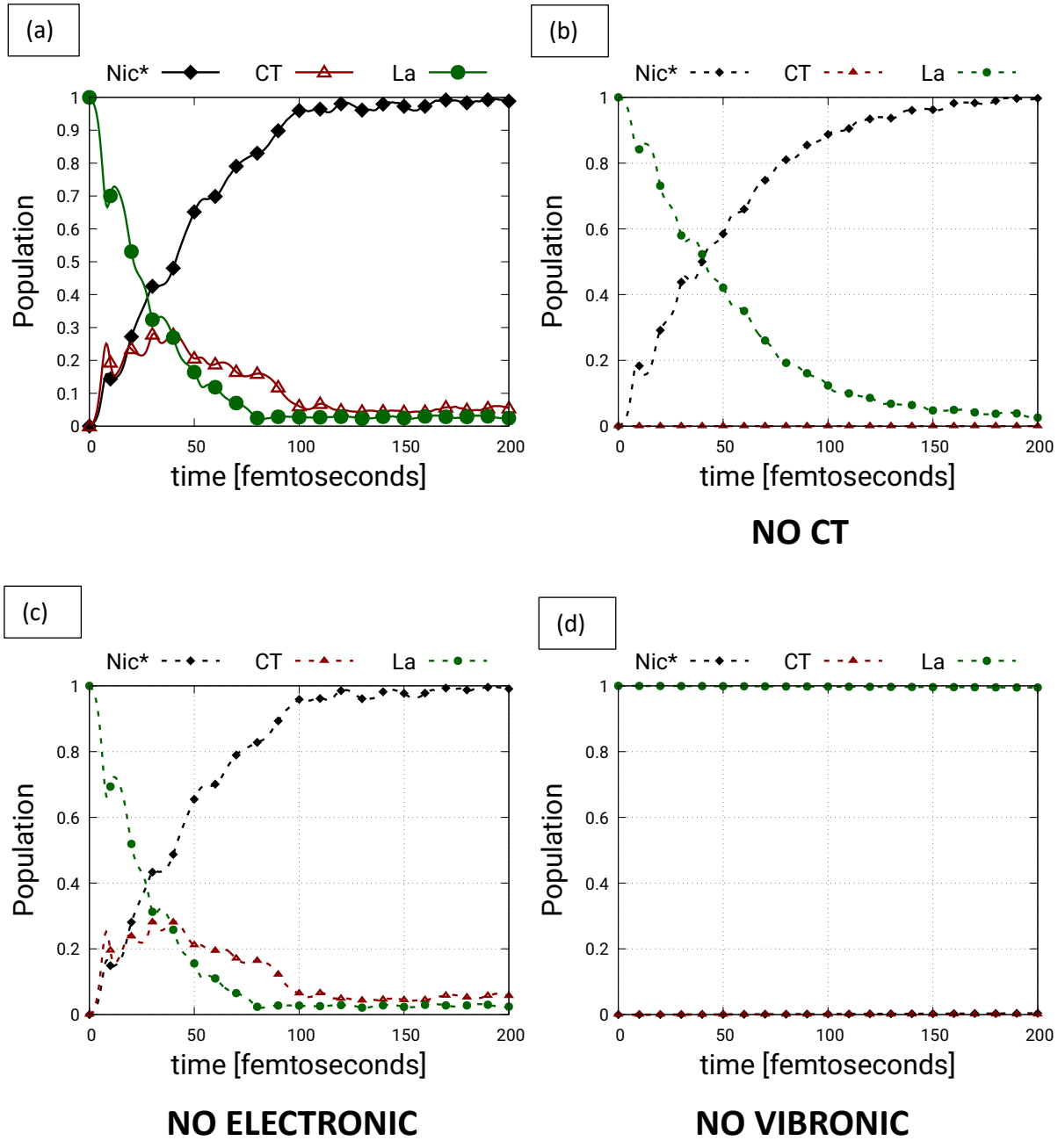

Suppl. Fig. 13.10: Caption same as Suppl. Fig. 13.1

Cluster C1
Structure 05

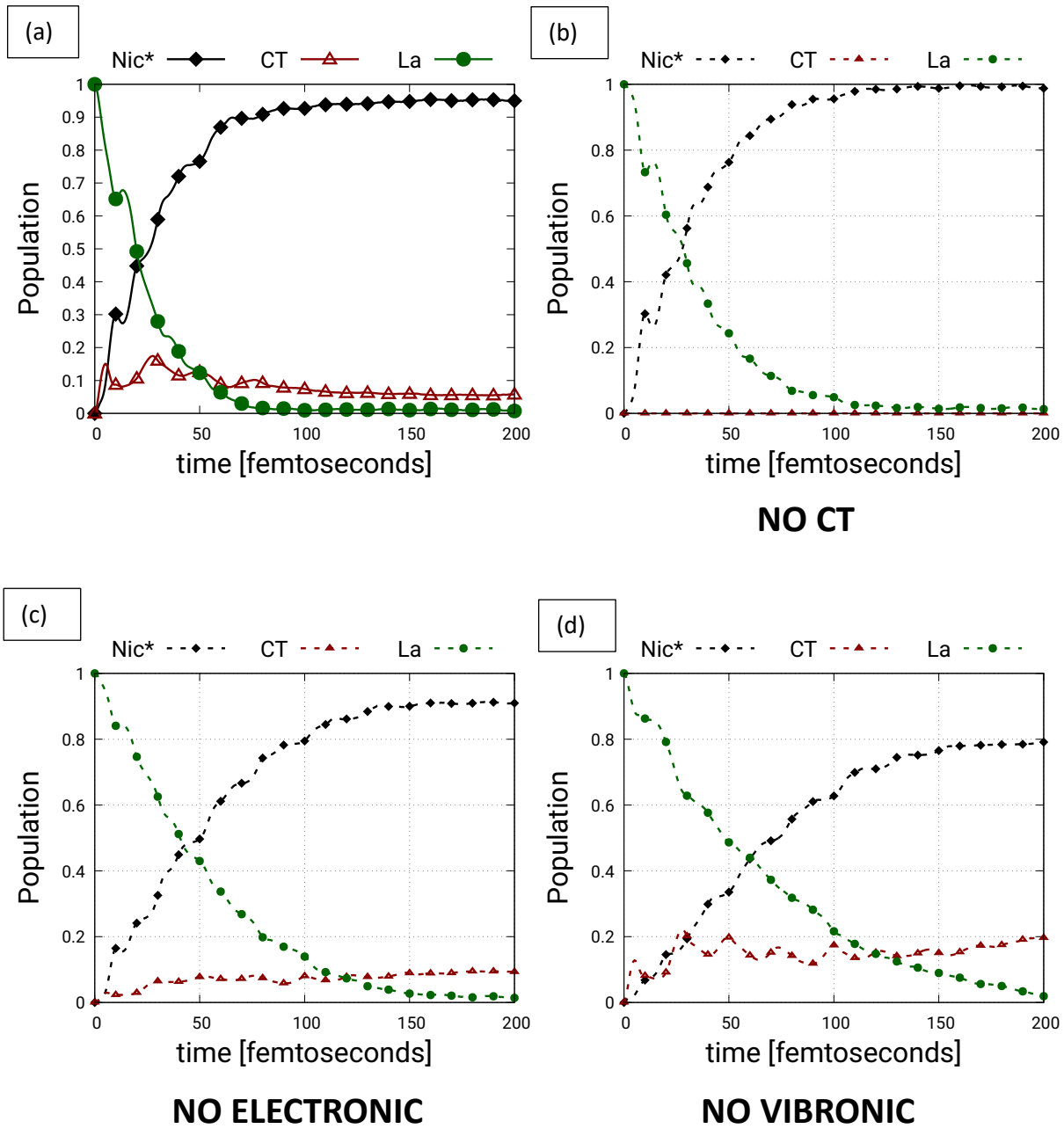

Suppl. Fig. 13.11: Caption same as Suppl. Fig. 13.1

Cluster C1
Structure 06

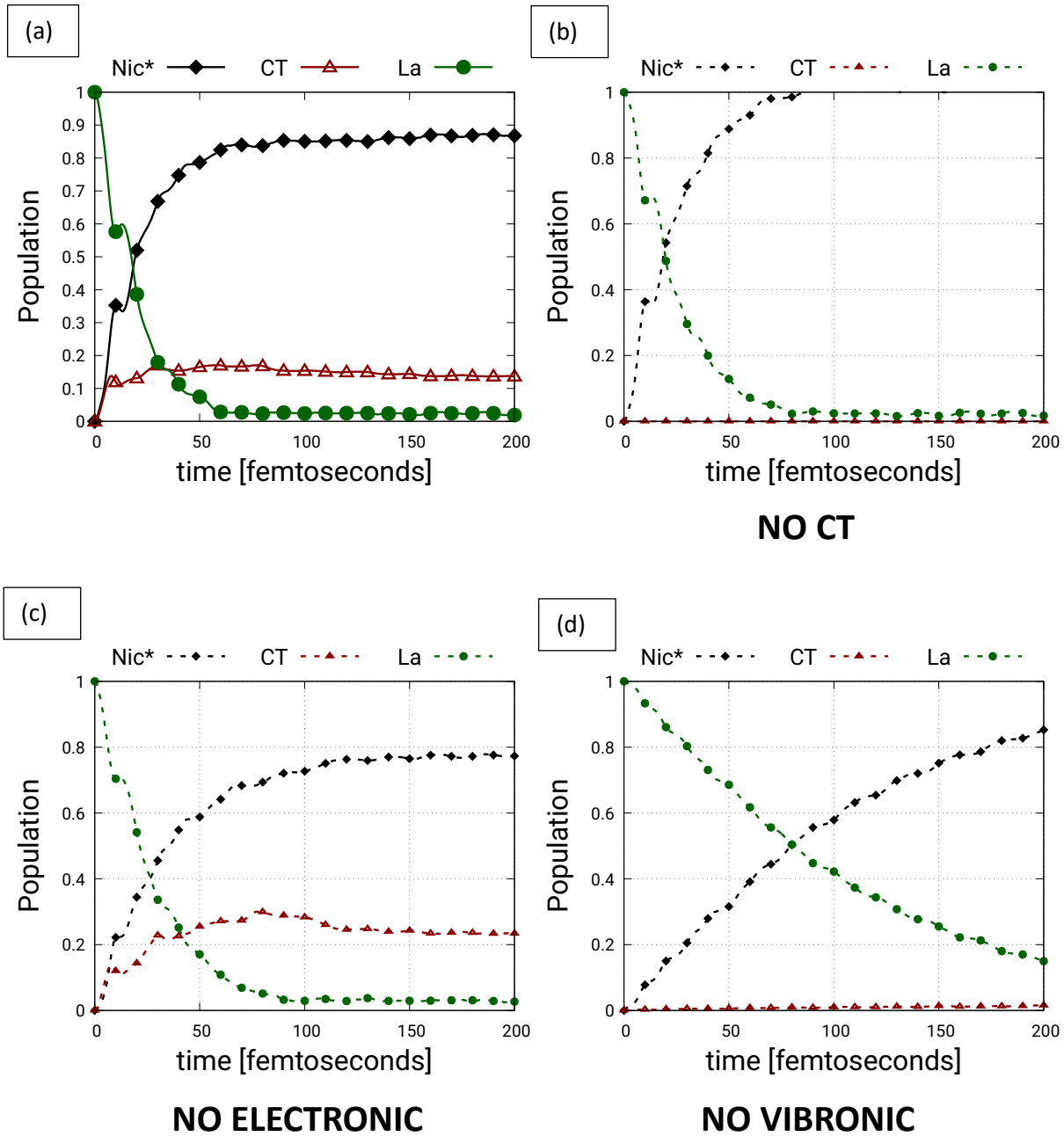

Suppl. Fig. 13.12: Caption same as Suppl. Fig. 13.1

Cluster C2
Structure 01

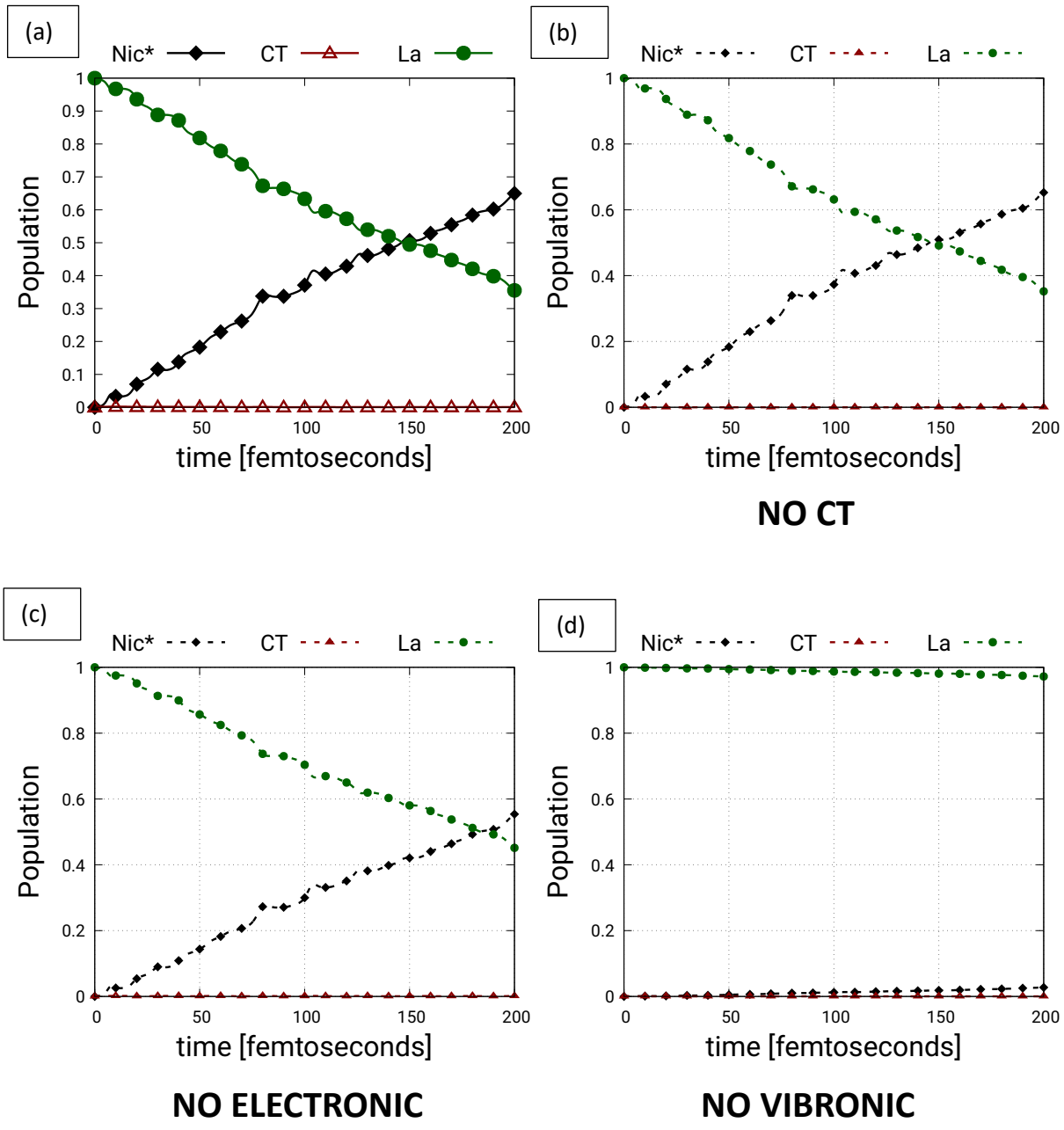

Suppl. Fig. 13.13: Caption same as Suppl. Fig. 13.1

Cluster C2
Structure 02

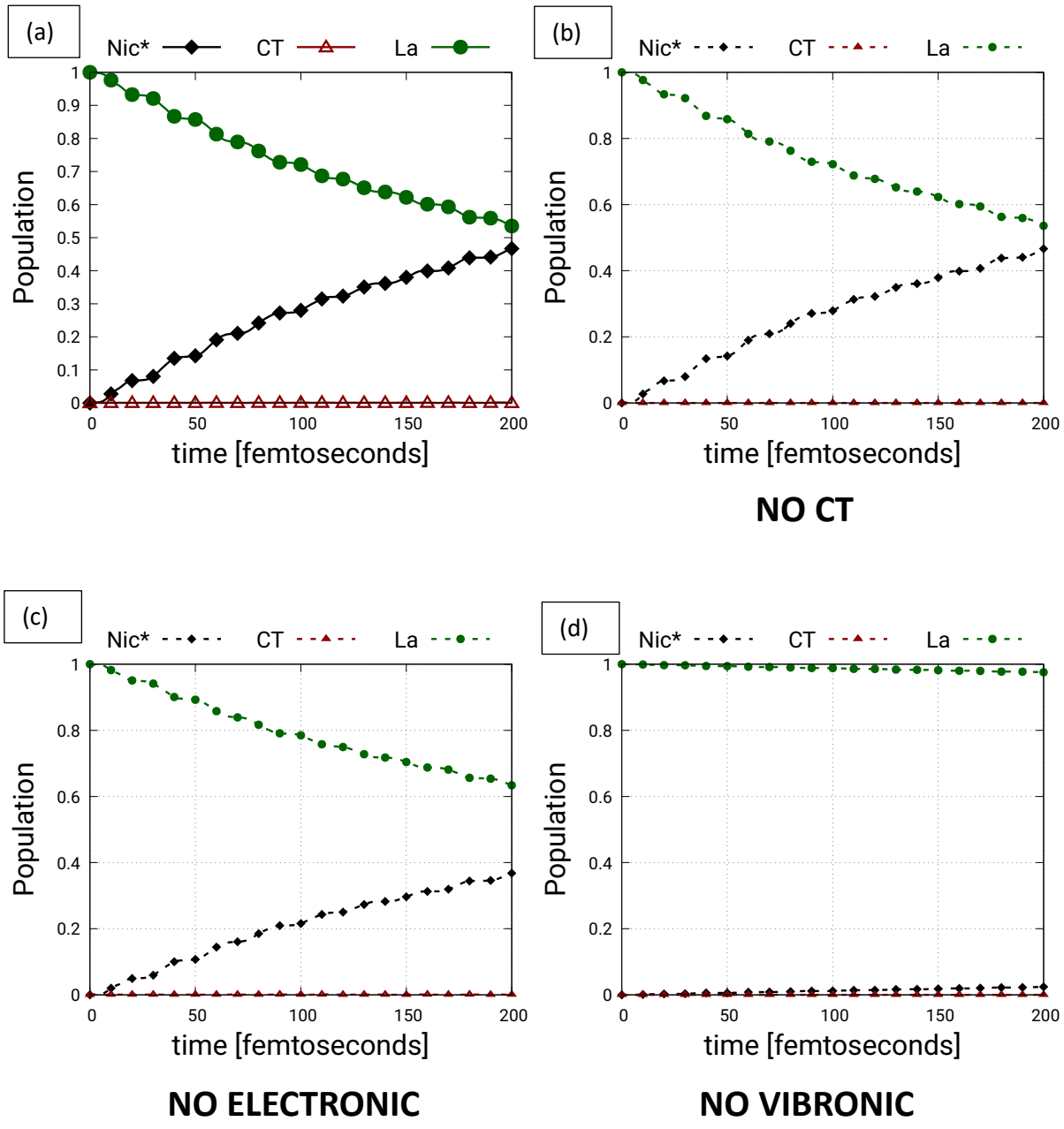

Suppl. Fig. 13.14: Caption same as Suppl. Fig. 13.1

Cluster C2
Structure 03

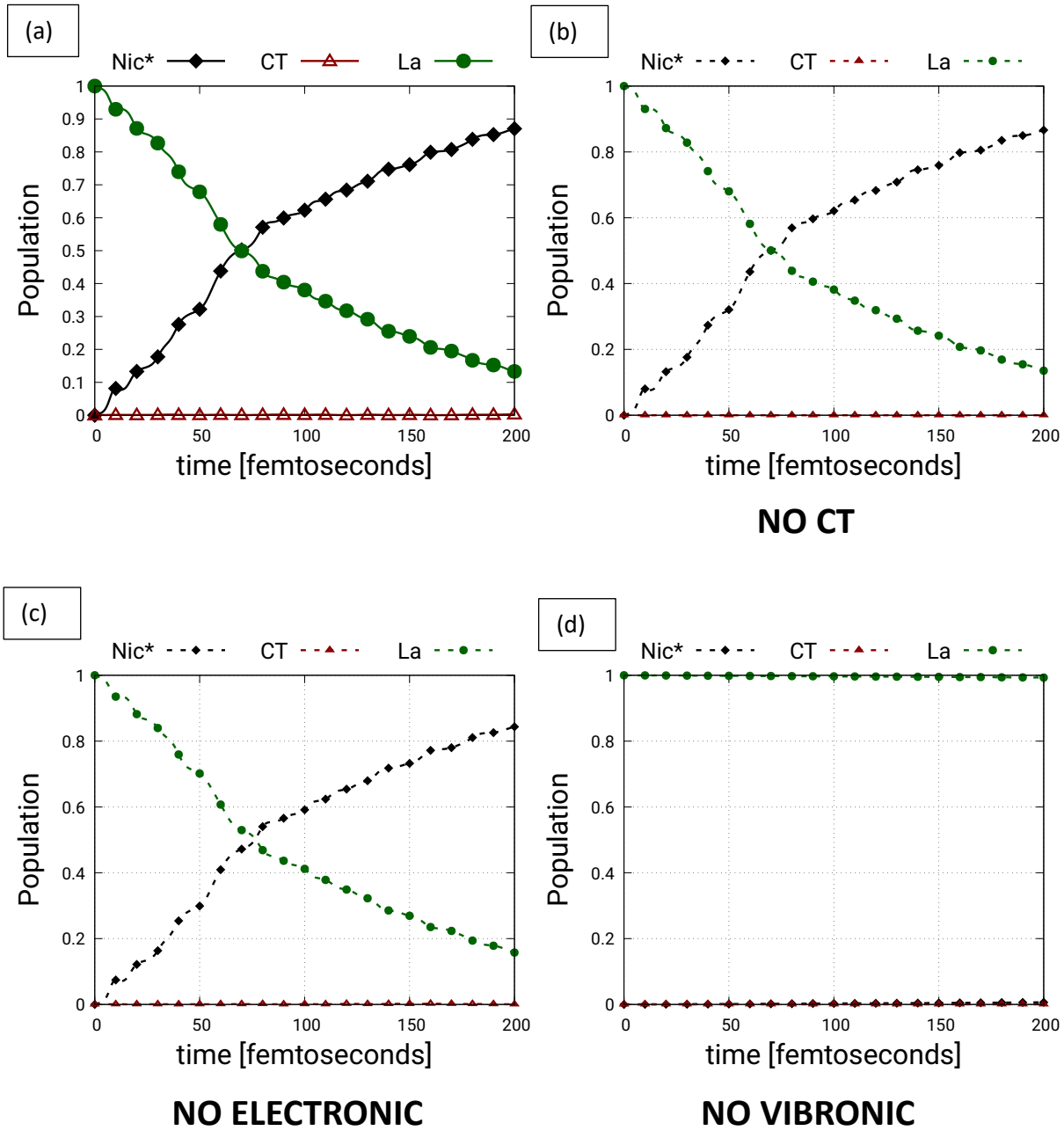

Suppl. Fig. 13.15: Caption same as Suppl. Fig. 13.1

Cluster C2
Structure 04

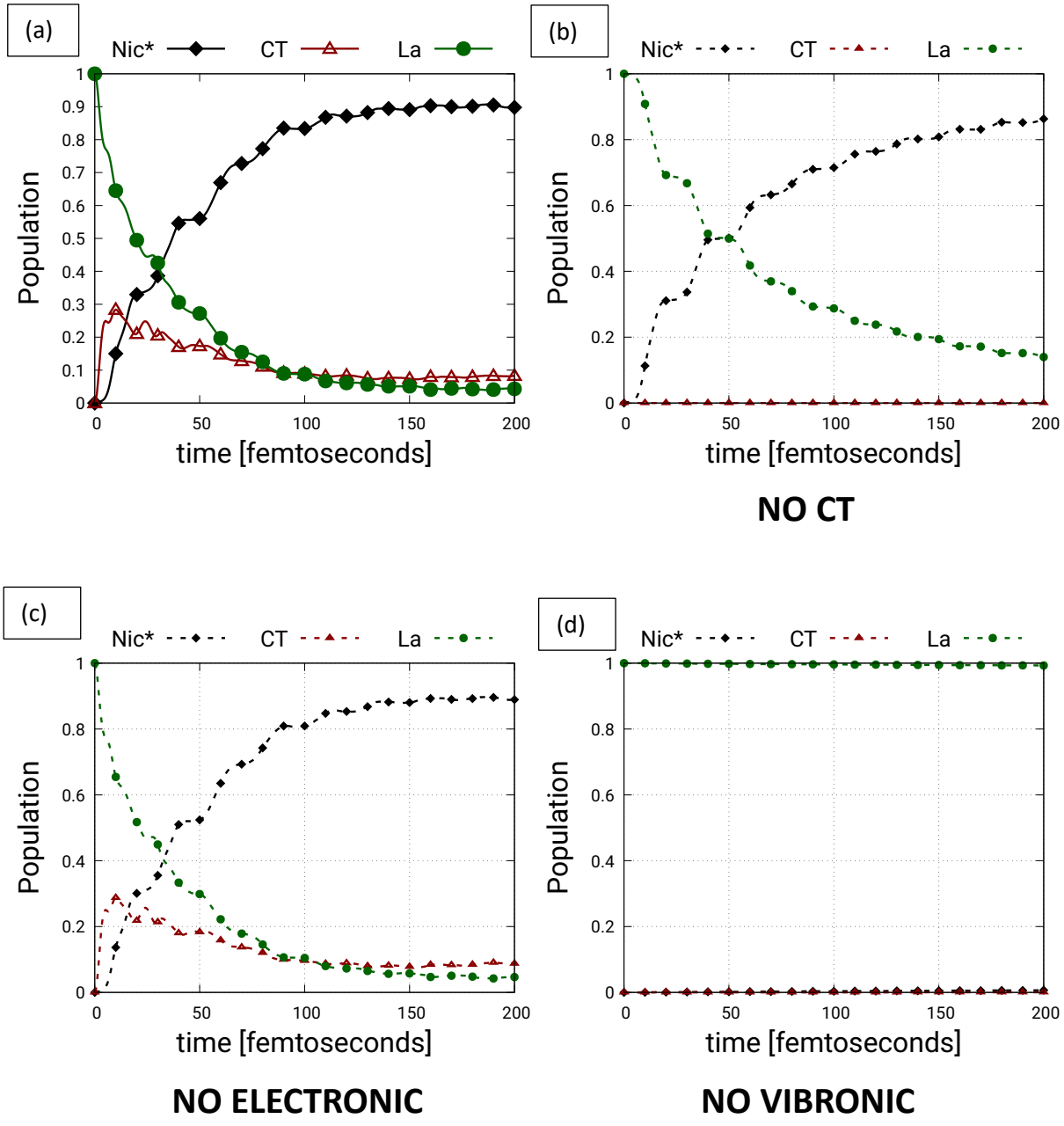

Suppl. Fig. 13.16: Caption same as Suppl. Fig. 13.1

Cluster C2
Structure 05

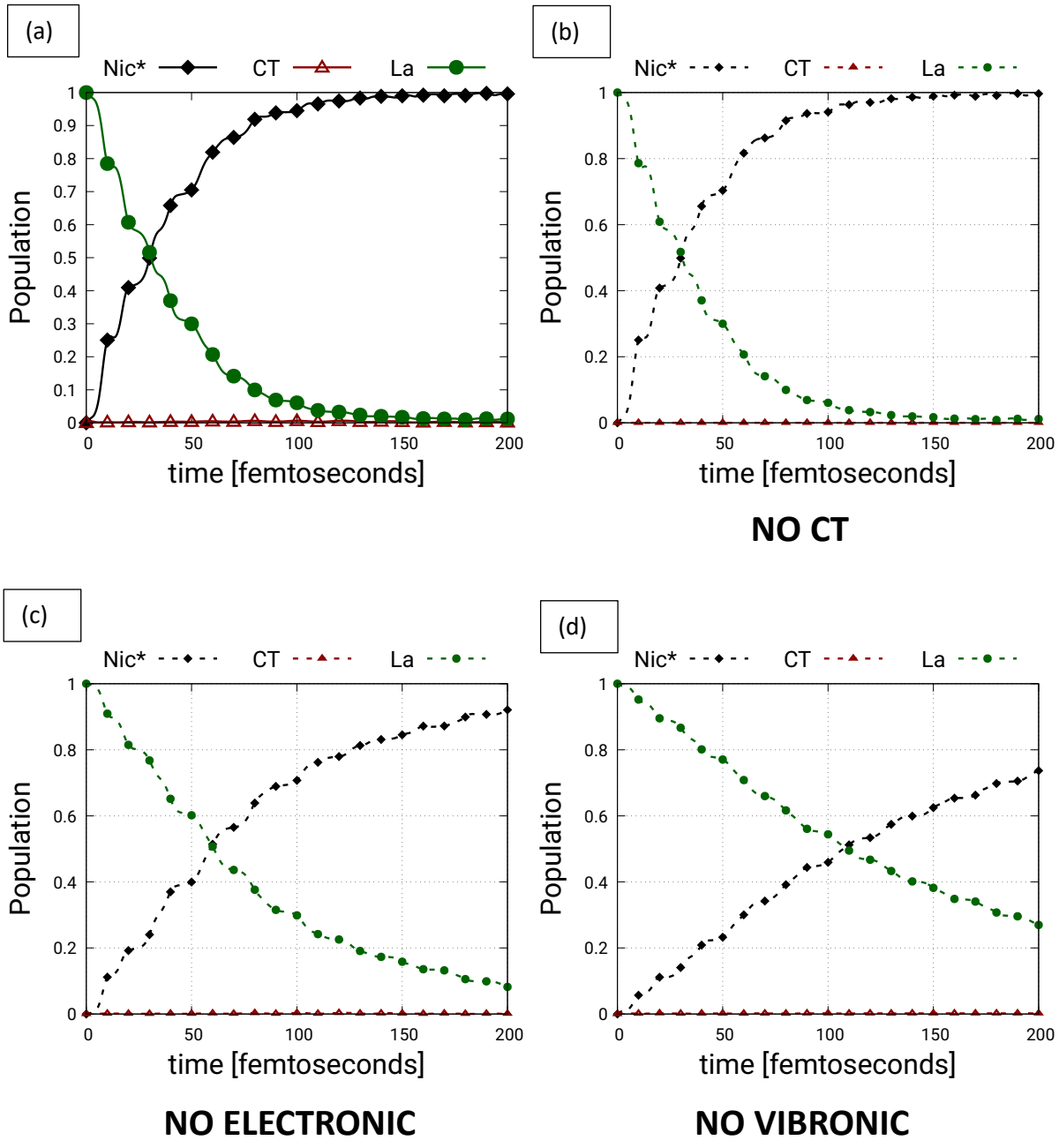

Suppl. Fig. 13.17: Caption same as Suppl. Fig. 13.1

Cluster C2
Structure 06

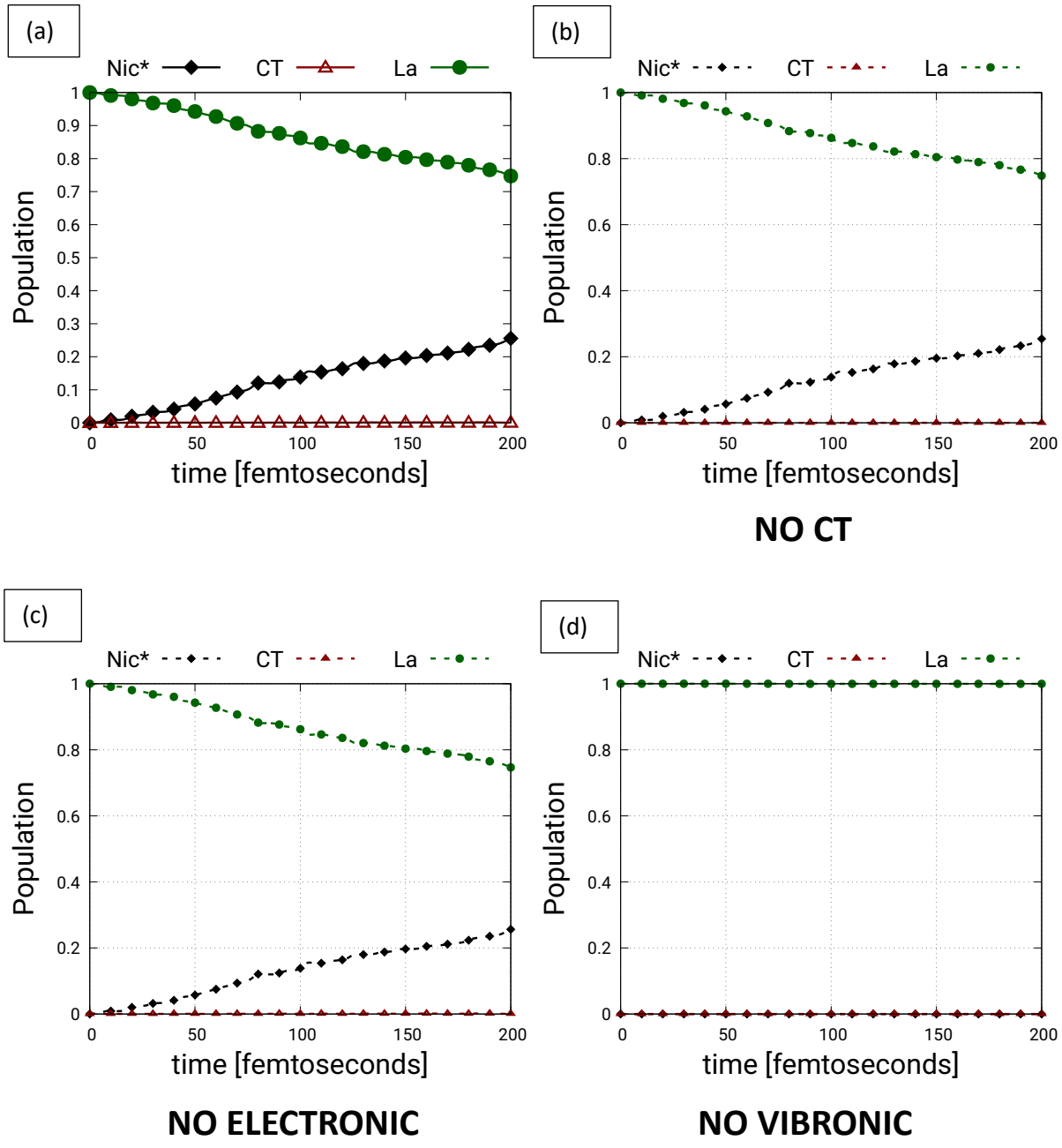

Suppl. Fig. 13.18: Caption same as Suppl. Fig. 13.1

Suppl. Note. 11 Selective effect of removing low-frequency modes on wavepacket dynamics

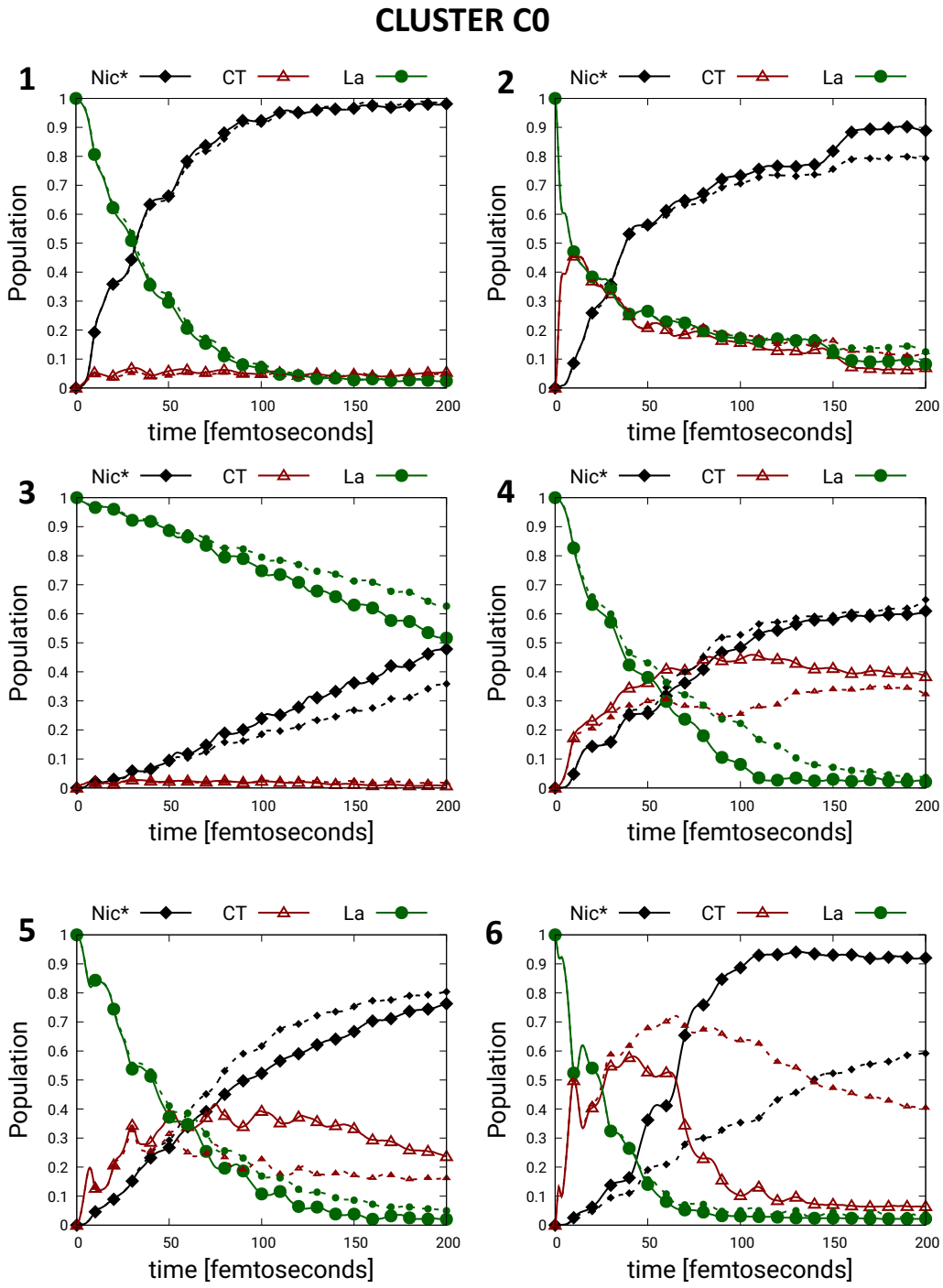

Suppl. Fig. 14: Solid Line: CT-mediated transfer same as Suppl. Fig. 10 including all couplings. Dashed line: CT mediated transfer after removing low frequency modes. Significantly slowed down population transfer is observed for Struct 06, where CT has an active doorway role in ultrafast EET dynamics.

Suppl. Note. 12 Photoactive normal modes responsible for EET transfer

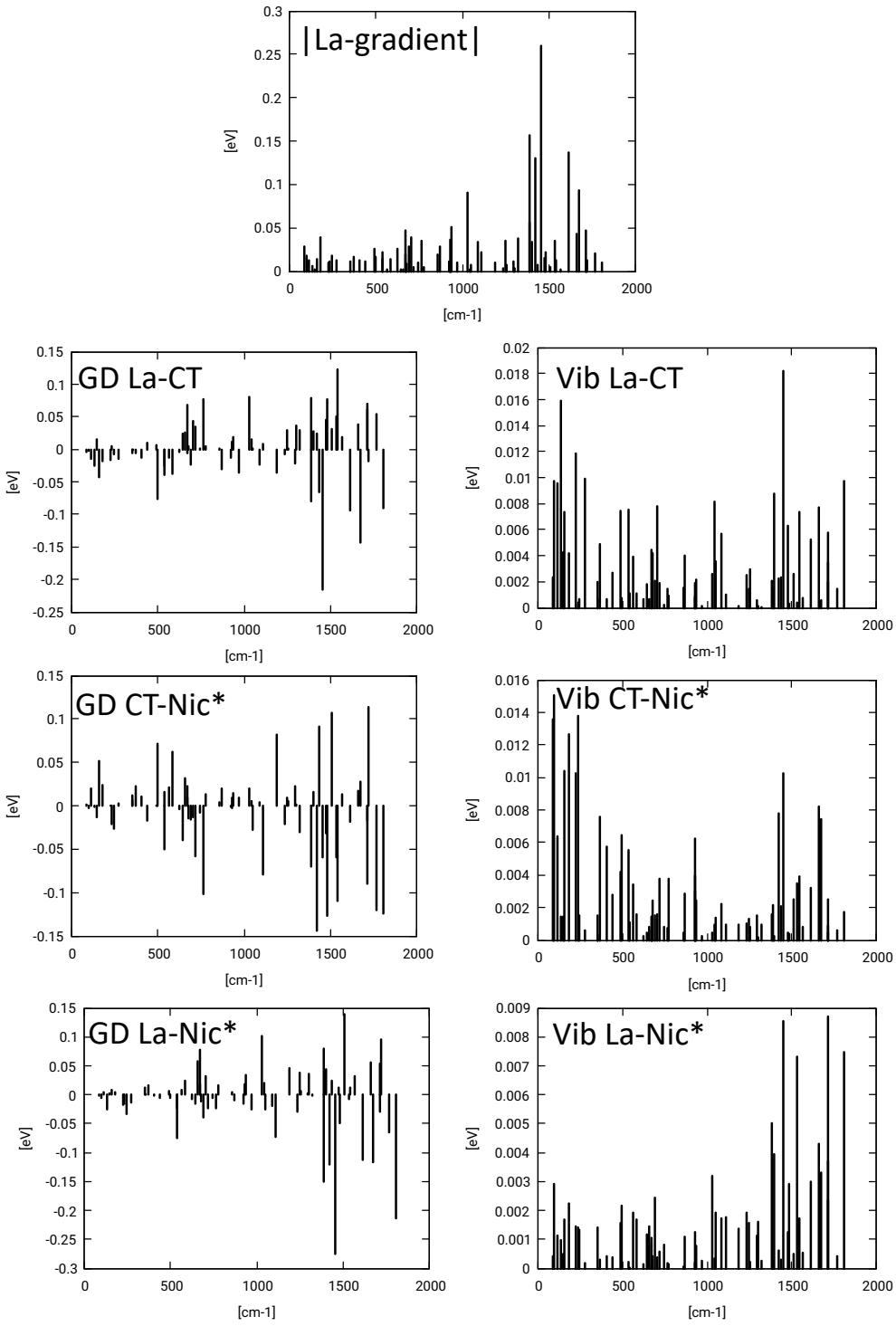

Suppl. Fig. 15: The photoexcited modes responsible for EET for a representative dynamic (Cluster C0 / Structure 06). The absolute value of gradient of La state along the modes , along with interstate gradient difference (GD) and absolute value of vibronic coupling (Vib) along the modes.

Suppl. Note. 13 Branching-space for CT-mediated and direct mechanism

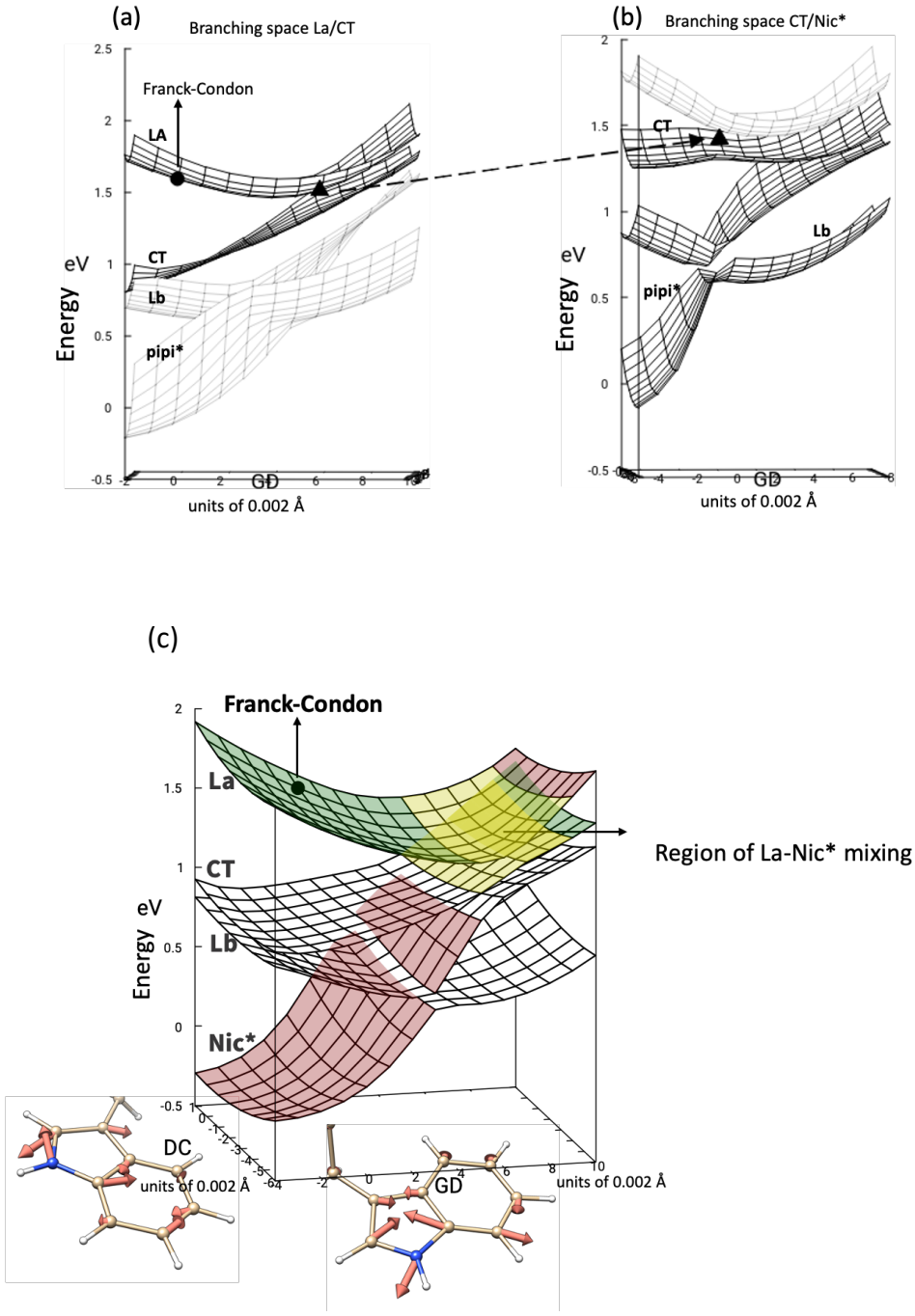

Suppl. Fig. 16: Branching space for (a,b) CT-mediated and (c) Direct EET mechanism showing the conical intersections involving relevant adiabatic states. The branching plane is a 2D PES along gradient difference (GD) and derivative coupling (DC) coordinates in units of Angstroms. These vectors have been computed at the Franck-Condon geometry in the present figures.

Suppl. Note. 14 Wavepacket dynamics on frozen solute in solvent ensemble

14.1 Generation of solvent ensemble

To disentangle the effect of solvent arrangement on the electronic-states and subsequent EET process, an equilibrated solvent ensemble around a fixed solute structure was created. The structure from C0/Struct C6 as labelled in Suppl. Table 6 was taken.

Since the velocities from REMD are not saved, a re-equilibrarion was done by heating the system from 0 to 300K in steps of 10K with 10ps dynamics in each step. This were done with restraints of 200 kcal/(mol·Å^2) to keep the solute fixed. After this, a MD at 300K and NPT for 100ps was done to equilibrate at constant pressure and temperature. Post equilibration, the production MD was run at the same NPT conditions for 200ps. Snapshots were saved every 2ps to obtain decorrelated solvent arrangements around the frozen solute.

A similar QM/MM setup comprising of a spherical droplet as reported in Section 4 was created. The previously optimized solute structure at QM/MM level was re-inserted inside every droplet. To obtain the LVC parameters vertical transition energies at XMS-CASPT2 |4,4| level were computed for every solvent snapshot and diabatized through a solvent-specific rotation matrix $\mathbf{D}_i$ for the i-th solvent snapshot as described in Section 7 to give energies and electronic couplings of solvent-specific LE/CT state.

The solvent specific diabatic states for every snapshot were taken as the reference states for ML-MCTDH dynamics amongst with population transfer was monitored. To obtain vibronic coupling terms, a wavefunction overlap method similar to Section 7 was employed. The overlap matrix $\mathbf{S}_i$ between the adiabatic states at Franck-Condon of **i-th** solvent snapshot $\psi[Q_0]_i$ and the previously computed adiabatic states at displaced geometries were utilized to transform the vibronic Hamiltonian matrix to solvent specific adiabatic-basis. This was then transformed to solvent-specific diabatic matrix through the rotation matrix $\mathbf{D}_i$. This procedure gives solvent specific vibronic-coupling terms along the normal modes for every snapshots of the ensemble.

14.2 Wavepacket dynamics on solvent ensemble in absence of CT-state

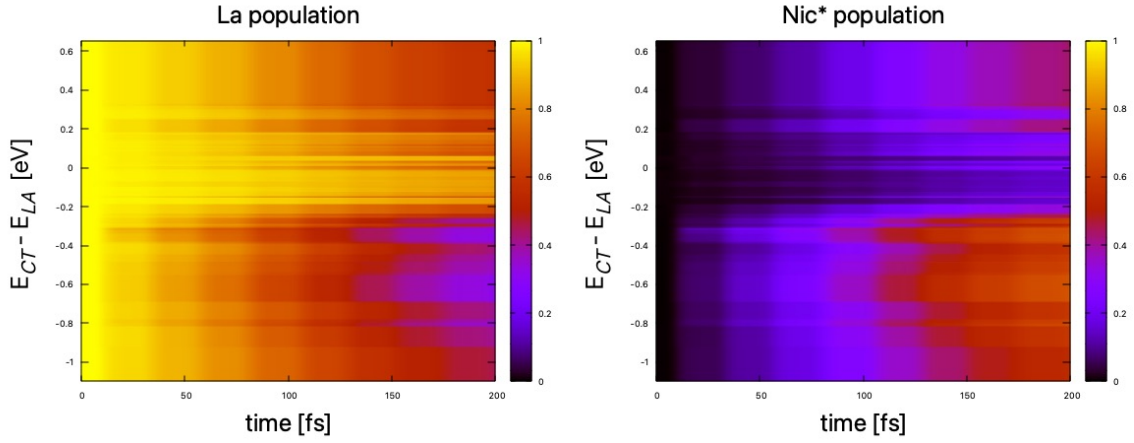

Suppl. Fig. 17: ML-MCTDH dynamics on solvent ensemble around frozen structure from most populated cluster without the CT-state.

Suppl. Note. 15 Coherences between the electronic states along EET dynamics for NADH

We focused on the two cases C0.06 (CT mediated) and C2.05 (direct transfer) investigated respectively in panels 2d and 2f of Figure 2 in the main text. The effect on the EET dynamics of the presence of the CT or of the constant (electronic coupling) and linear (vibronic coupling) terms among all the electronic states was already demonstrated in Figures S13.6 and Suppl. Fig. 13.17 of the SI.

Here we present the coherences for above two cases. We computed the quantum electronic coherences, i.e. the elements of $|La\rangle\langle CT|$, $|La\rangle\langle Nic^*|$, $|CT\rangle\langle Nic^*|$, and namely

$\langle\Psi(t)|La\rangle|\langle CT|\Psi(t)\rangle$, $\langle\Psi(t)|La\rangle|\langle Nic^*|\Psi(t)\rangle$, $\langle\Psi(t)|CT\rangle|\langle Nic^*|\Psi(t)\rangle$. (the other off-diagonal terms of the density matrix are the complex conjugate of these ones). They are represented by complex values and therefore we report both their absolute values and their real and imaginary components. It has been shown that the time dependence of the coherences χ_{ij} between states *i* and *j* is affected by several physical factors[14–16], including the product of the populations of the two states p_i and p_j (a coherence is trivially zero if one of the two states has zero population) and the overlap of the wavepackets components running of their surfaces. In order to disentangle these effects, like proposed in reference [14], we also report normalized coherences defined as $|\chi_{ij}|/\sqrt{p_i p_j}$.

It is interesting to notice that normalized coherences are always larger than true coherences, showing that part of their small values are simply due to the depopulation of one of the two states (the population contribution is largest when $p_i = p_j = 0.5$. On the other side, coherences and normalized coherences show the same recurrence times and this finding supports the interpretation that these recurrence depend on the vibrational coherent motion.

We computed the coherences both including all couplings or selectively switching off some of them (analogously as what done in Section 10 of this SI). Here we further added an additional test, obtained by setting to zero all diagonal gradients. The idea was to maintain the WP at rest in the nuclear coordinate space to check if this helps disentangling vibrational and electronic effects.

The comparative analysis of the results for the two snapshots indicate that the role of the tuning modes is essential for facilitating EET. If we switch them off (labelled λ_{ii}, 5th column in Figures S18 and S19), we observe high frequency oscillations in the coherences proportional to the electronic energy gaps due to the purely electronic coupling E_{ij}^0. Despite the coherences having sizeable values, no substantial population transfer takes place. On these grounds we can conclude that, despite the conformational heterogeneity of NADH, the EET is an intrinsically coherent process governed by coherently oscillating wave packets on the potential energy surfaces of the involved electronic states which tune the energy gaps and drive the EET unidirectionally from the donor to the acceptor. Such coherent EET cannot be described by incoherent mechanisms such a Förster theory

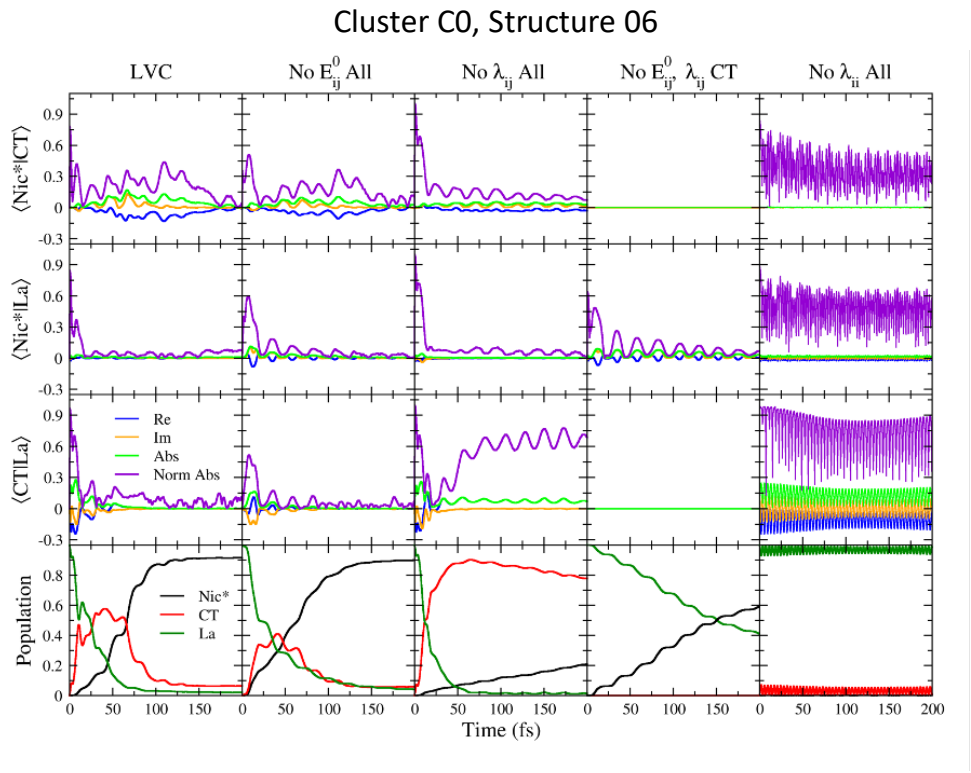

Suppl. Fig. 18: Coherences in EET dynamics involving CT state as an intermediary.

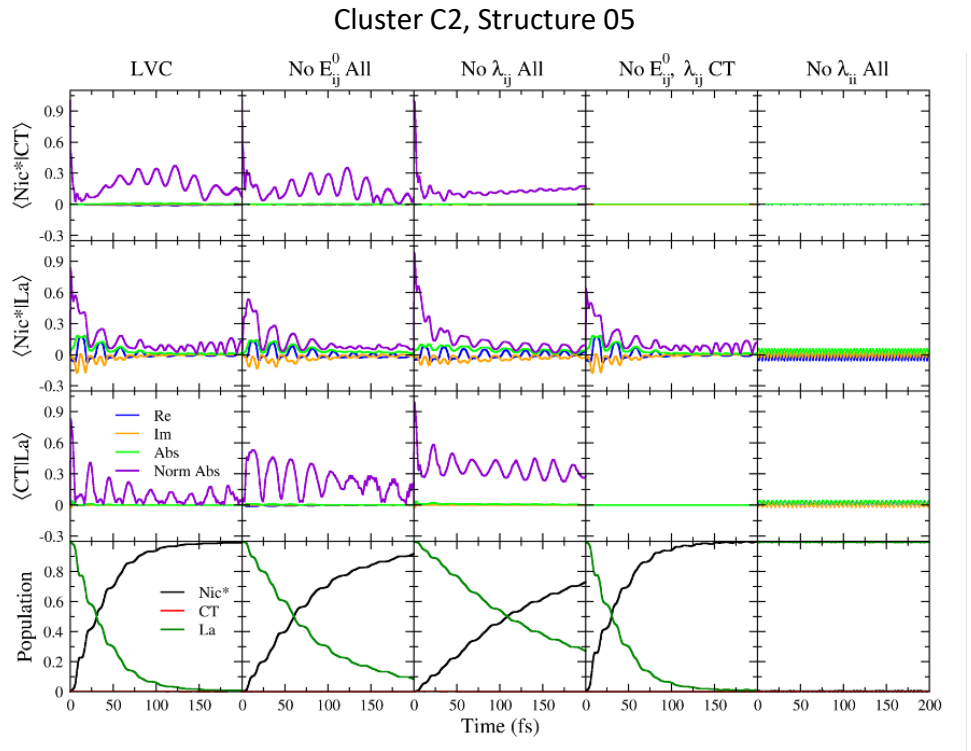

Suppl. Fig. 19: Coherences in EET dynamics involving direct population transfer from La to Nic*

Supplementary References

(1) Heiner, Z.; Roland, T.; Leonard, J.; Haacke, S.; Groma, G. I. Kinetics of Light-Induced Intramolecular Energy Transfer in Different Conformational States of NADH. *J. Phys. Chem. B* **2017**, *121* (34), 8037–8045. https://doi.org/10.1021/acs.jpcb.7b04753.

(2) Cao, S.; Li, H.; Liu, Y.; Zhang, M.; Wang, M.; Zhou, Z.; Chen, J.; Zhang, S.; Xu, J.; Knutson, J. R. Femtosecond Fluorescence Spectra of NADH in Solution: Ultrafast Solvation Dynamics. *The Journal of Physical Chemistry B* **2020**, *124* (5), 771–776. https://doi.org/10.1021/acs.jpcb.9b10656.

(3) Cadena-Caicedo, A.; Gonzalez-Cano, B.; López-Arteaga, R.; Esturau-Escofet, N.; Peon, J. Ultrafast Fluorescence Signals from β-Dihydronicotinamide Adenine Dinucleotide: Resonant Energy Transfer in the Folded and Unfolded Forms. *The Journal of Physical Chemistry B* **2020**, *124* (3), 519–530. https://doi.org/10.1021/acs.jpcb.9b10012.

(4) Reza, M. M.; Durán-Hernández, J.; González-Cano, B.; Jara-Cortés, J.; López-Arteaga, R.; Cadena-Caicedo, A.; Muñoz-Rugeles, L.; Hernández-Trujillo, J.; Peon, J. Primary Photophysics of Nicotinamide Chromophores in Their Oxidized and Reduced Forms. *J. Phys. Chem. B* **2023**, *127* (39), 8432–8445. https://doi.org/10.1021/acs.jpcb.3c03246.

(5) *Handbook of Biochemistry and Molecular Biology*, 3rd ed.; Fasman, G. D., Ed.; CRC Press: London, England, 2021. https://doi.org/10.1201/9780429264214.

(6) McComb, R. B.; Bond, L. W.; Burnett, R. W.; Keech, R. C.; Bowers, G. N., Jr. Determination of the Molar Absorptivity of NADH. *Clinical Chemistry* **1976**, *22* (2), 141–150. https://doi.org/10.1093/clinchem/22.2.141.

(7) Osik, N. A.; Zelentsova, E. A.; Sharshov, K. A.; Tsentalovich, Y. P. Nicotinamide Adenine Dinucleotide Reduced (NADH) Is a Natural UV Filter of Certain Bird Lens. *Scientific Reports* **2022**, *12* (1), 16850. https://doi.org/10.1038/s41598-022-21139-x.

(8) Hayatshahi, H. S.; Henriksen, N. M.; Cheatham, T. E. Consensus Conformations of Dinucleoside Monophosphates Described with Well-Converged Molecular Dynamics Simulations. *Journal of Chemical Theory and Computation* **2018**, *14* (3), 1456–1470. https://doi.org/10.1021/acs.jctc.7b00581.

(9) Pavelites, J. J.; Gao, J.; Bash, P. A.; Mackerell Jr., A. D. A Molecular Mechanics Force Field for NAD+ NADH, and the Pyrophosphate Groups of Nucleotides. *Journal of Computational Chemistry* **1997**, *18* (2), 221–239. https://doi.org/10.1002/(SICI)1096-987X(19970130)18:2<221::AID-JCC7>3.0.CO;2-X.

(10) Walker, R. C.; de Souza, M. M.; Mercer, I. P.; Gould, I. R.; Klug, D. R. Large and Fast Relaxations inside a Protein: Calculation and Measurement of Reorganization Energies in Alcohol Dehydrogenase. *J. Phys. Chem. B* **2002**, *106* (44), 11658–11665. https://doi.org/10.1021/jp0261814.

(11) Ester, M.; Kriegel, H.-P.; Sander, J.; Xu, X. A Density-Based Algorithm for Discovering Clusters in Large Spatial Databases with Noise. In *Proceedings of the Second International Conference on Knowledge Discovery and Data Mining*; KDD'96; AAAI Press: Portland, Oregon, 1996; pp 226–231.

(12) Hsu, C.-P.; You, Z.-Q.; Chen, H.-C. Characterization of the Short-Range Couplings in Excitation Energy Transfer. *J. Phys. Chem. C* **2008**, *112* (4), 1204–1212. https://doi.org/10.1021/jp076512i.

(13) Azumi, T.; Matsuzaki, K. WHAT DOES THE TERM "VIBRONIC COUPLING" MEAN? *Photochemistry and Photobiology* **1977**, *25* (3), 315–326. https://doi.org/10.1111/j.1751-1097.1977.tb06918.x.

(14) Matselyukh, D. T.; Despré, V.; Golubev, N. V.; Kuleff, A. I.; Wörner, H. J. Decoherence and Revival in Attosecond Charge Migration Driven by Non-Adiabatic Dynamics. *Nature Physics* **2022**, *18* (10), 1206–1213. https://doi.org/10.1038/s41567-022-01690-0.

(15) Vacher, M.; Bearpark, M. J.; Robb, M. A.; Malhado, J. P. Electron Dynamics upon Ionization of Polyatomic Molecules: Coupling to Quantum Nuclear Motion and Decoherence. *Phys. Rev. Lett.* **2017**, *118* (8), 083001. https://doi.org/10.1103/PhysRevLett.118.083001.

(16) Fiete, G. A.; Heller, E. J. Semiclassical Theory of Coherence and Decoherence. *Phys. Rev. A* **2003**, *68* (2), 022112. https://doi.org/10.1103/PhysRevA.68.022112.